

Search for the Standard Model Higgs boson in the dimuon decay channel with the ATLAS detector

Dissertation

zur Erlangung des akademischen Grades

Doctor rerum naturalium

(Dr. rer. nat.)

vorgelegt der

**Fakultät Mathematik und Naturwissenschaften der
Technischen Universität Dresden**

von

Dipl.-Phys. Jörg Christian Rudolph

geboren am 14.11.1984 in Karl-Marx-Stadt (jetzt Chemnitz)

eingereicht am 16.07.2014

verteidigt am 12.09.2014



1. Gutachter: Prof. Dr. Michael Kobel
2. Gutachter: Prof. Dr. Otmar Biebel

Kurzfassung

Die Suche nach dem Higgs-Boson des Standardmodells der Teilchenphysik stellte einen der Hauptgründe für den Bau des Large Hadron Colliders (LHC) dar, dem derzeit größten Teilchenphysik-Experiment der Welt. Die vorliegende Arbeit ist gleichfalls von dieser Suche getrieben. Der direkte Zerfall des Higgs-Bosons in Myonen wird untersucht. Dieser Kanal hat mehrere Vorteile. Zum einen ist der Endzustand, bestehend aus zwei Myonen unterschiedlicher Ladung, leicht nachzuweisen und besitzt eine klare Signatur. Weiterhin ist die Massenauflösung hervorragend, sodass eine gegebenenfalls vorhandene Resonanz gleich in ihrer grundlegenden Eigenschaft - ihrer Masse - bestimmt werden kann. Leider ist der Zerfall des Higgs-Bosons in ein Paar von Myonen sehr selten. Lediglich etwa 2 von 10000 erzeugten Higgs-Bosonen zeigen diesen Endzustand¹. Außerdem existiert mit dem Standardmodellprozess $Z/\gamma^* \rightarrow \mu\mu$ ein Zerfall mit einer sehr ähnlichen Signatur, jedoch um Größenordnungen höherer Eintrittswahrscheinlichkeit. Auf ein entstandenes Higgs-Boson kommen so etwa 1,5 Millionen Z-Bosonen, welche am LHC bei einer Schwerpunktsenergie von $\sqrt{s} = 8$ TeV produziert werden.

In dieser Arbeit werden zwei eng miteinander verwandte Analysen präsentiert. Zum einen handelt es sich hierbei um die Untersuchung des Datensatzes von Proton-Proton-Kollisionen bei einer Schwerpunktsenergie von 8 TeV, aufgezeichnet vom ATLAS-Detektor im Jahre 2012, auch als *alleinstehende* Analyse bezeichnet. Zum anderen erfolgt die Präsentation der *kombinierten* Analyse des kompletten Run-I Datensatzes, welcher aus Aufzeichnungen von Proton-Proton-Kollisionen der Jahre 2011 und 2012 bei Schwerpunktsenergien von 7 TeV bzw. 8 TeV besteht. In beiden Fällen wird die Verteilung der invarianten Myon-Myon-Masse nach einer schmalen Resonanzsignatur auf der kontinuierlichen Untergrundverteilung hin untersucht. Dabei dient die theoretisch erwartete Massenverteilung sowie die Massenauflösung des ATLAS-Detektors als Grundlage, um analytische Parametrisierungen der Signal- und Untergrundverteilungen zu entwickeln. Auf diese Art wird der Einfluss systematischer Unsicherheiten auf Grund von ungenauer Beschreibung der Spektren in Monte-Carlo Simulationen verringert. Verbleibende systematische Unsicherheiten auf die Signalakzeptanz werden auf eine neuartige Weise bestimmt. Zusätzlich wird ein bisher einzigartiger Ansatz verfolgt, um die systematische Unsicherheit resultierend aus der Wahl der Untergrundparametrisierung in der kombinierten Analyse verfolgt. Zum ersten Mal wird dabei die Methode des scheinbaren Signals auf einem simulierten Untergrunddatensatz auf Generator-Niveau angewendet, was eine Bestimmung des Einflusses des Untergrundmodells auf die Anzahl der ermittelten Signalereignisse mit nie dagewesener Präzision ermöglicht.

In keiner der durchgeführten Analysen konnte ein signifikanter Überschuss im invarianten Massenspektrum des Myon-Myon-Systems nachgewiesen werden, sodass obere Ausschlussgrenzen auf die Signalstärke $\mu = \sigma/\sigma_{SM}$ in Abhängigkeit von der Higgs-Boson-Masse gesetzt werden. Dabei sind Stärken von $\mu \geq 10,13$ bzw. $\mu \geq 7,05$ mit einem Konfidenzniveau von 95% durch die alleinstehende bzw. kombinierte Analyse ausgeschlossen, jeweils für eine Higgs-Boson-Masse von 125,5 GeV.

Die erzielten Ergebnisse werden ebenfalls im Hinblick auf die kürzlich erfolgte Entdeckung des neuen Teilchens interpretiert, dessen Eigenschaften mit den Vorhersagen eines Standardmodell-Higgs-Bosons mit einer Masse von etwa 125,5 GeV kompatibel sind. Dabei werden obere Grenzen auf das Verzweungsverhältnis von $BR(H \rightarrow \mu\mu) \leq 1,3 \times 10^{-3}$ und auf die Yukawa-Kopplung des Myons von $\lambda_\mu \leq 1,6 \times 10^{-3}$ gesetzt, jeweils mit einem Konfidenzniveau von 95%.

¹bei einer angenommenen Higgs-Boson-Masse von 125 GeV

Abstract

The search for the Standard Model Higgs boson was one of the key motivations to build the world's largest particle physics experiment to date, the Large Hadron Collider (LHC). This thesis is equally driven by this search, and it investigates the direct muonic decay of the Higgs boson. The decay into muons has several advantages: it provides a very clear final state with two muons of opposite charge, which can easily be detected. In addition, the muonic final state has an excellent mass resolution, such that an observed resonance can be pinned down in one of its key properties: its mass. Unfortunately, the decay of a Standard Model Higgs boson into a pair of muons is very rare, only two out of 10000 Higgs bosons are predicted to exhibit this decay.² On top of that, the non-resonant Standard Model background arising from the $Z/\gamma^* \rightarrow \mu\mu$ process has a very similar signature, while possessing a much higher cross-section. For one produced Higgs boson, there are approximately 1.5 million Z bosons produced at the LHC for a centre-of-mass energy of 8 TeV.

Two related analyses are presented in this thesis: the investigation of 20.7 fb^{-1} of the proton-proton collision dataset recorded by the ATLAS detector in 2012, referred to as *standalone* analysis, and the *combined* analysis as the search in the full run-I dataset consisting of proton-proton collision data recorded in 2011 and 2012, which corresponds to an integrated luminosity of $\mathcal{L}_{int} = 24.8 \text{ fb}^{-1}$. In each case, the dimuon invariant mass spectrum is examined for a narrow resonance on top of the continuous background distribution. The dimuon phenomenology and ATLAS detector performance serve as the foundations to develop analytical models describing the spectra. Using these analytical parametrisations for the signal and background mass distributions, the sensitivity of the analyses to systematic uncertainties due to Monte-Carlo simulation mismodeling are minimised. These residual systematic uncertainties are addressed in a unique way as signal acceptance uncertainties. In addition, a new approach to assess the systematic uncertainty associated with the choice of the background model is designed for the combined analysis. For the first time, the spurious signal technique is performed on generator-level simulated background samples, which allows for a precise determination of the background fit bias.

No statistically significant excess in the dimuon invariant mass spectrum is observed in either analysis, and upper limits are set on the signal strength $\mu = \sigma/\sigma_{SM}$ as a function of the Higgs boson mass. Signal strengths of $\mu \geq 10.13$ and $\mu \geq 7.05$ are excluded for a Higgs boson mass of 125.5 GeV with a confidence level of 95% by the standalone and combined analysis, respectively.

In the light of the discovery of a particle consistent with the predictions for a Standard Model Higgs boson with a mass of $m_H = 125.5 \text{ GeV}$, the search results are reinterpreted for this special case, setting upper limits on the Higgs boson branching ratio of $BR(H \rightarrow \mu\mu) \leq 1.3 \times 10^{-3}$, and on the muon Yukawa coupling of $\lambda_\mu \leq 1.6 \times 10^{-3}$, both with a confidence level of 95 %.

²Assuming a Higgs boson mass of 125 GeV.

Contents

Kurzfassung	III
Abstract	V
1 Introduction	1
2 Theoretical Foundations	3
2.1 The Standard Model of Particle Physics	3
2.1.1 Particles and Interactions	3
2.1.2 Electroweak Sector and the Higgs Mechanism	4
2.1.2.1 Electroweak Standard Model	4
2.1.2.2 The Higgs Mechanism	6
2.2 Phenomenology of Dimuon Events	7
2.2.1 Dimuon Production at the LHC	7
2.2.2 Higgs Boson Production and Decay	8
3 Experimental Setup	11
3.1 The LHC	11
3.2 The ATLAS Detector	11
3.2.1 ATLAS Coordinate System	12
3.2.2 Inner Detector Tracking System	13
3.2.2.1 Pixel Detector	13
3.2.2.2 Semi Conductor Tracker	14
3.2.2.3 Transition Radiation Tracker	14
3.2.3 Calorimeter System	15
3.2.3.1 Electromagnetic Calorimeter	15
3.2.3.2 Hadronic Calorimeter	16
3.2.3.3 Forward Calorimeter	16
3.2.4 Muon Spectrometer	16
3.2.4.1 Monitored Drift Tubes	16
3.2.4.2 Cathode Strip Chambers	18
3.2.4.3 Resistive Plate Chambers	18
3.2.4.4 Thin Gap Chambers	19
3.2.5 Magnet System	19
3.2.6 Trigger System	20
3.2.6.1 Muon Trigger	22
3.2.7 Luminosity Detectors	23
4 Event Simulation	25
4.1 Concepts of Monte Carlo Simulation in Particle Physics	25
4.1.1 Parton Distribution Functions	26
4.1.2 Hard Scattering	26
4.1.3 Parton Shower	26
4.1.3.1 Matching of Matrix Element and Parton Shower	27
4.1.4 Hadronisation	27
4.1.5 Detector Simulation	28
4.2 Monte Carlo Generators	28
4.2.1 Powheg	28
4.2.2 MC@NLO	28
4.2.3 Pythia	29
4.2.4 Alpgen	29

5	Muon Reconstruction and Identification	31
5.1	Standalone Muon Reconstruction	31
5.2	Combined Muon Reconstruction	31
5.3	Segment-tagged Muon Reconstruction	32
5.4	Calorimeter-tagged Muon Reconstruction	32
5.5	Muon Reconstruction Performance	33
5.5.1	Reconstruction Efficiency	33
5.5.2	Momentum Scale and Resolution	33
6	Event Selection	35
6.1	Trigger Selection	35
6.1.1	Trigger Efficiencies	35
6.1.2	Trigger Scale Factors	36
6.2	Baseline Selection	38
6.2.1	Physics Object Definitions	38
6.2.1.1	Muons	38
6.2.1.2	Jets	39
6.2.1.3	Missing Transverse Energy	39
6.2.2	Event Preselection	40
6.2.3	Candidate Event Selection	40
6.3	Analysis Categories	44
6.3.1	Resolution Categorisation	44
6.3.2	8 TeV Standalone Analysis Categories	45
6.3.3	7 + 8 TeV Combined Analysis Categories	47
7	Signal and Background Modeling	51
7.1	Signal Modeling	51
7.2	Background Modeling	57
7.2.1	Standalone Analysis Background Model	57
7.2.1.1	Goodness-of-fit Studies	57
7.2.2	Combined Analysis Background Model	61
7.2.2.1	Background Model for the $p_T^{\mu\mu}$ categories	61
7.2.2.2	Determination of the Mass Resolution	61
7.2.2.3	Background Model for the VBF category	61
7.2.2.4	Background Fit Results	63
8	Systematic Uncertainties	65
8.1	Experimental Systematic Uncertainties	65
8.1.1	Uncertainty of the Luminosity Measurement	65
8.1.2	Pile-up Reweighting	65
8.1.3	Muon Trigger, Reconstruction and Identification Uncertainties	65
8.1.3.1	Muon Trigger Uncertainties	66
8.1.3.2	Muon Reconstruction and Identification Uncertainty	66
8.1.4	Jet and Missing Transverse Energy Related Uncertainties	66
8.1.5	Experimental Systematic Uncertainties for the Standalone Analysis	66
8.1.6	Experimental Systematic Uncertainties Summary for the Combined Analysis	67
8.2	Theoretical Systematic Uncertainties	67
8.2.1	Higgs Boson Production Cross Section Uncertainty	67
8.2.1.1	Gluon-Fusion Production Mode	67
8.2.1.2	Vector-Boson Fusion Production Mode	67
8.2.1.3	Production through Higgs-strahlung	69
8.2.2	Branching Ratio Uncertainty	70

8.3	Methodical Systematic Uncertainties	71
8.3.1	Signal Acceptance Systematic Uncertainties	71
8.3.1.1	Acceptance Uncertainties of the Standalone Analysis	71
8.3.1.2	Acceptance Uncertainties of the Combined Analysis	79
8.3.2	Spurious Signal Method	81
8.3.2.1	Spurious Signal in a Nutshell	81
8.3.2.2	Generator-Level Smeared Background Samples	82
8.3.2.3	Spurious Signal Results	86
9	Statistical Methods	91
9.1	Likelihood Definition	91
9.2	Test Statistic and Sampling Distribution	91
9.3	Modified Frequentist Confidence CL_S	92
9.4	Inclusion of Systematic Uncertainties	93
10	Results	95
10.1	Standalone Search Results	95
10.2	Combined Search Result	97
10.3	Comparison with CMS	99
10.4	Embedding into other ATLAS Higgs Results	99
11	Summary and Outlook	101
A	Auxiliary Information on Conventions and Units	103
B	Monte Carlo Simulated Samples	105
B.1	Samples for the Standalone Analysis	105
B.1.1	Background Samples	105
B.1.2	Signal Samples	109
B.2	Samples for the Combined Analysis	111
B.2.1	7 TeV Background Samples	111
B.2.2	7 TeV Signal Samples	115
C	Auxiliary Information on the Muon Resolution Model	117
	Bibliography	121
	List of Figures	129
	List of Tables	131

1 Introduction

The field of elementary particle physics can be seen as a consequence of the inherent quest of mankind for explanations for phenomena in nature. Though being remarkably successful and mathematically appealing in its simplicity and form, the underlying theory, the Standard Model of particle physics (SM), is the product of a decade-long complicated journey of physicists trying to explain the structure of matter and the nature of fundamental interactions. During that journey, which began in the early 20th century, there had been times when the theoretical foundation lagged behind experimental findings. For example, the first modern particle accelerators produced a multitude of unknown new particles in the 1950s, whose structure and classification only became clear with the development of the quark model by Gell-Mann and Zweig in 1964 [1]. On the other hand, theoretical predictions were beyond the scope of experiments on several occasions, such that e.g. the Z and W bosons were predicted already in the late 1950s and early 1960s [2, 3], but were not discovered experimentally until 1983 [4, 5]. A similar situation governed one sector of the SM for almost 50 years: The Brout-Englert-Higgs mechanism [6–9], which provides an elegant way to include otherwise forbidden mass terms for gauge bosons and fermions into the SM, also predicted a massive fundamental scalar particle, the Higgs boson. The search for this particle lasted almost half a century, until July the 4th 2012, when the ATLAS and CMS collaborations announced the discovery of a resonance with a mass of approximately 125.5 GeV [10, 11].

However, the work is all but done with this discovery, as it raised further questions which need to be answered: Is the observed particle the SM Higgs boson? Are the couplings and properties such as spin and parity consistent with the expectations? Are there additional resonances which give a hint to an extended Higgs sector? Recent analyses of Higgs boson decay signatures into pairs of photons, b -quarks, Z and W bosons and the di-tau final state, carried out at both the ATLAS and the CMS experiment, do not exhibit significant deviations from the Standard Model prediction [12–17].

This thesis is part of the effort of the high energy particle physics community to pin down the properties of the discovered boson, and to exclude additional SM Higgs-like resonances with other masses. Here, the search for the decay of a SM Higgs boson into a muon pair is presented, using datasets of proton-proton collisions recorded by the ATLAS detector in 2011 and 2012 at center-of-mass energies of $\sqrt{s} = 7$ TeV and 8 TeV. The search is logically split into two analyses: The standalone investigation of the 8 TeV dataset, and a refined analysis of the combined 2011+2012 datasets. In both of these, the dimuon invariant mass spectrum is examined for a signal signature with Higgs boson mass hypotheses in a range between 110 GeV and 150 GeV.

This document is structured as follows:

Chapter 2 introduces the Standard Model, the theoretical framework in which this search is embedded. The focus is placed on electroweak symmetry breaking and the Higgs mechanism, with a phenomenological review of the expected dimuon invariant mass spectra of the signal and the main background processes.

Chapter 3 gives an overview of the experimental setup used to obtain the dataset, outlining the LHC accelerator and describing the ATLAS detector.

Chapter 4 elaborates on the concepts of Monte Carlo simulation of collision events, a crucial method to estimate and predict observables in general and the event kinematics of the dimuon topology in particular for this analysis.

Chapter 5 describes the collection of muon reconstruction algorithms employed throughout the ATLAS collaboration and utilised for this search.

Chapter 6 presents a detailed description of the event selection, outlining the similarities and the differences between the standalone and the combined analysis selections and the motivation behind them.

Chapter 7 is dedicated to the development and validation of analytic models for the signal and background components of the investigated invariant mass spectrum.

Chapter 8 focusses on the categorisation and quantification of systematic uncertainties associated to the analyses.

Chapter 9 describes the statistical concepts used to interpret the observed data.

Chapter 10 collects the results obtained from the standalone and the combined searches, and puts them into the context of the Higgs boson observation and the results of other experiments.

2 Theoretical Foundations

This chapter will introduce the theoretical foundations of the currently established theory of elementary particles and their interactions, referred to as the Standard Model of particle physics. After an introduction of the SM, the focus is placed on the electroweak sector and the Higgs mechanism of spontaneous symmetry breaking. The last section of this chapter is dedicated to phenomenological considerations, focussing on dimuon final states of proton-proton collisions.

2.1 The Standard Model of Particle Physics

Despite its humble name, the SM is a sophisticated and powerful theory able to describe particle physics phenomena at a great variety of energy scales to an excellent degree of precision. This section will introduce the SM as a quantum field theory. First, its particle content and the interactions are introduced. Then, the electroweak interaction and the Higgs mechanism will be described in greater detail.

2.1.1 Particles and Interactions

The fundamental particles of the SM are spin $\frac{1}{2}$ fermions. They are grouped in quarks and leptons, the former participating in the strong interaction, while the latter do not. So-called up-type and down-type quarks (or leptons, respectively) are further combined as isospin doublets of the weak interaction. This doublet structure is repeated three times for both quarks and leptons forming three generations of fundamental fermions, resulting in a total of six quarks and six leptons. An overview of the fermion generations and their electroweak quantum numbers is given in Table 2.1. For each particle, there exists a corresponding antiparticle with the same properties, except that all charges switch sign. The inter-

	generation			quantum number		
	I	II	III	I_3^W	Y	Q
up-type leptons	$L = \begin{pmatrix} \nu_e \\ e^- \end{pmatrix}_L$	$\begin{pmatrix} \nu_\mu \\ \mu^- \end{pmatrix}_L$	$\begin{pmatrix} \nu_\tau \\ \tau^- \end{pmatrix}_L$	$+\frac{1}{2}$	-1	0
down-type leptons				$-\frac{1}{2}$	1	-1
up-type quarks	$Q = \begin{pmatrix} u \\ d' \end{pmatrix}_L$	$\begin{pmatrix} c \\ s' \end{pmatrix}_L$	$\begin{pmatrix} t \\ b' \end{pmatrix}_L$	$+\frac{1}{2}$	$+\frac{1}{3}$	$+\frac{2}{3}$
down-type quarks				$-\frac{1}{2}$	$+\frac{1}{3}$	$-\frac{1}{3}$
right-handed leptons	(ν_{eR})	$(\nu_{\mu R})$	$(\nu_{\tau R})$	0	0	0
	e_R	μ_R	τ_R	0	-2	-1
right-handed quarks	u_R	c_R	t_R	0	$+\frac{4}{3}$	$+\frac{2}{3}$
	d'_R	s'_R	b'_R	0	$-\frac{2}{3}$	$-\frac{1}{3}$

Table 2.1: The fundamental fermions in the Standard Model and their electroweak quantum numbers: the third component of the weak isospin I_3^W , the weak hypercharge Y and the electric charge Q [18]. The left-handed particles are combined into weak isospin doublets, whereas the right-handed particles remain singlets.³

actions contained in the SM are the strong, the weak and the electromagnetic force. Mathematically, they are described by inner (or gauge) symmetries of the Lagrange density⁴ \mathcal{L} with respect to a local gauge transformation, determined by a corresponding symmetry group. Each interaction is associated with a corresponding charge, and only particles carrying the respective charge take part in the interaction. The SM Lagrangian is symmetric under local $SU(3)_C \times SU(2)_L \times U(1)_Y$ transformations. The

³The hypothetical right-handed neutrinos ν_R carry no charge and would not participate in any interaction.

⁴For the rest of this discussion, the correct term *Lagrange density* will be abbreviated with the term *Lagrangian*, which is commonly used as a synonym.

dynamics implied by $SU(3)_C$ are called Quantum Chromodynamics (QCD), describing the interaction of quarks via the strong interaction. The associated gauge bosons are eight gluons. Having colour charge themselves, they do self-interact, which causes the potential between two coloured objects to rise with spatial distance. This results in the so-called confinement of QCD, essentially stating that no free colour charges (i.e. free quarks) can be observed.⁵ The three gauge bosons of $SU(2)_L$ (W^1, W^2, W^3) and the single one associated with $U(1)_Y$ (B) are not physically observable, but mix to form the three physical gauge bosons of the weak interaction, W^\pm and Z^0 , and the photon γ , the mediator of the electromagnetic force. For details of electroweak mixing, see section 2.1.2.1. Table 2.2 gives an overview of the gauge bosons and their basic properties. Each gauge symmetry is associated with a unique gauge coupling

interaction	coupling constant ⁶	gauge boson	m [GeV]	Q
electromagnetic	$\alpha_{em} \simeq \frac{1}{127}$	photon γ	0	0
weak	$\alpha_W \simeq 0.034$	W-boson W^\pm	80.385	± 1
		Z-boson Z^0	91.188	0
strong	$\alpha_S \simeq 0.12$	8 gluons g	0	0

Table 2.2: The three fundamental interactions of the SM and the associated gauge bosons, including their basic properties mass m and electric charge Q [18].

g_S , g and g' for $SU(3)_C$, $SU(2)_L$ and $U(1)_Y$, respectively. Usually one defines a corresponding coupling constant $\alpha_i \doteq \frac{g_i^2}{4\pi}$. Despite their name, the couplings are not constant, but are a function of the scale Q^2 at which they are probed (usually the momentum transfer of a hard scattering process). This *running* of the coupling is particularly important for α_S , which rises with low scales rendering a perturbative ansatz for low-energy QCD calculations inappropriate. The running of the strong coupling is shown in Figure 2.1.

2.1.2 Electroweak Sector and the Higgs Mechanism

2.1.2.1 Electroweak Standard Model The electroweak sector of the SM was developed by Glashow, Salam and Weinberg in the second half of the 20th century [3, 19, 20]. The gauge group is the direct product of $SU(2)_L \times U(1)_Y$, leading to the Lagrangian for the gauge fields⁷ W_a^μ and B^μ :

$$\mathcal{L} = -\frac{1}{4}W_a^{\mu\nu}W_{\mu\nu}^a - \frac{1}{4}B^{\mu\nu}B_{\mu\nu}, \quad (2.1)$$

in which the field strength tensors $W_a^{\mu\nu}$ and $B^{\mu\nu}$ are defined as:

$$\begin{aligned} W_a^{\mu\nu} &= \partial^\mu W_a^\nu - \partial^\nu W_a^\mu - g\epsilon^{abc}W_b^\mu W_c^\nu, \\ B^{\mu\nu} &= \partial^\mu B^\nu - \partial^\nu B^\mu. \end{aligned} \quad (2.2)$$

The coupling of the gauge fields to the fermion fields is governed by the covariant derivative, which has the form:

$$D^\mu = \partial^\mu + igI_a W_a^\mu + ig'\frac{Y}{2}B^\mu. \quad (2.3)$$

Here g and g' are the coupling constants of $SU(2)_L$ and $U(1)_Y$, respectively, with the weak isospin \vec{I} and the weak hypercharge Y as the corresponding charges. The ratio of the couplings g and g' determines the weak mixing angle θ_w :

$$\tan \theta_w = \frac{g'}{g}. \quad (2.4)$$

⁵An exact mathematical proof for confinement is not yet available, due to the non-perturbative nature of the problem.

⁶The coupling constants are given at the momentum scale $Q^2 = M_Z^2$ [18].

⁷Throughout this section, Einstein's summation convention is implied.

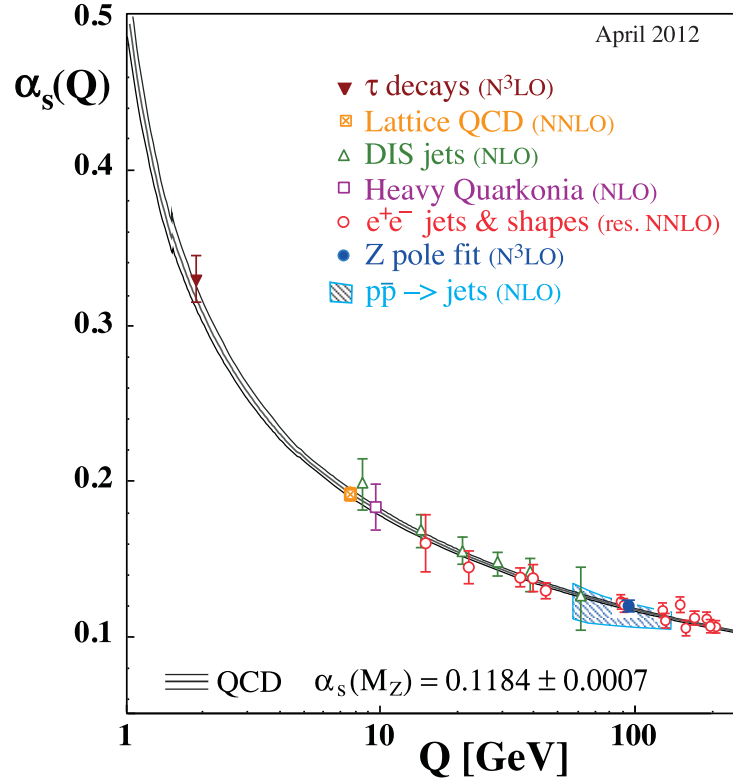


Figure 2.1: Dependence of the strong coupling constant α_s on the momentum transfer Q , with the world average value at $Q = M_Z$ given [18].

The physical observable bosons W^\pm of the charged weak interaction are linear combinations of W_1 and W_2 :

$$W_\mu^\pm = \frac{1}{\sqrt{2}}(W_{1,\mu} \mp iW_{2,\mu}), \quad (2.5)$$

and the neutral physical Z boson and photon γ are a mixture of W_3 and B :

$$\begin{pmatrix} Z_\mu \\ A_\mu \end{pmatrix} = \begin{pmatrix} \cos \theta_w & -\sin \theta_w \\ \sin \theta_w & \cos \theta_w \end{pmatrix} \begin{pmatrix} W_{3,\mu} \\ B_\mu \end{pmatrix}. \quad (2.6)$$

Experimental observation had shown that the charged weak interaction is maximal parity violating. This means that the W_μ^i fields only couple to left-handed fermion fields and right-handed antifermion fields, defined as:

$$\psi_L = \frac{1}{2}(1 - \gamma_5)\psi \quad \bar{\psi}_R = \bar{\psi}\frac{1}{2}(1 - \gamma_5). \quad (2.7)$$

In analogy, the right handed fermion and left-handed antifermion fields are defined as:

$$\psi_R = \frac{1}{2}(1 + \gamma_5)\psi \quad \bar{\psi}_L = \bar{\psi}\frac{1}{2}(1 + \gamma_5). \quad (2.8)$$

Here, γ_5 is the product of the Dirac matrices:

$$\gamma_5 = i\gamma_0\gamma_1\gamma_2\gamma_3. \quad (2.9)$$

With these definitions and Equations (2.1) and (2.3), the electroweak Lagrangian reads:

$$\mathcal{L}_{EW} = \bar{\chi}_L \gamma^\mu D_\mu \chi_L + \bar{\psi}_{1,R} \gamma^\mu D_\mu \psi_{1,R} + \bar{\psi}_{2,R} \gamma^\mu D_\mu \psi_{2,R} - \frac{1}{4} W_a^{\mu\nu} W_{\mu\nu}^a - \frac{1}{4} B^{\mu\nu} B_{\mu\nu}, \quad (2.10)$$

where the left-handed weak isospin doublet χ_L is defined as:

$$\chi_L = \begin{pmatrix} \psi_1 \\ \psi_2 \end{pmatrix}_L. \quad (2.11)$$

The fermion fields ψ_1 and ψ_2 hereby denote the isospin partners within a doublet (see Table 2.1). An important consequence of Equation (2.10) is that mass terms for both the boson fields as well as the fermion fields break the gauge symmetry, and therefore cannot be introduced ad hoc. However, experimental observation clearly showed that fermions and weak gauge bosons do have mass, and the theory had to be adapted to include mass terms.

2.1.2.2 The Higgs Mechanism The recipe to generate the mass terms dynamically for the weak gauge bosons in the electroweak Lagrangian is called spontaneous symmetry breaking (SSB). It was developed by Brout, Englert and Higgs in 1964 [6–8]. Mass terms for fermions were later added as Yukawa interaction terms by Weinberg in 1967 [19]. An additional scalar doublet field, the Higgs field Φ , is introduced as:

$$\Phi = \begin{pmatrix} \Phi^+ \\ \Phi^0 \end{pmatrix} = \begin{pmatrix} \phi_1 & +i\phi_2 \\ \phi_3 & +i\phi_4 \end{pmatrix}, \quad (2.12)$$

with four real scalar fields $\phi_{1\dots 4}$. With the following ansatz for the potential of Φ :

$$V(\Phi) = \mu^2 \Phi^\dagger \Phi + \lambda (\Phi^\dagger \Phi)^2, \quad (2.13)$$

the Lagrangian for the Higgs field takes the form:

$$\mathcal{L}_H = D_\mu \Phi D^\mu \Phi - V(\Phi). \quad (2.14)$$

The parameters μ and λ are free parameters, but SSB only occurs if $\mu^2 < 0$ and $\lambda > 0$. The potential (2.13) then has a nonzero minimum, the vacuum expectation value v :

$$v = \sqrt{\frac{-\mu^2}{\lambda}}. \quad (2.15)$$

In this minimum, one is free to choose the four fields as $\phi_1 = \phi_2 = \phi_4 = 0$ and $\phi_3 = \frac{v}{\sqrt{2}}$, such that Φ reads as:

$$\Phi \stackrel{!}{=} \Phi_0 = \frac{1}{\sqrt{2}} \begin{pmatrix} 0 \\ v \end{pmatrix}. \quad (2.16)$$

An expansion around this minimum of the form

$$\Phi_0 \rightarrow \Phi'_0 = \frac{1}{\sqrt{2}} \begin{pmatrix} 0 \\ v + H(x) \end{pmatrix}, \quad (2.17)$$

introduces the physical scalar Higgs boson field $H(x)$. Inserting Equation (2.17) into the Lagrangian (2.14) with the covariant derivative (2.3) yields both mass terms for the W^\pm and Z^0 bosons and the Higgs boson itself (for a complete derivation see e.g. [21]):

$$M_{W^\pm} = \frac{1}{2}vg \quad M_{Z^0} = \frac{1}{2}v\sqrt{g^2 + g'^2} \quad M_H = v\sqrt{2\lambda}. \quad (2.18)$$

Fermion masses are introduced via Yukawa coupling terms of the Higgs field Φ and the respective left- and right-handed fermion fields in a Yukawa Lagrangian \mathcal{L}_F [19]:

$$\begin{aligned} \mathcal{L}_F &= -\lambda_F \bar{\chi}_L \Phi \psi_R^2 \\ &= -\lambda_F \frac{1}{\sqrt{2}} (\bar{\psi}_{1,L}, \bar{\psi}_{2,L}) \begin{pmatrix} 0 \\ v + H \end{pmatrix} \psi_{2,R} \\ &= -\lambda_F \frac{1}{\sqrt{2}} (v + H) \bar{\psi}_{2,L} \psi_{2,R}, \end{aligned} \quad (2.19)$$

with the Yukawa coupling λ_F as an additional parameter for each fermion⁸. From (2.19) it can be seen that the fermion mass is proportional to the Yukawa coupling parameter λ_F . Similarly, the coupling of the fermion field ψ to the Higgs field H is proportional to λ_F and therefore proportional to the fermion mass. Thus, the Higgs boson couples stronger to heavy fermions than to light fermions.

2.2 Phenomenology of Dimuon Events

A convenient way to translate the mathematical structure of \mathcal{L} into cross-sections σ and decay rates Γ are Feynman diagrams. These depict schematically the process of interest, and allow to calculate the matrix element, or amplitude \mathcal{M} by applying vertex factors and propagators following the so-called Feynman rules, which are derived from the Lagrangian (for an introductory overview, see e.g. [22]). Both σ and Γ are proportional to the absolute square $|\mathcal{M}|^2$ of the matrix element times a phase space factor ensuring energy and momentum conservation⁹.

2.2.1 Dimuon Production at the LHC

The production of a muon pair in a hadronic collision was first described by Sidney Drell and Tung-Mow Yan [23], and is also known as Drell-Yan (DY) process. The Feynman diagrams contributing to the DY dimuon production are the quark-antiquark initiated exchanges of a photon (γ) or a Z -boson, quark-gluon scattering and gluon-gluon fusion, as shown in Figure 2.2. The cross-section for the production of

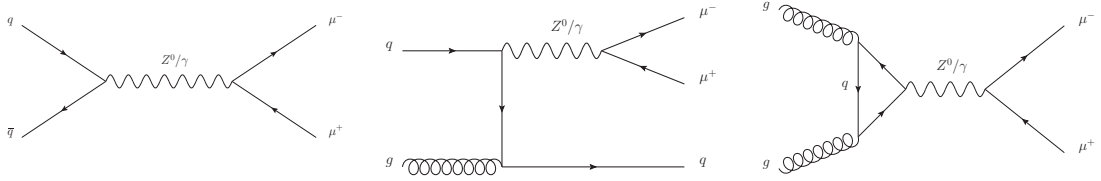


Figure 2.2: Dimuon production via quark-antiquark annihilation (left), quark-gluon-scattering (middle) and gluon-gluon fusion (right).

a muon-antimuon pair via quark-antiquark annihilation through photon exchange is [23]:

$$\sigma_{q\bar{q} \rightarrow \mu^+ \mu^-}(s) = \frac{4\pi\alpha_{em}^2}{9s} Q_i^2, \quad (2.20)$$

with the electromagnetic fine structure constant α_{em} (see section 2.1.1), the squared centre-of-mass energy $s = m_{\mu\mu}^2$ of the dimuon system and the charge of the initial quarks Q_i . With this relation, the differential partonic cross section $d\sigma/dm$ of the DY production of a muon pair with invariant mass $m_{\mu\mu}$ is proportional to

$$\frac{d\sigma}{dm_{\mu\mu}} \propto \frac{1}{m_{\mu\mu}^3}. \quad (2.21)$$

For the exchange of a Z -boson, one has to take the resonance effect into account, which is due to the Z -boson propagator going on-shell. This propagator:

$$G_Z(s) = \frac{g_{\mu\nu}}{s - M_Z^2 + iM_Z\Gamma_Z}, \quad (2.22)$$

enters the amplitude according to the Feynman rules, such that the cross section for the Z -boson exchange at leading order is proportional to:

$$\sigma_{q\bar{q} \rightarrow Z \rightarrow \mu^+ \mu^-}(s) \propto \frac{1}{(s - M_Z^2)^2 + M_Z^2\Gamma_Z^2}. \quad (2.23)$$

⁸Mass terms for the up-type fermion fields ψ_1 arise from the hermitean conjugate of Equation (2.19).

⁹This is known as *Fermi's Golden Rule*.

Again, s is the squared invariant mass of the muon pair, and the mass M_Z and width Γ_Z of the Z -boson are $M_Z = 91.19$ GeV and $\Gamma_Z = 2.50$ GeV [18]. The dimuon invariant mass lineshape of the quark-gluon scattering and gluon-gluon fusion diagrams are identical to the quark-antiquark annihilation process due to the lack of colour flow between the initial state and the leptonic final state¹⁰. Nevertheless, this picture of dimuon production is rather simplified, as the interference between γ and Z -boson is not taken into account. It is still sufficient for the presented analyses, as will be shown in section 7.2.

2.2.2 Higgs Boson Production and Decay

In principle, the same diagrams as for the DY dimuon production can be drawn for the production of a SM Higgs boson. The main difference is that the coupling strength of the Higgs boson depends on the mass of the involved particle (see section 2.1.2.2), such that the main contributions to the SM Higgs production cross-section involve diagrams with heavy quarks or gauge bosons, see Figure 2.3. These

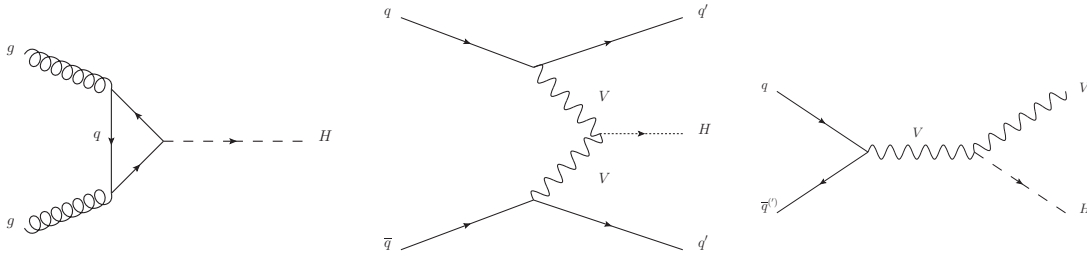


Figure 2.3: Dominant SM Higgs boson production modes at the LHC: gluon-gluon-fusion (left), vector-boson fusion (middle) and Higgsstrahlung (right). The symbol V stands for a W or Z -boson, respectively.

processes are labeled gluon-gluon-fusion (ggF), vector-boson fusion (VBF) and Higgsstrahlung. The ggF process dominates in terms of production cross-section, followed by VBF and to a lesser extent by Higgsstrahlung [24]. The production cross-sections as a function of the Higgs boson mass are shown in Figure 2.4.

The decay rate $\Gamma_{H \rightarrow f\bar{f}}$ of the SM Higgs boson into a pair of fermions is proportional to the spin-averaged square of the corresponding matrix element $\langle |\mathcal{M}|^2 \rangle$, which can be derived from the Lagrangian (2.19) as [25]:

$$\langle |\mathcal{M}|^2 \rangle = \frac{m_f^2}{v^2} (2m_H^2 - 8m_f^2), \quad (2.24)$$

leading to the fermionic decay width Γ at leading order of

$$\Gamma_{H \rightarrow f\bar{f}} = \frac{1}{8} \frac{m_f^2}{v^2} \beta^3 m_H, \quad (2.25)$$

where β is the fermion velocity $\beta = \frac{p}{E}$, which is very close to 1 for $m_H \gg m_f$. It can be observed from (2.25) that the decay width depends linearly on the Higgs boson mass at leading order, and that the partial width goes quadratically with the fermion mass. For the total decay width of the SM Higgs boson, the decays to gauge bosons have to be considered as well, which is more complicated due to subsequent gauge boson decays and loop-induced decays to $\gamma\gamma$ or gg . A complete discussion can be found e.g. in [26]. The dependence of the SM Higgs boson total and partial widths on its mass is shown in figure 2.5.

¹⁰Strictly speaking, this is only true at leading order, since quark loops contribute to the propagator at higher orders. This effect is small and will be neglected for the rest of this discussion.

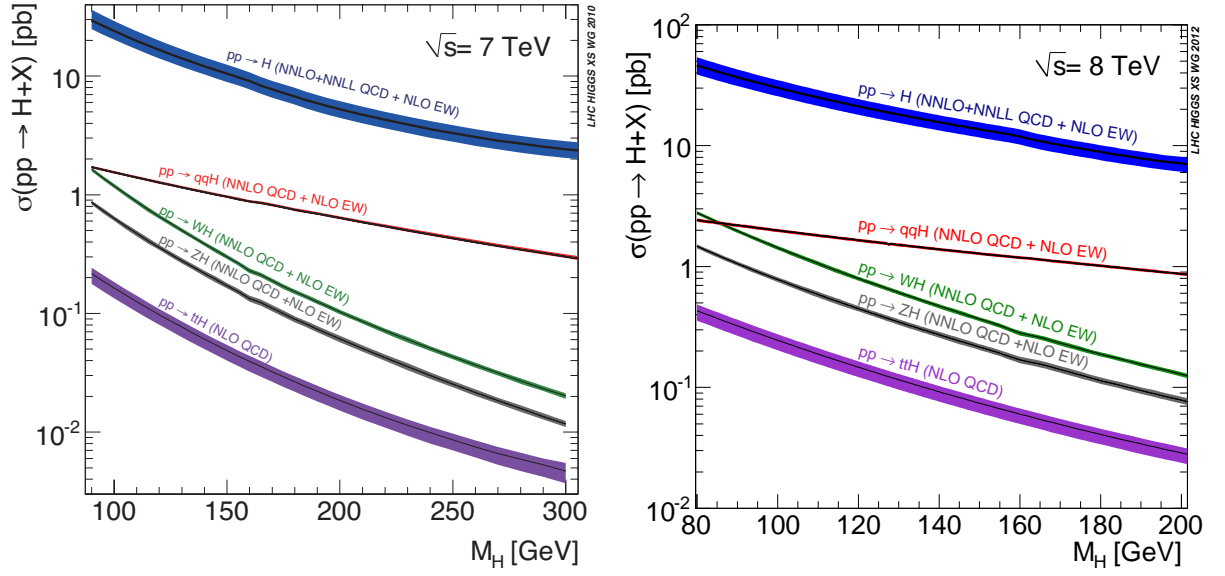


Figure 2.4: Production cross-sections for a SM Higgs boson versus mass, for different production modes. The left plot shows the cross-sections for a centre-of-mass energy of $\sqrt{s} = 7$ TeV, and the right plot depicts the cross-sections for $\sqrt{s} = 8$ TeV [24].

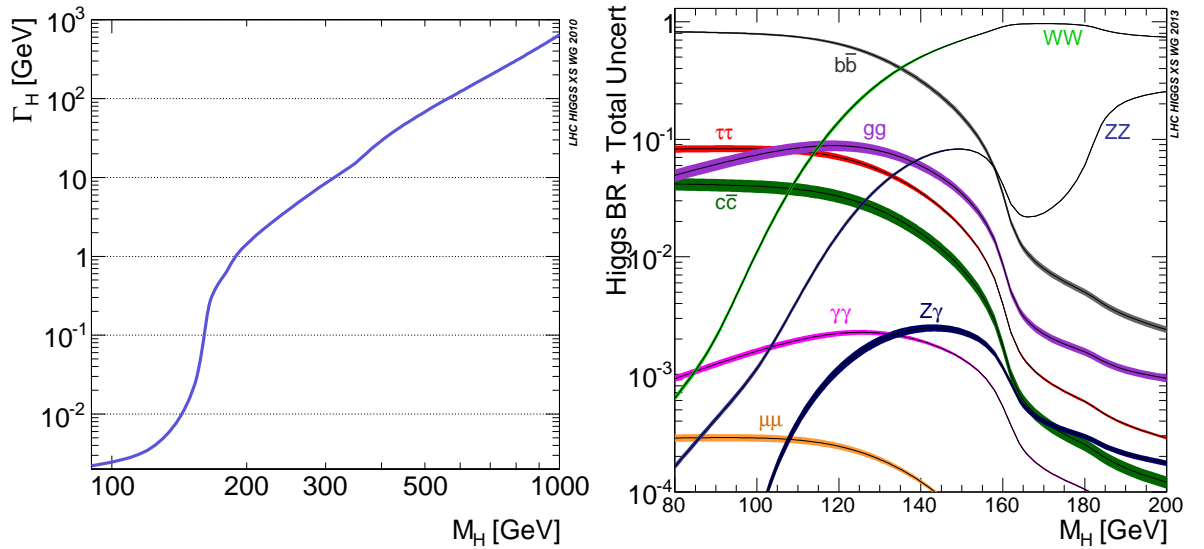


Figure 2.5: Total (left) and partial (right) width of the SM Higgs boson as a function of its mass [27]. The total width increases rapidly at the threshold for the production of a W boson pair.

3 Experimental Setup

In this chapter, the experimental setup will be introduced. At first, the particle accelerator complex, the Large Hadron Collider (LHC), will be briefly discussed. After that, the ATLAS detector will be described in detail, outlining its subdetectors and data-taking technologies.

3.1 The LHC

The Large Hadron Collider [28] is a circular particle accelerator located at the European Organisation for Nuclear Research (CERN, from the French Conseil Européen pour la Recherche Nucléaire) at the Franco-Swiss border near Geneva, Switzerland. It is a proton-proton collider housed in the tunnel of its predecessor machine, the Large Electron-Positron collider (LEP). With a circumference of almost 26.7 km and a design centre of mass energy of $\sqrt{s} = 14$ TeV for proton-proton collisions, it is currently the world's most powerful particle accelerator machine. An alternative run mode with lead nuclei instead of protons is also possible, with a per-nucleon energy of up to 2.76 TeV. The LHC consists of 8 straight sections which mainly serve the acceleration and aperture correction of the beams, and 8 arc sections, where a total of 1232 superconducting dipole magnets keep the beams on their nominal trajectory by providing a magnetic field of up to 8.33 T. Each proton beam consists of up to 2808 bunches, each containing up to 10^{11} protons. With according additional beam parameters, this corresponds to a design instantaneous luminosity¹¹ of $10^{34} \text{ cm}^{-2}\text{s}^{-1}$ for the two high-luminosity experiments ATLAS and CMS.

To achieve such high energies, a system of pre-accelerators is used to deliver protons with an energy of 450 GeV to the LHC machine. From a hydrogen source, protons are extracted and ramped up to 50 MeV with the LINAC (LINear ACcelerator). These are boosted to 1.4 GeV by the PSB (Proton Synchrotron Booster) and fed into the PS (Proton Synchrotron) and SPS (Super Proton Synchrotron), where they reach their injection energy of 450 GeV. The LHC then accelerates the beams to their design energy of 7 TeV, which takes approximately 20 minutes. A schematic view of the LHC accelerator complex with its pre-accelerators is shown in Figure 3.1.

Shortly after its first start of operations in 2008, a quench in one superconductive junction between the dipole magnets lead to a major incident, in the course of which the LHC had to be shut down for more than a year. Operation and data taking started again in 2009 with a reduced centre of mass energy of 900 GeV. In 2010 and 2011, operation continued at a centre of mass energy of 7 TeV. For the 2012 data taking period, the centre of mass energy was increased to 8 TeV.

3.2 The ATLAS Detector

The ATLAS Detector is one of the two multi-purpose particle physics experiments housed at the LHC. It follows a cylindric shape 4π solid angle hermetic detector design consisting of onion-like shells of subdetector systems to ensure particle detection and identification for a variety of physics analyses over almost the full phase space. The subdetector systems can be grouped into three parts:

- Inner Detector Tracking System
- Calorimeter System
- Muon Spectrometer.

Besides, a robust and efficient trigger system is required to cope with the high bunch crossing rate of 40 MHz. Furthermore, the ATLAS detector includes a complex magnet system which bends trajectories of charged particles, enabling a measurement of the particle momenta. The following sections will elaborate on the subdetector systems, with a stronger focus on the muon spectrometer which plays a crucial role for this analysis. In the beginning, an introduction to the coordinate system used in ATLAS is given.

¹¹See Appendix A

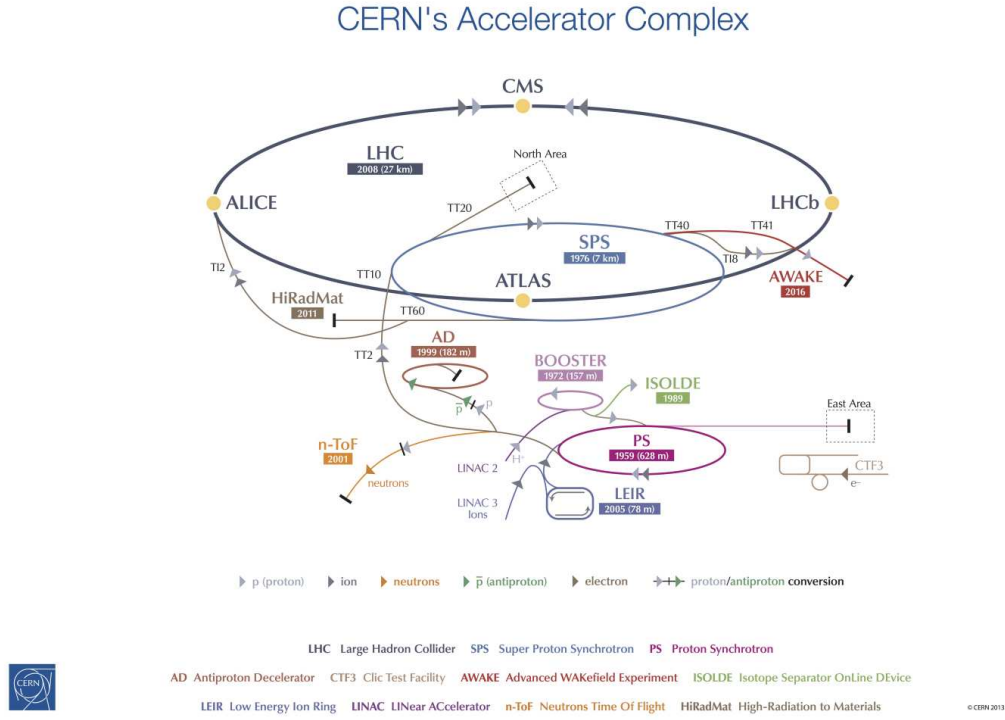


Figure 3.1: Schematic view of the LHC accelerator complex at CERN [29]. The LHC storage ring is shown in dark blue, the various pre-accelerator stages are also shown.

3.2.1 ATLAS Coordinate System

The coordinate system used throughout ATLAS is defined as a right-handed cartesian coordinate system, with the x coordinate pointing towards the centre of the LHC accelerator ring, the y axis pointing towards the surface and the z component pointing along the beam line. Usually, particle trajectories are expressed in polar coordinates reflecting the detector geometry, such that angular coordinates are introduced as follows:

- ϕ - polar angle in the x - y -plane, range: $[-\pi, \pi]$
- θ - angle in the z - y -plane, range: $[0, \pi]$.

For convenience, the *pseudorapidity* η , defined as

$$\eta = -\ln \tan \frac{\theta}{2}, \quad (3.1)$$

is used instead of the angle θ . The pseudorapidity corresponds to the rapidity y in the limit of ultrarelativistic particles, which is defined as:

$$y = \frac{1}{2} \ln \frac{E + p_z}{E - p_z}. \quad (3.2)$$

The differential hadron production cross-section $\frac{d\sigma}{dy}$ is invariant under Lorentz-boosts, and the flux of particles produced in hadron collisions is approximately constant in y . As a distance measure in the $\eta - \phi$ -plane, the quantity ΔR is defined as:

$$\Delta R = \sqrt{(\Delta\eta)^2 + (\Delta\phi)^2}, \quad (3.3)$$

with $\Delta\eta$ and $\Delta\phi$ being the distance of two objects in η and ϕ , respectively. Further, the momentum of an object in the transverse plane is commonly used. It is defined as

$$p_T = \sqrt{p_x^2 + p_y^2}. \quad (3.4)$$

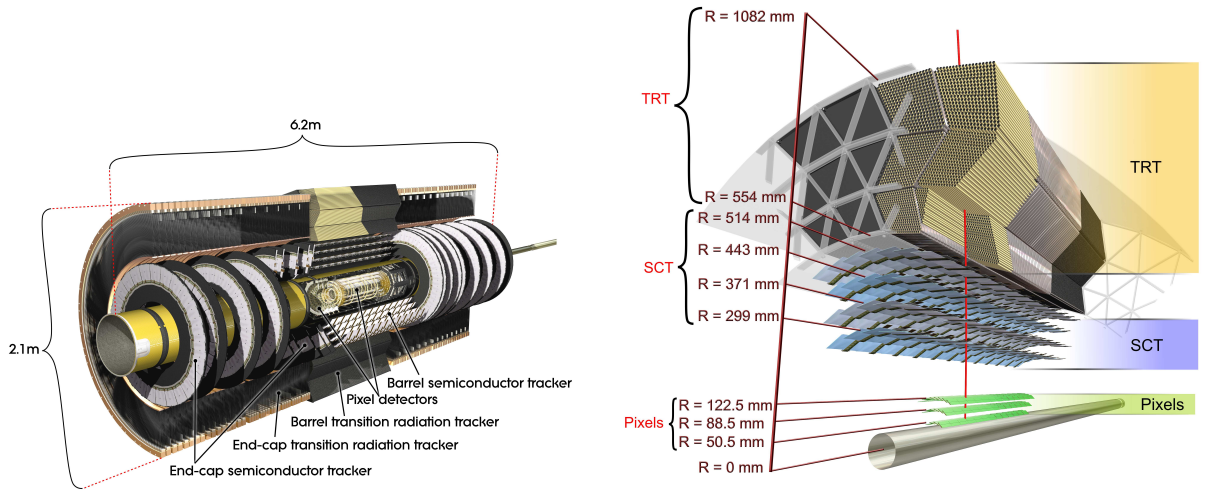
The reason to prefer the transverse momentum over individual momentum components is the following. In proton-proton-collisions, the colliding partons carry an unknown fraction of the protons' momentum, thus the initial longitudinal momentum p_z of the collision is unknown. Albeit, the transverse momentum of the colliding partons is negligibly small, justifying the approximate momentum conservation in the transverse plane: $\sum p_T \approx 0$.

Together with an object's energy E , the transverse momentum and the two angular coordinates η and ϕ completely determine the object's four-momentum vector in this particular base:

$$p_\mu = (p_T, \eta, \phi, E)^T. \quad (3.5)$$

3.2.2 Inner Detector Tracking System

The inner detector tracking system is the detector part closest to the beam pipe and nominal interaction point. It has to cope with extremely high particle densities of up to 1000 particles per collision taking place every 50 ns during the 2012 data taking period, and still ensure a high momentum and vertex resolution. Three subdetectors utilising different technologies are installed to meet these requirements: the pixel detector, the semiconductor tracker and the transition radiation tracker. Figure 3.2 displays a schematic view of the ATLAS inner detector and its components. The whole inner detector is embedded in a 2 T magnetic field generated by the central solenoid magnet (c.f. sec. 3.2.5).



(a) Cut-away view of the inner detector showing its components and dimensions.

(b) Schematic view of the inner detector barrel being crossed by a high-energetic charged particle (red line). The different subdetector systems and their dimensions are shown.

Figure 3.2: The ATLAS inner detector system [30].

3.2.2.1 Pixel Detector Being the innermost part of the ATLAS detector, the pixel detector is composed of three barrel layers at radii between 50.5 mm and 122.5 mm from the beam line extending ± 400.5 mm in z direction, and three end-cap circular discs with radii of 88.8 mm – 149.6 mm situated at z distances between 495 mm – 650 mm from the nominal interaction point, covering a pseudorapidity range of $|\eta| < 2.5$. A silicon junction diode with a depletion bias voltage applied serves as active sensor. Charged particles passing the depletion volume of a pixel create electron-hole-pairs via ionisation, and the electrons drift to the cathode where the signal is read out by a bump bond [31]. The different geometrical setup of the barrel and endcap parts of the pixel detector lead to different spatial resolutions. The barrel layers are designed to reach a resolution of 10 μm in the $R - \phi$ plane and 115 μm in z direction,

whereas the endcap disks have a design resolution of $10\text{ }\mu\text{m}$ in the $z-\phi$ plane and $115\text{ }\mu\text{m}$ in R direction. Fig. 3.3 shows a cut-away view of the ATLAS pixel detector.

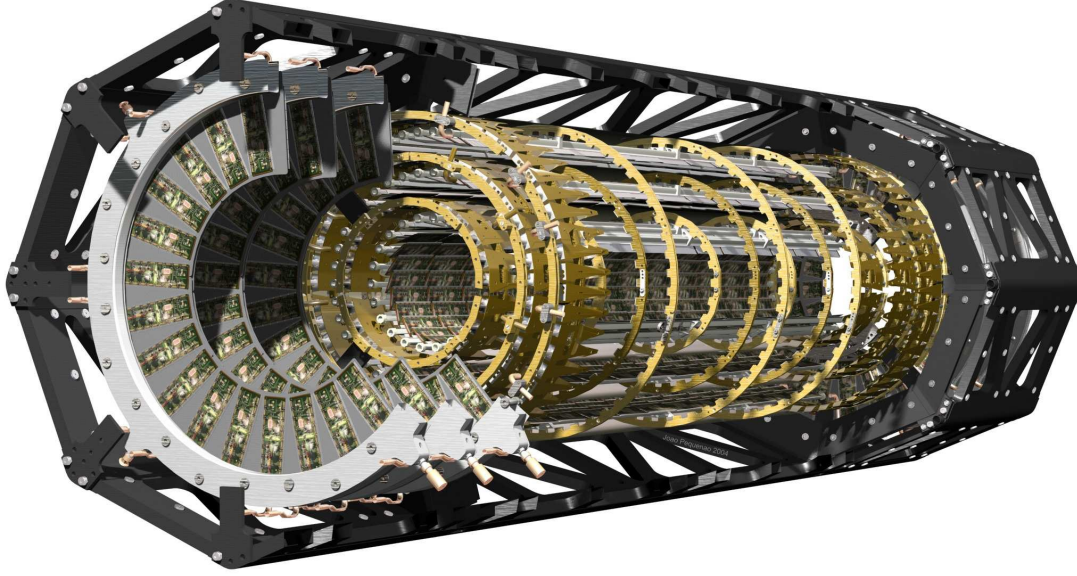


Figure 3.3: Schematic view of the ATLAS pixel detector including support structures for the barrel layers and endcap wheels. [30]

3.2.2.2 Semi Conductor Tracker The semi conductor tracker (SCT) is the second silicon-based tracking detector system of ATLAS. It consists of four double-layers of silicon strips at radii between 299 mm and 514 mm in the barrel section and nine end-cap wheels on each side of the barrel at distances in z direction between 839 mm and 2735 mm from the coordinate origin. Each sensor module consists of two 6.4 cm long silicon strips with a pitch of $80\text{ }\mu\text{m}$, utilising a single sided p-in-n technology with AC-coupled readout. The two strips are mounted at a small stereo angle of 40 mrad to measure a crossing track in two dimensions. With this design, the barrel SCT layers achieve an intrinsic resolution of $17\text{ }\mu\text{m}$ in the $R-\phi$ plane and $580\text{ }\mu\text{m}$ in z direction, whereas the endcap discs reach an overall resolution of $17\text{ }\mu\text{m}$ in the $z-\phi$ plane and $580\text{ }\mu\text{m}$ in R [31].

3.2.2.3 Transition Radiation Tracker The outermost part of the ATLAS inner detector tracking system is the transition radiation tracker (TRT). In contrast to the pixel and SCT detectors, it consists of gas-filled straw tubes with a tungsten-rhenium wire in its center set to positive high voltage. A passing charged particle ionises the gas mixture, causing electrons to drift towards the cathode wire. An avalanche close to the wire due to the high electric field leads to a measurable signal. Precise measurement of the entrance point of the particle into the straw tube is possible due to the drift time measurement and constant drift velocity of the electrons. In addition, polypropylene foils are mounted between the straw tubes. Thus, charged particles emit transition radiation because they cross many layers with different refraction indices, and the transition radiation photons add an additional energy component to the measurement. This is used to distinguish electrons from charged pions over a large energy range [31].

In the barrel part of the TRT, the 144 cm long straws are bundled in three layers in radii of 554 mm–1082 mm, allowing a track measurement in the $R-\phi$ plane with an accuracy of $130\text{ }\mu\text{m}$. The endcap TRT consists of radially arranged straws with a length of 37 cm between distances in z direction of 848 mm–2710 mm from the coordinate origin. In the endcap, the TRT provides a track measurement in the $z-\phi$ plane with an intrinsic resolution of $130\text{ }\mu\text{m}$. Contrary to the other two inner detector parts, the TRT extends only to a pseudorapidity of $|\eta| = 2.0$, but delivers a mean of $\langle N \rangle = 35$ straw hits per track.

3.2.3 Calorimeter System

The energy measurement of most of the particles created in a collision event is performed by the ATLAS calorimeter system. For this purpose, the particles are completely stopped within the detector volume, and the energy deposit is measured. Several subcomponents exist in the ATLAS calorimeter system to perform this measurement. The innermost part is the *electromagnetic* (EM) calorimeter for a precise measurement of electron and photon energies. It is surrounded by the *hadronic* calorimeter, whose purpose is to measure the energy of hadronically interacting particles. The ATLAS calorimeter is completed by the *forward calorimeter* (FCAL) which measures the energy of particles with a pseudorapidity up to $|\eta| < 4.9$. A schematic view of the complete calorimeter is shown in Fig. 3.4.

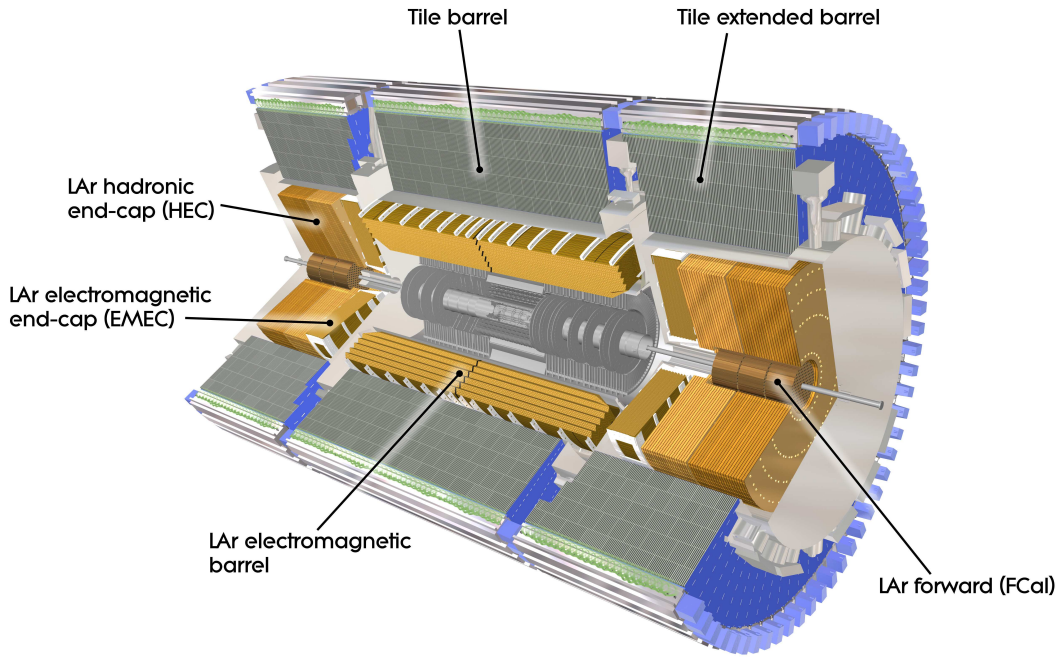


Figure 3.4: Schematic view of the ATLAS calorimeter system showing the barrel and endcap liquid argon calorimeter system in orange, and the hadronic tile calorimeter in grey. [30]

3.2.3.1 Electromagnetic Calorimeter The electromagnetic calorimeter consists of a barrel part and two endcaps on either side of the detector. The barrel in turn is split into two halves by a central gap at $\eta = 0$. The barrel electromagnetic calorimeter has an overall length of 6.4 m and extends between radii of 1.4 m–2.0 m, thus covering a pseudorapidity of $0 < |\eta| < 1.475$. The two endcap wheels are installed at longitudinal distances of $|z| = 3.74$ m from the coordinate origin. They each have a thickness of 0.63 m and inner and outer radii of $0.33 \text{ m} < R < 2.10 \text{ m}$, which corresponds to a pseudorapidity coverage of $1.375 < |\eta| < 3.2$. With this overlap, a smooth transition between the barrel and endcap regions is ensured. Lead absorber plates and liquid argon gaps equipped with copper electrodes alternate in an accordion-shape structure to achieve full coverage in ϕ avoiding cracks. High-energetic electrons and positrons traversing the absorber material emit photons via bremsstrahlung, and photons with sufficient energies split into electron-positron-pairs, such that an electromagnetic shower is generated. The electrons, positrons and photons of the shower ionise the liquid argon in the gaps, and the charge is collected by the electrodes.

The granularity of the electromagnetic calorimeter cells expressed in $\Delta\eta \times \Delta\phi$ ranges from 0.025×0.025 to 0.1×0.1 , depending on the detector region (for details see [32]). A fractional energy resolution of $\frac{\sigma_E}{E} \simeq 10\% / \sqrt{E}$ is reached by the electromagnetic calorimeter [31].

3.2.3.2 Hadronic Calorimeter Surrounding the electromagnetic calorimeter, the hadronic calorimeter's purpose is to stop and measure the energy of hadronically interacting particles which traversed the electromagnetic calorimeter. Different technologies are employed in the barrel and endcap part of the hadronic calorimeter. The hadronic tile barrel and extended barrel calorimeters consist of iron absorber plates interleaved with scintillating tiles, which are read out by wavelength-shifting fibres and photomultipliers. The barrel hadronic calorimeter covers a pseudorapidity range of $0 < |\eta| < 1.7$. This partly overlaps with the coverage of the endcap hadronic calorimeter wheels, which are able to detect hadronic showers in a pseudorapidity range of $1.5 < |\eta| < 3.2$. In contrast to the barrel and extended barrel tile calorimeter, the hadronic endcap utilises liquid argon as active material similarly to the electromagnetic calorimeter, but using copper instead of lead as absorber material. The granularity of the calorimeter cells is 0.1×0.1 to 0.2×0.1 in $\Delta\eta \times \Delta\phi$ in the tile barrel and extended barrel calorimeter, and 0.1×0.1 to 0.2×0.2 in the hadronic endcap, respectively. The fractional energy resolution of the tile calorimeters was measured to $\frac{\sigma_E}{E} \simeq (52 \pm 2)\% / \sqrt{E}$ [32], while the resolution of the hadronic endcap calorimeter is slightly worse with $\frac{\sigma_E}{E} \simeq (88 \pm 5)\% / \sqrt{E}$ [33].

3.2.3.3 Forward Calorimeter The ATLAS calorimeter system is completed with a forward calorimeter (FCal) employing the liquid argon technology as active material. It covers a pseudorapidity range of $3.1 < |\eta| < 4.9$. Due to the high particle flux in this region, the liquid argon gap size is smaller than in the electromagnetic calorimeters and the hadronic endcap calorimeter. For the first layer of the FCal, copper is used as absorber material, while for the second and third layer tungsten serves as absorber.

3.2.4 Muon Spectrometer

The ATLAS muon spectrometer has the highest volume of all ATLAS subdetector systems, forming its outermost part. The energy loss of a muon in the calorimeters is small compared to its total energy [18], so most of the muons produced in particle collisions traverse the whole ATLAS detector without being stopped. The purpose of the muon spectrometer is therefore to provide precise tracking information for muons traversing the ATLAS detector, independent from the Inner Detector tracker. This is achieved by a combination of high precision tracking chambers and fast responding trigger chambers. The former are called *Monitored Drift Tubes* (MDTs) and *Cathode Strip Chambers* (CSCs), and the latter technology is implemented as *Resistive Plate Chambers* (RPCs) and *Thin Gap Chambers* (TGCs). An overview of the ATLAS muon spectrometer is shown in Figure 3.5.

3.2.4.1 Monitored Drift Tubes The MDTs are the most widely used precision tracking detectors of the ATLAS muon spectrometer, installed to cover a pseudorapidity of $|\eta| \leq 2.0$. In the barrel part of the detector, up to $|\eta| = 1$, the MDTs are organised in three widely spaced cylindrical stations with radii of 5, 7 and 9.5 m, respectively. Additionally, there are four endcap MDT wheels on either side of the ATLAS detector, installed at distances z of 7.5, 10, 14 and 22 m from the interaction point. Each station in turn consists multiple chambers of closely-packed layers of drift tubes separated by a spacer. An example of one MDT chamber depicting the layer structure is shown in Figure 3.6. The number of layers in each station is given in Table 3.1. In total, there are 1194 MDT chambers in the ATLAS muon spectrometer, with ≈ 370000 readout channels in total. The basic component of the MDT chambers are aluminium drift tubes with a diameter of 30 mm, housing a 50 μm tungsten-rhenium anode wire at a potential of 3270 V in its centre. They are filled with a mixture of 93% Ar and 7% CO₂ at a pressure of 3 bar. A traversing muon ionises the gas mixture producing electron-ion pairs along its trajectory. The electrons then drift towards the anode wire, which is read out at one end with a system of current-sensitive amplifiers and an ADC. The maximum drift time is ≈ 700 ns [32]. Together with fast trigger chambers (c.f. section 3.2.4.3), the exact drift time and therefore the precise location where the particle entered the drift tube can be calculated. A single-tube resolution of 80 μm is reached in the bending plane of the muon spectrometer magnetic field (see section 3.2.5), resulting in an overall resolution of 40 μm for a MDT chamber exploiting the measurement in up to 8 individual tubes [34]. A high mechanical precision

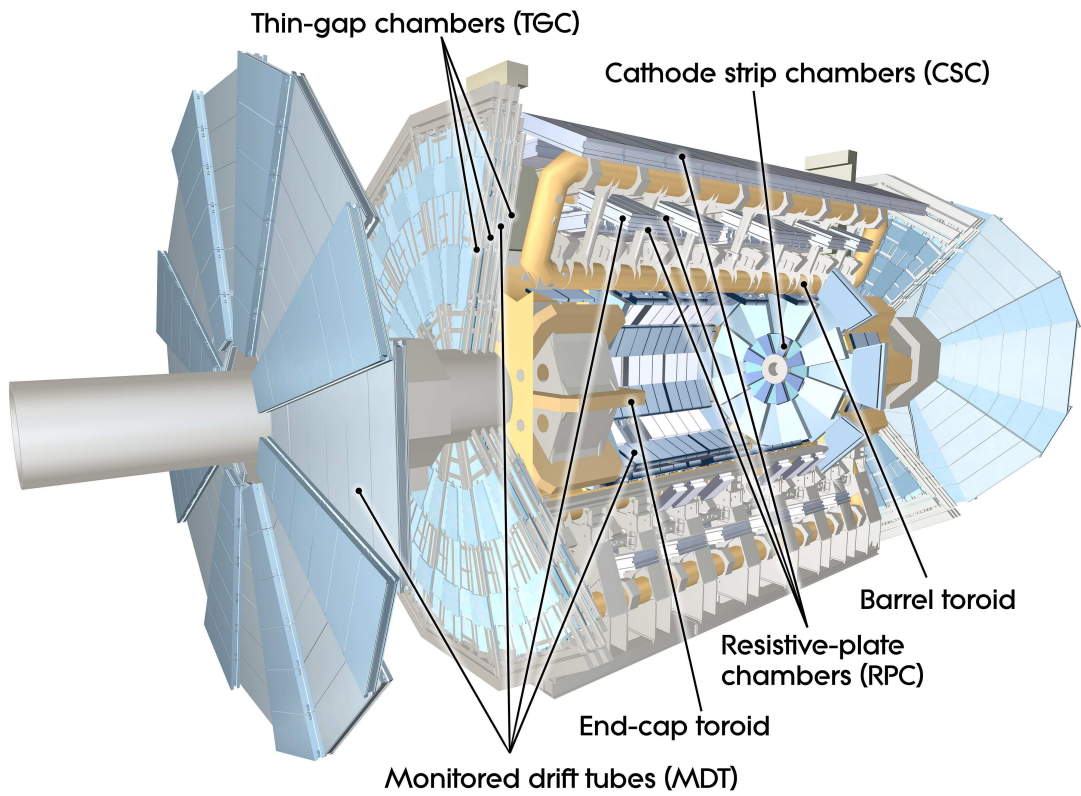


Figure 3.5: Schematic view of the ATLAS muon spectrometer detector depicting all its subcomponents. The muon spectrometer magnet system is also shown. [30]

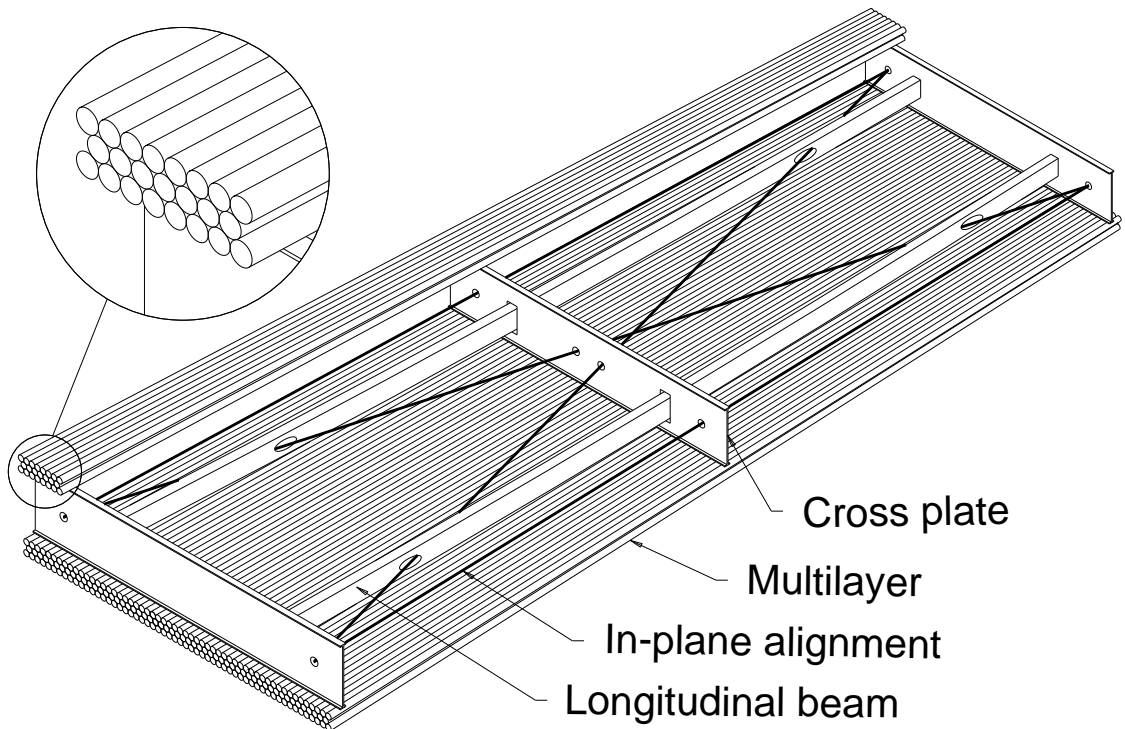


Figure 3.6: Schematic view of a MDT chamber with support structures [34].

station	layers
BI	2×4
BM	2×3
BO	2×3
EI	2×4
EE	2×3
EM	2×3
EO	2×3

Table 3.1: Number of drift tube layers and drift tubes in each MDT station [34]. Here BI, BM and BO name the barrel inner, middle and outer stations, respectively; and EI, EE, EM and EO denote the four endcap MDT station wheels from inside to outside.

is required to maintain this resolution, therefore the drift tube chambers are constantly monitored with an optical alignment system, which allows to correct for displacements and deformations due to e.g. gravitational sag and magnetic forces.

3.2.4.2 Cathode Strip Chambers In the innermost wheel of the endcap part of muon spectrometer, the high particle flux from the collisions would strongly degrade the performance and resolution of the monitored drift tubes, therefore an alternative instrumentation with cathode strip chambers is used. These cover the forward muon spectrometer at pseudorapidities between $2.0 < |\eta| < 2.7$ (see Figure 3.8). Cathode strip chambers are multi-wire proportional chambers filled with a mixture of 30% Ar, 50% CO₂ and 20% CF₄. The high admixture of the quenching gases CO₂ and CF₄ reduce uncontrolled avalanche buildup under high particle fluxes, which would otherwise degrade the spatial resolution. The precision measurement is performed by reading out and amplifying the charge induced on the segmented cathode by the avalanche formed on the anode wires, after an ionising particle crossed the gas volume. The high resolution is achieved by a special geometry of the anode wires and cathode strips: the anode-cathode spacing of 2.54 μm is equal to the anode wire pitch allowing for interpolation. Non-linearity in the interpolation due to the cathode pitch of 5.08 mm is overcome by exploiting capacitive coupling of two additional intermediate cathode strips between the readout strips. This design is depicted in Figure 3.7. The cathode strip chambers are organised in 2×4 layers forming the segments of the CSC wheels, providing up to eight precision measurement points for a single traversing particle. The spatial resolution in the bending plane of a single hit in a single CSC layer is 60 μm , leading to a combined resolution of 40 μm for the complete chamber segment [34].

3.2.4.3 Resistive Plate Chambers The RPC subdetector serves mainly two purposes: to provide a fast and accurate trigger system, and to measure the track coordinates in the non-bending plane complementary to the measurement in the precision chambers (MDT, see section 3.2.4.1 and CSC, c.f. section 3.2.4.2). RPC modules are installed in the barrel part of the muon spectrometer on both sides of the middle MDT station and above the outer MDT station, as can be seen in Figure 3.8. They cover a pseudorapidity range of $0 < |\eta| < 1.05$. RPCs are gas-filled parallel-plate detectors without electrodes inside the gas volume, operated in avalanche mode. This ensures high rate capability while maintaining excellent timing performance with a response time of less than 10 ns [34]. High-resistive bakelite plates with polycarbonate spacers of 2 mm thickness define the gas volume, which is filled with an admixture of 94.7% tetrafluoroethane (C₂H₂F₄), 5% butane and 0.3% sulfur hexafluoride (SF₆). The bakelite surface is covered with graphite electrodes, which provide a high voltage potential of 10 kV. An ionising particle traversing the gas volume creates free charges, which then build up an avalanche due to the strong electric field. This avalanche signal is read out via capacitive coupling by two orthogonal sets of

readout electrode strips, one on each side of the plates. One strip set is oriented such that it measures in the bending (η) coordinate, and orthogonal strips are used to measure the non-bending (ϕ) coordinate. The strip width varies from 30 mm to 39.5 mm throughout the detector. Two RPC layers with four strip sets in total form a RPC chamber.

The RPC detector readout is organised such that a fast muon trigger decision can be achieved. Dedicated front-end boards and readout chips on the detector provide a trigger decision with configurable p_T thresholds with a granularity of $\Delta\eta \times \Delta\phi = 0.1 \times 0.1$ by reading out the η and ϕ strips of different RPC stations within one sector. Further details of the muon trigger system are discussed in section 3.2.6.

3.2.4.4 Thin Gap Chambers Thin Gap Chambers follow a similar detector design as multi-wire proportional chambers, except that the anode-cathode distance is smaller than the anode wire pitch. They are operated in saturation mode with a high-quenching gas mixture of 55% CO_2 and 45% $n - \text{C}_5\text{H}_{12}$ within a potential of 3.1 kV [34], ensuring low sensitivity to mechanical deformations and only small dependence of the pulse height to the incident angle of the ionising particle. The small wire pitch of 1.8 mm leads to short electron drift times and a faster signal. TGCs cover the endcap muon spectrometer at pseudorapidities of $1.05 < |\eta| < 2.4$. Similarly to the RPCs, they provide both a fast trigger signal and the complementary measurement of the track coordinate in the non-bending direction. In the inner endcap wheel, one doublet of TGCs provides the non-bending measurement, whereas in the middle station one triplet and two doublet layers of TGCs ensure both the trigger and the secondary coordinate measurement. The location of the TGCs within the ATLAS muon spectrometer and the electrode structure within a TGC is shown in Figure 3.9. Several anode wires are grouped together with a common readout to form a trigger signal. The number of wires grouped this way varies with pseudorapidity to reach the desired constant trigger granularity.

3.2.5 Magnet System

The ATLAS detector houses a four-component superconducting magnet system, which provides a magnetic field bending the trajectories of charged particles crossing the detector volume. Thus, it is an essential component, enabling momentum and charge measurement in the inner detector and the muon spectrometer through the curvature of the tracks. A niob-titan composite embedded in an aluminium stabilizer is used as conductor in all of the superconducting magnets. Cooling in the magnet cryostats is provided through a steady flow of helium at 4.5 K. The central solenoid magnet surrounds the inner detector, and generates an average magnetic field of 2.0 T with a current of 7.6 kA [35]. The magnetic field in the muon spectrometer is provided by three large air-coil toroid magnets, one barrel toroid and

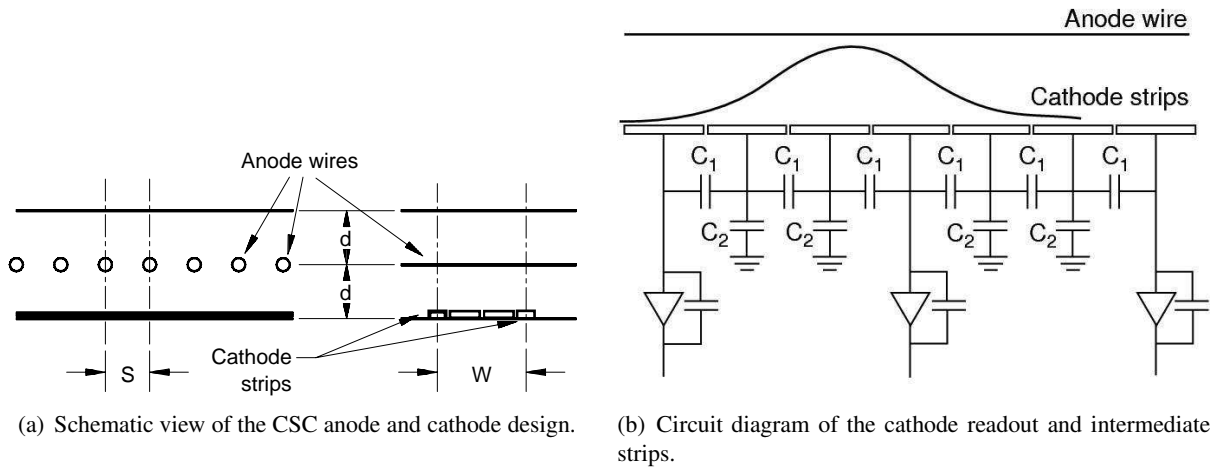


Figure 3.7: Schematic view of the CSC chamber electrode geometry [34].

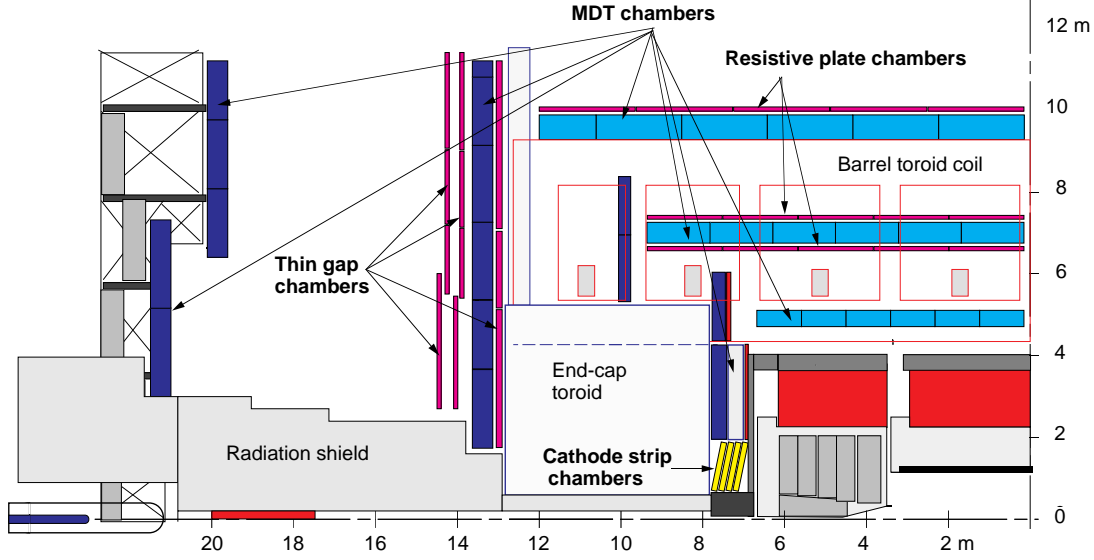
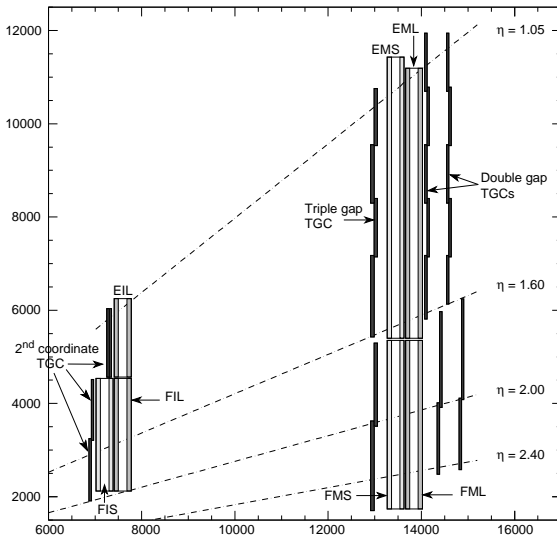
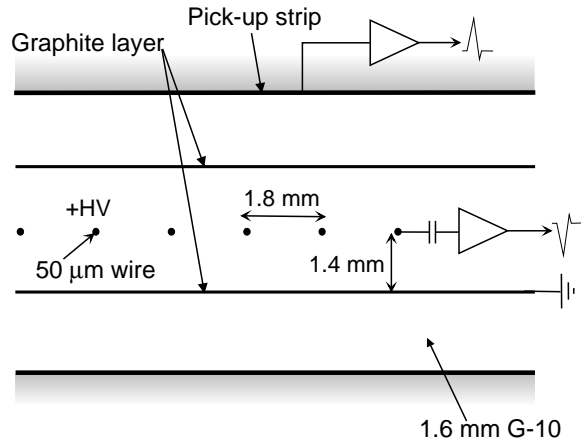


Figure 3.8: Side cut schematic view of one side of the ATLAS muon spectrometer [34]. The location of its subdetector components is shown.



(a) Location of TGCs in the endcap muon spectrometer.



(b) Schematic view of the gas gap and electrode instrumentation of a TGC.

Figure 3.9: Schematics of the ATLAS TGC subdetector [34].

two endcap toroids on either side of the detector. Each of the toroid magnets consists of eight coils, and a peak field strength of 3.9(4.1) T is reached in the barrel (endcap) magnets with a current of 20 kA [35]. However, due to the large volume of the muon spectrometer, the average field strength is between 0.5 T and 1 T, and even lower in the overlap region between the barrel and endcap toroids. Since a precise knowledge of the magnetic field is crucial for an accurate track reconstruction, the ATLAS magnetic field is constantly monitored and mapped. The superconducting coil system and an example of the magnetic field map are shown in Figure 3.10.

3.2.6 Trigger System

With a design event rate of 40 MHz and an average event size of 1.3 Mb, it is technically impossible to record and store every collision event taking place. Therefore, a sophisticated three-staged trigger system

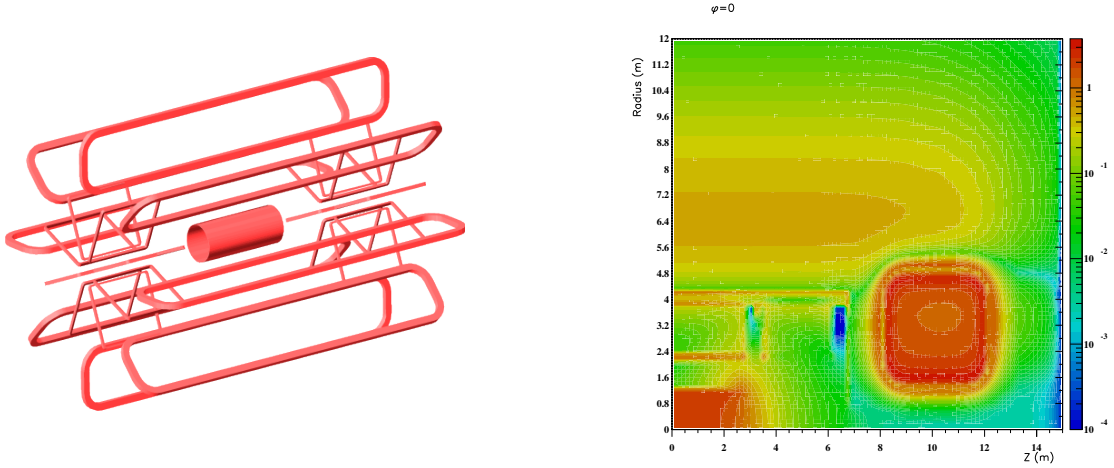


Figure 3.10: Schematic view of the central solenoid coil and the barrel and endcap toroid coils [35] (left), and slice of the magnetic field map at $\phi = 0$ (right) [34], showing the magnetic field strength in T color-coded.

is employed, effectively reducing the event rate to a moderate 200 Hz–400 Hz. The three trigger stages are called *Level 1* (L1), *Level 2* (L2) and *Event Filter* (EF). The latter two are also commonly referred to as *high level trigger* (HLT). Figure 3.11 shows the schematic dataflow of the whole trigger system. In the

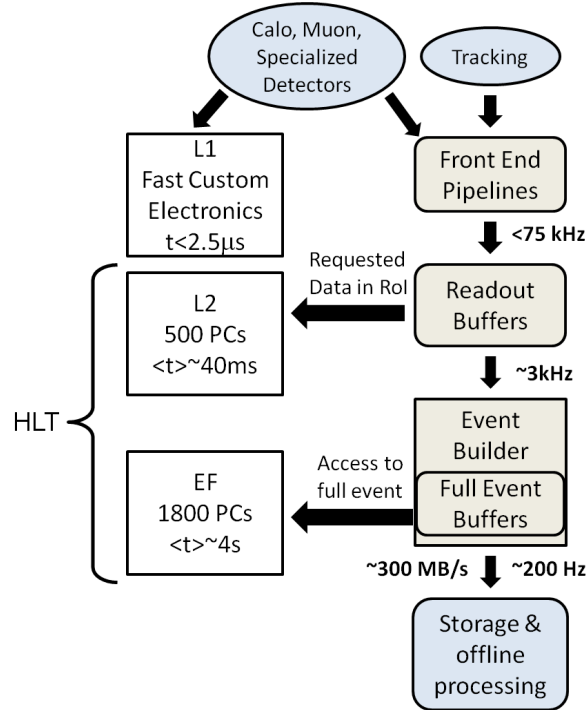


Figure 3.11: Scheme of the three-staged ATLAS trigger system [36]

L1 stage, specialised hardware is used to look for potentially interesting detector signatures with coarse granularity, such as high energy deposits in the calorimeter or coinciding hits in the muon spectrometer stations. Customisable thresholds can be programmed into the hardware. The average latency of the L1 trigger is $2.5 \mu s$, reducing the event rate to 75 kHz. If one of the L1 triggers delivers a positive result, it further defines a *region of interest* (ROI) in the detector, and passes it to the corresponding L2 trigger. This software-based trigger system has access to the full detector granularity inside the ROIs,

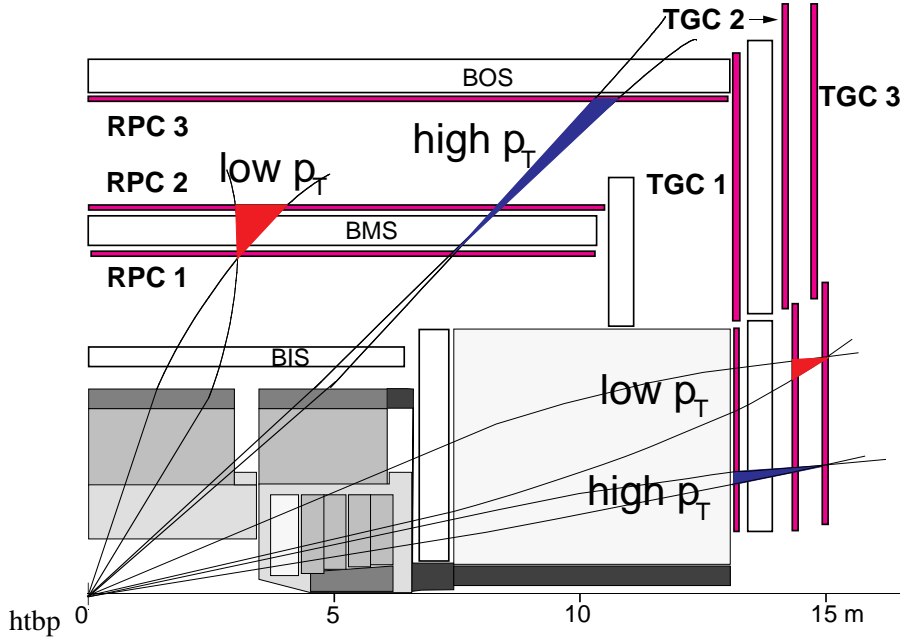


Figure 3.12: Definition of low and high transverse momentum L1 muon trigger items [38].

and dedicated trigger algorithms perform fast and basic object reconstruction, placing further cuts and thresholds to reach a decision whether to keep the event. It takes approximately 40 ms to reach this decision, which reduces the event rate to about 3.5 kHz. A positive answer by the L2 feeds the event to the EF stage, which executes a full event reconstruction with algorithms similar to the offline event reconstruction algorithms, accessing the complete detector information. This takes about 4 s for a single event and reduces the final event rate to about 200 Hz. While the trigger algorithms are busy, data from subsequent collisions is stored in readout buffers to await their decision.

3.2.6.1 Muon Trigger This section will give further details on the muon trigger system and algorithms.

L1 Muon Trigger The first stage of the muon trigger are dedicated hardware boards mounted directly on the muon trigger chambers (c.f. section 3.2.4.3, 3.2.4.4). Programmable coincidence matrix circuits look for coinciding hits in the RPC (TGC) layers of the barrel (endcap) muon spectrometer [37]. The number of detector layers with coinciding hits determines whether it is a low- p_T or high- p_T trigger as illustrated in Figure 3.12. A rough estimate of the curvature of the track is done via estimating the width of the geometrical trigger road through the detector layers, which is then used to put various transverse momentum thresholds. In total there are six p_T thresholds configured for the L1 muon trigger, three for both low and high transverse momentum. These are listed in Table 3.2.

L2 Muon Trigger The L2 muon trigger consists of dedicated software algorithms who are capable of performing very fast track reconstruction and momentum measurement. They use inner detector, calorimeter and muon spectrometer hit information inside the ROI defined by the L1 trigger. At first, a fast tracking algorithm reconstructs muon spectrometer tracks from MDT drift time information, making use of lookup tables to assign a momentum estimate to the track curvature, forming L2 *standalone* (SA) trigger items. These standalone tracks are further combined with tracks reconstructed in the respective inner detector ROI by an independent tracking algorithm, generating L2 *combined* (CB) trigger objects. The energy loss in the calorimeter is estimated from lookup tables. As a last step, information from the calorimeter cells in the vicinity of the estimated track path is evaluated, and surrounding inner detector tracks are taken into account, giving rise to *isolated* L2 muon trigger objects.

	p_T threshold [GeV]	item name
low- p_T	4	L1_MU4
	6	L1_MU6
	10	L1_MU10
high- p_T	11	L1_MU11
	15	L1_MU15
	20	L1_MU20

Table 3.2: Transverse momentum thresholds for the L1 muon trigger [39]

EF Muon Trigger At the event filter stage, the same muon reconstruction algorithms as in the offline event reconstruction are utilised (c.f. section 5), accessing the full detector readout information. The combined muon reconstruction algorithms, which start from muon spectrometer segments and extrapolate back to the inner detector to form combined muon trigger objects, are referred to as *outside-in* triggers, whereas segment-tagging algorithms starting from inner detector tracks are called *inside-out* triggers. At the EF, relative track isolation and compatibility of the muon track and inner detector track in the combination can also be used, resulting in *isolated* and *tight* EF muon triggers, respectively.

3.2.7 Luminosity Detectors

Two dedicated detectors are currently used to measure the luminosity online on a bunch-by-bunch basis: LUCID (LUminosti measurement using Cerenkov Integrating Detector) and the BCM (Beam Conditions Monitor). LUCID consists of an array of Cerenkov cones located on both sides of the ATLAS detector, at a distance $z = 17$ m from the nominal interaction point. The BCM is made from two pairs of horizontal and vertical diamond sensors on each side of the ATLAS nominal interaction point [40]. They are both capable of online luminosity measurement utilizing the proportionality between the luminosity and the visible inelastic scattering event rate [41].

The luminosity measurement is complemented by algorithms extracting the luminosity integrated over time by measuring the mean current from the ATLAS tile and forward calorimeters, which is proportional to the mean particle density traversing the detector. Dedicated van-der-Meer beam separation scans are used to calibrate the luminosity measurement [42].

4 Event Simulation

The simulation of events using Monte Carlo (MC) techniques is crucial in every stage of a high energy physics experiment. During the planning and commissioning phase, the simulations help to find the best solutions regarding detector efficiency, resolution and not least cost efficiency. For physics analyses, MC simulation is widely used to estimate the sensitivity, selection efficiency and expected discovery potential. Thus, the simulation can be used to optimise the analysis before actually looking at the real data. The first part of this chapter will outline the basic concepts of MC event simulation. Then, the most important event generators used in the analyses are introduced.

4.1 Concepts of Monte Carlo Simulation in Particle Physics

For an experimental particle physicist, MC simulation of the simulation of collision events should be able to handle a specific initial state (i.e. protons colliding at a defined centre-of-mass energy), and provide the detector response to the desired final state of the chosen process. The detector simulation is specific for each experiment, so Monte Carlo event generators provide the final state in terms of stable particles before interactions with the detector material and their four-momenta, together with the cross section of the process. However, the exact calculation of the general process $pp \rightarrow n$ with a final state of n particles is impossible for two reasons: first, the initial protons are a QCD bound state which cannot be described perturbatively, and second, the perturbative expansion of the hard scattering has to be truncated at some fixed order. In a first step, the hard scattering subprocess is separated from the incoming proton via collinear factorisation [43] and introducing the factorisation scale μ_F , reducing the problem to the calculation of the hard scattering of partons, and their origin from the protons. The general hard scattering cross section $\sigma_{pp \rightarrow n}$ of a proton-proton collision producing a final state n can then be expressed as:

$$\begin{aligned}\sigma_{pp \rightarrow n} &= \sum_{a,b} \int_0^1 dx_a dx_b \int f_a^{p_1}(x_a, \mu_F) f_b^{p_2}(x_b, \mu_F) d\hat{\sigma}_{ab \rightarrow n}(\mu_F, \mu_R) \\ &= \sum_{a,b} \int_0^1 dx_a dx_b \int d\Phi_n f_a^{p_1}(x_a, \mu_F) f_b^{p_2}(x_b, \mu_F) \\ &\quad \times \frac{1}{2x_a x_b s} |\mathcal{M}_{ab \rightarrow n}|^2(\Phi_n, \mu_F, \mu_R),\end{aligned}\tag{4.1}$$

where $f_{a,b}^{p_{1,2}}$ are the parton distribution functions (PDFs) parametrising the probability to find a parton of flavour a (b) with momentum fraction x_a (x_b) inside its parent proton p_1 (p_2), when the proton is probed at a factorisation scale μ_F . The partonic cross section $\hat{\sigma}_{ab \rightarrow n}$ describes the probability to create the final state n with the initial partons a, b , given the final state phase space Φ_n , the factorisation scale μ_F and the renormalisation scale μ_R . It is expressed as the absolute square of the matrix element, $\mathcal{M}_{ab \rightarrow n}$, multiplied by the inverse partonic flux $\frac{1}{2x_a x_b s}$, with the square of the centre-of-mass energy s . To summarise, the ingredients of the simulation of collision events are:

- PDFs
- Hard scattering
- Parton shower
- Hadronisation
- Detector simulation.

The calculation of the hard scattering cross section is performed via evaluation of the matrix element. Its form is determined by the Lagrangian of the underlying theory and the Feynman rules (see section 2.2). The parton shower then evolves QED and QCD emissions from incoming and outgoing particles to all orders of perturbation theory down to the hadronisation scale, where QCD becomes non-perturbative

(c.f. section 2.1.1). This is the entry point for the hadronisation, which uses phenomenological models to describe the production of colourless hadrons from the outgoing partons of the parton shower. The last step in the event generation chain is the simulation of the detector response to the generated stable particles.

4.1.1 Parton Distribution Functions

At leading order, the parton distribution function $f_i(x, \mu_F)$ describes the probability to find a parton i with momentum fraction x inside a proton probed at the factorisation scale μ_F . This function cannot be derived from the theory since it depends on the non-perturbative proton physics, but instead has to be tuned and fitted to collision and deep inelastic scattering data. As soon as the parametrisation at some initial scale μ_{F0} is known, however, the DGLAP¹² equations determine the behaviour at all higher scales [44]. At present, a variety of PDF sets is available. Throughout this analysis, the CTEQ6 [45] and CT10 [46] PDF sets provided by the CTEQ collaboration [47] are used. Alternatives like the MRST PDF [48] are also commonly used, and yield comparable results in benchmark scenarios [49].

4.1.2 Hard Scattering

As mentioned above, the cross section $\hat{\sigma}_{ab \rightarrow n}$ of the hard scattering process is calculated by constructing and evaluating the corresponding absolute square of the matrix element, $|\mathcal{M}|^2$, averaged over all spin and colour degrees of freedom, and then integrating over the final state phase space Φ_n . The matrix element depends on both the factorisation scale which separates the perturbative hard scattering from the non-perturbative part absorbed in the PDFs, and the renormalisation scale at which the involved running couplings are evaluated (see section 2.1). It is constructed as the sum over all contributing Feynman diagrams. Since the number of Feynman diagrams increases approximately factorial with the number of outgoing particles, dedicated matrix element generators employing recursion techniques are used for high-multiplicity final states. Examples are the ALPGEN [50] and MADGRAPH [51] multi-leg generators.

Next-to-leading order hard scattering cross sections are formally expressed in terms of the leading order (Born-level) component \mathcal{B} denoted as $\hat{\sigma}_{ab \rightarrow n}$ in Equation 4.1, and the virtual and real-emission corrections, \mathcal{V} and \mathcal{R} , respectively:

$$\hat{\sigma}_{NLO} = \int_n d\tilde{\Phi}_n \left[\mathcal{B}(\tilde{\Phi}_n) + \alpha_S \mathcal{V}(\tilde{\Phi}_n) \right] + \int_{n+1} d\tilde{\Phi}_{n+1} \alpha_S \mathcal{R}(\tilde{\Phi}_{n+1}), \quad (4.2)$$

where $\tilde{\Phi}_n$ and $\tilde{\Phi}_{n+1}$ denote the phase space element for the n -particle and $n + 1$ -particle final state, respectively, including the integration over the partonic momentum fractions x implicitly. In practice, the generators of NLO matrix elements have to overcome additional subtleties, most notably divergencies in both the real and virtual corrections. For additional information about these techniques, see e.g. [52] and [53].

The integration of the phase space is usually complicated, and a combination of sophisticated Monte Carlo integration techniques [54] is employed by the matrix element generators. For example, spikes in the phase space are flattened by variable transformations before integration, and divergencies due to propagators going on-shell are either regularised with mass terms or simply cut out.

4.1.3 Parton Shower

A parton shower algorithm models the evolution of the partons produced at the energy scale of the hard scattering down to the energy scale of hadronisation, where QCD becomes non-perturbative. It compensates approximately for all higher order effects omitted from the fixed order matrix element calculation. The evolution of the parton shower is based on the no-emission probability $\Delta_i(Q^2, q^2)$ of a

¹²Named after their developers Dokshitzer, Gribov, Lipatow, Altarelli and Parisi.

parton i between the starting scale Q^2 and a lower scale q^2 . This no-emission probability, also called the Sudakov form factor, can be derived as [55]:

$$\Delta_i(Q^2, q^2) = \exp\left(-\int_{q^2}^{Q^2} \frac{dk^2}{k^2} \frac{\alpha_S}{2\pi} \int_{Q_0^2/k^2}^{1-Q_0^2/k^2} dz P_{ji}(z)\right), \quad (4.3)$$

where $P_{ji}(z)$ are the splitting kernels, expressing the probability of a splitting of the form $i \rightarrow ij$ to occur producing a parton j with a momentum fraction z . The strong coupling α_S is evaluated for each splitting at a scale proportional to the relative transverse momentum between the incoming and the emitted parton. The lower cutoff scale Q_0 has to be chosen carefully: if it is too low, the coupling α_S becomes of the order of 1 and the shower evolution enters the non-perturbative regime. In practise, the evolution of the shower is performed by drawing a random number $\rho \in [0, 1]$ and solving $\Delta_i(Q^2, q^2) = \rho$ for q^2 using the right side of equation 4.3. If $q^2 > Q_0^2$, a splitting is created at the scale q^2 and the process is reiterated with a new starting scale $Q^2 = q^2$, otherwise the evolution terminates.

The parton shower is separated in final state radiation (FSR) and initial state radiation (ISR). This distinction is rather arbitrary from a physics point of view, and eventual interference effects have to be handled carefully. Nevertheless, the distinction is still necessary because it allows for a forward evolution of final state partons, and a backward evolution for the initial state partons. The former is governed by equation 4.3, while the latter uses a modification reflecting the probability that an initial parton m with momentum fraction x in the hard scattering in fact came from the splitting of a parton l with a higher momentum fraction $x/z, z \in (0, 1)$:

$$\Delta_m(Q^2, q^2, x) = \exp\left(-\int_{q^2}^{Q^2} \frac{dk^2}{k^2} \frac{\alpha_S}{2\pi} \int_{Q_0^2/k^2}^{1-Q_0^2/k^2} dz P_{lm}(z) \frac{x/z_m(x/z, k^2)}{x_l(x, k^2)}\right), \quad (4.4)$$

which contains the ratio of the PDFs for partons m, l as an additional factor modifying the splitting probability.

4.1.3.1 Matching of Matrix Element and Parton Shower An important step is the matching of a higher order matrix element (i.e. with additional hard parton emission) and the parton shower. While the former describe well separated emissions, they lack the capability to model soft emissions correctly. On the other hand, the parton shower is designed to describe soft and collinear emissions down to the hadronisation scale, but cannot model hard emissions well. The matching itself is non-trivial (for a detailed description see e.g. [55]) in order to avoid double-counting or under-counting of phase space regions. In addition, the splitting of partons in the shower evolution transfers momentum to the whole system including the hard scattering, which has to be taken into account. Different methods exist to match a parton shower to tree-level matrix elements, e.g. the MLM matching [56] or the CKKW matching [57], developed to match parton showers to multi-leg tree-level matrix elements. Matching procedures which are correct also for NLO matrix elements are the MC@NLO [58] and the POWHEG [59] method, to mention two examples.

4.1.4 Hadronisation

The term hadronisation in the context of MC event simulation refers to the transition between the partonic final state which is produced by the parton shower algorithm, to the hadronic final state containing only colourless hadrons. For this transition, only empirical models inspired by QCD are available. Two models exist which are in use: the string model and the cluster model. The string model [60] is based on the idea that two coloured objects, e.g. a quark-antiquark pair, are connected via a colour flux tube called a string with a linearly rising potential $V(r) = \kappa r$. When the quark and the antiquark move away from each other, the potential energy in the string increases, until it eventually breaks apart forming an additional quark-antiquark pair. This process continues until the kinetic energy between a quark and the adjacent antiquark is no longer sufficient to form another quark-antiquark pair. The string model is employed by the PYTHIA [61] event generator.

The cluster model is based on the so-called preconfinement property of parton showers [62], which basically states that nearby quarks and gluons from the parton shower already form colourless clusters. The gluons are then forced to decay into additional quark-antiquark pairs of the respective colours. Once the cluster only contains quarks and antiquarks, it “decays” into a set of hadrons allowed by spin, parity, flavour and kinematics at random. This requires some tuning and care must be taken not to bias the quantities of some hadrons at the cost of others. Examples for generators using the cluster model for hadronisation are HERWIG [63] and SHERPA [64].

4.1.5 Detector Simulation

The detector simulation for ATLAS is done utilising GEANT 4 [65], a general purpose framework for simulating particle passages through matter. A full model of the ATLAS detector, including alignment and magnetic field information, is used. The simulation of the detector response to a generated event is performed in several steps. At first, the particles from the event generator are propagated through the detector using GEANT 4, and hits corresponding to energy deposits in the detector systems are produced. The next step is the digitisation, in which the hits are translated to digits if they meet requirements such as a certain energy or voltage threshold in a predefined time window. The requirements depend on the detector subsystem in which the hit was generated. The collection of digits is called raw data object (RDO), which contains all information about the event which the ATLAS detector would have recorded had it occurred in a real particle collision. In addition, a truth record is also formed as part of the RDO, which contains all information of the original particles produced by the event generator. Now, the regular trigger and reconstruction algorithms can be applied to turn the RDO into higher-tier reconstructed particle candidates for further analysis (see section 5).

4.2 Monte Carlo Generators

This section will briefly introduce the most important MC event generators employed in the presented analyses.

4.2.1 POWHEG

The Positive Weight Hardest Emission Generator (POWHEG) [66] is a generic prescription to match NLO matrix elements to any subsequent parton shower evolution. The basic idea is to generate the hardest emission first, with NLO accuracy, and then hand the NLO-correct event to the parton showering algorithm. The hardest emission is hereby generated using a similar approach as in the evolution of a parton shower, using a modified Sudakov form factor (see equation 4.3) and a splitting into real and virtual NLO corrections as in equation 4.2. For details, see e.g. [59]. The only requirement for this procedure to yield correct results is that the subsequent shower algorithm must not generate emissions harder than the POWHEG emission. The POWHEG method has been implemented for a variety of processes (see [67] for a complete list), and is used in conjunction with PYTHIA as parton shower algorithm to generate gluon-fusion and vector-boson fusion Higgs boson signal samples for the $H \rightarrow \mu^+\mu^-$ search. In addition, the $Z/\gamma^* \rightarrow \mu^+\mu^-$ and quark-initiated diboson background samples used in this analysis are generated with POWHEG. For a full list, see appendix B.

4.2.2 MC@NLO

The method of MC@NLO [58] is another recipe to match NLO matrix elements to parton shower algorithms. Starting from equation 4.2 for the NLO cross section, the real emission corrections are modified such that they contain only terms not covered by the parton shower algorithm, effectively subtracting them from the expression. In practice, two sets of events are generated, one with positive weights without any modifications, and one with negative weights correcting the NLO real emissions already covered

by the parton shower algorithm, which in total produce the correct NLO differential distributions of observables. The MC@NLO generator package [68] is used to simulate single top quark and $t\bar{t}$ background samples used in this analysis, see appendix B for a detailed listing.

4.2.3 Pythia

PYTHIA [69] is a multi-purpose Monte Carlo generator providing modules for all stages of MC event simulation, except the detector simulation. It implements several hard scattering processes of the Standard Model and beyond, e.g. weak boson production, top quark production and Higgs boson production. PYTHIA further provides an implementation of a p_T ordered parton shower algorithm as described in section 4.1.3 for both initial and final state showers, and has modules for hadronisation, underlying event and multi-parton interactions. Its main usage for this thesis is as an interfaced parton shower and hadronisation module for hard scattering processes generated with POWHEG.

4.2.4 Alpgen

ALPGEN [50] is a multi-parton matrix element generator, capable of calculating the exact matrix element for weak boson and heavy quark production with up to six additional light partons (quarks, antiquarks and gluons) at leading order. For a specified parton multiplicity, it selects a subprocess contributing to this multiplicity. For example, for $Z + 2$ partons, possible subprocesses are $q\bar{q} \rightarrow Zgg$, $qg \rightarrow Zqg$ and $gq \rightarrow Zq\bar{q}$, among others. The matrix elements of the subprocesses are calculated using a recursive algorithm described in [70]. ALPGEN is used in conjunction with HERWIG + JIMMY [63][71] to simulate the $W \rightarrow l\nu$ background contributions with up to five additional parton emissions, see appendix B.

5 Muon Reconstruction and Identification

The reconstruction and identification of muons plays a crucial role in the course of this analysis. A high reconstruction efficiency as well as excellent resolution is required, thus complementary algorithms utilising different parts of the ATLAS detector are usually combined to achieve optimal results. The reconstruction and identification algorithms for muons in ATLAS can be classified following four different strategies:

- *standalone* muon reconstruction algorithms
- *combined* reconstruction algorithms
- *segment tagging*
- *calorimeter tagging*.

These strategies, their advantages, disadvantages and usage are explained in the following sections. The full muon reconstruction chain combines several of the aforementioned strategies to ensure high precision, efficiency and purity.

During the course of LHC Run I, two algorithm families called STACO¹³ and MUID¹⁴ were available for physics analyses [72]. These algorithm families are also called *Chain 1* and *Chain 2*. Each comes with dedicated algorithms implementing the aforementioned strategies, both with comparable performance [73]. These two families have recently been merged to form the *Unified Muon Identification Chain* [74]. However, since this new chain was still in the validation step at the beginning of this analysis, it was not utilised, and the STACO family is used instead.

5.1 Standalone Muon Reconstruction

The standalone (SA) muon reconstruction begins in the ATLAS muon spectrometer. The fast RPC and TGC chambers (c.f. section 3.2.4.3 and 3.2.4.4) define regions of interest (ROIs) in the muon spectrometer. In these ROIs, the algorithms search for hits in the precision MDT and CSC chambers, depending on the detector region (see section 3.2.4). The spatial information of the hit in a single tube defines a drift circle with a distinct radius. Now drift circles of adjacent tubes with hits are connected with tangents. If the constructed tangents are compatible with hits in additional tubes, they are kept as track segments. This step of the standalone reconstruction is therefore called *segment finding*. The remaining coordinate of the track segment in the non-bending plane is either associated from the RPC or TGC hit, or extracted from the drift time information in the precision chamber.

The next step involves the combination of track segments to form so-called roads. Track segments in a single muon station are matched using the χ^2 of the combined track match as a discriminating variable. Roads of up to three different muon stations are then used to form a track, taking multiple scattering and energy loss between the stations into account. The tracks are then extrapolated back through the calorimeter and inner detector to the point of closest approach to the beamline. During this procedure, the energy loss of the muon candidate in the calorimeter system is taken into account, either by using the measurement of the energy deposit directly, or by parametrisations in case the energy measurement is either inaccurate or unreliable due to calorimeter noise or lack of instrumentation (e.g. if the extrapolated track traverses through support structures).

5.2 Combined Muon Reconstruction

As the name suggests, combined (CB) muon reconstruction algorithms utilise a combination of detector information from both the inner detector (c.f. 3.2.2) and the muon spectrometer to reconstruct muon objects with optimal purity and resolution. The concrete reconstruction strategy differs between the MUID

¹³Statistical Combination

¹⁴Muon Identification

and STACO, and only the latter will be discussed here. The starting point of the algorithm are standalone reconstructed muons, of which the (extrapolated) track parameters at the nominal interaction point are already known. A geometrical matching is performed to search for tracks reconstructed by inner detector tracking algorithms. If one or more inner detector tracks are found in the vicinity of the standalone muon candidate, the matching χ^2 :

$$\chi_{\text{match}}^2 = (\vec{t}_{\text{MS}} - \vec{t}_{\text{ID}})^T (\mathbf{C}_{\text{ID}} + \mathbf{C}_{\text{MS}})^{-1} (\vec{t}_{\text{MS}} - \vec{t}_{\text{ID}}), \quad (5.1)$$

for each of the matches is calculated. Here \vec{t}_{MS} and \vec{t}_{ID} denote the track parameter vectors measured in the muon spectrometer and the inner detector, respectively, and \mathbf{C}_{MS} and \mathbf{C}_{ID} label their covariance matrices. If the matching χ^2 is sufficiently small¹⁵, the combined muon track parameters are calculated as follows:

$$\vec{t} = (\mathbf{C}_{\text{ID}}^{-1} + \mathbf{C}_{\text{MS}}^{-1})^{-1} (\mathbf{C}_{\text{ID}}^{-1} \vec{t}_{\text{ID}} + \mathbf{C}_{\text{MS}}^{-1} \vec{t}_{\text{MS}}). \quad (5.2)$$

5.3 Segment-tagged Muon Reconstruction

The combined muon reconstruction discussed above lacks reconstruction efficiency for both low- p_{T} muons and muons traversing detector regions with less instrumentation, e.g. the barrel-endcap transition region near $|\eta| = 1.05$. To recover efficiency in these cases, segment-tagging (ST) reconstruction algorithms exist. For *Chain 1*, this algorithm is called *MuTag* [31]. Starting from well-reconstructed inner detector tracks which have not yet been used by the STACO combination, MuTag extrapolates these tracks through the calorimeters until reaching the muon spectrometer, and searches for track segments. Again these track segments must not have been utilised during the standalone or combined reconstruction, ensuring a complementary reconstruction to recover the inefficiencies of the standalone and combined algorithms. If such a track segment is found, a χ^2 discriminant between the reconstructed segment parameters and their expectation from the extrapolation is imposed. Once this requirement is met, the inner detector track is tagged and kept as *segment-tagged* (ST) muon.

5.4 Calorimeter-tagged Muon Reconstruction

Calorimeter tagging utilises the fact that muons can be considered minimal-ionising particles in the typical energy range of $O(10^1 - 10^2)$ GeV [18]. The calorimeter tagging acts completely independent from the muon spectrometer, and therefore serves as a complementary measurement to recover efficiency where the muon spectrometer lacks instrumentation. Two algorithms currently exist to identify and reconstruct calorimeter-tagged muons, a cut-based one called CaloMuonTag and a likelihood-based one named CaloMuonLikelihoodTool [31]. They have in common that they both start from well-reconstructed inner detector tracks and extrapolate the track parameters to the calorimeter system. The tracks are required to originate from the primary vertex to reduce fakes by pile-up tracks, and a relative track isolation criterion is imposed:

$$\log_{10} \left(\frac{p_{\text{T}}^{\text{ISO}}}{p_{\text{T}}} \right) < 0.7, \quad (5.3)$$

where $p_{\text{T}}^{\text{ISO}}$ denotes the sum of all tracks' transverse momenta in a geometrical cone around the candidate track and p_{T} refers to the candidate track's transverse momentum itself. After the extrapolation the energy deposits of cells crossed by the extrapolated track and their neighbouring cells in all calorimeter layers are retrieved. CaloMuonLikelihoodTool now constructs a likelihood ratio to distinguish muons from pions, utilising energy ratios reflecting the overall features of the energy deposit. CaloMuonTag on the other hand uses a set of energy threshold and veto cuts depending on η and the respective calorimeter layer to tag a candidate track as a calorimeter muon.

¹⁵Different configurations are possible here, the default mode also used in this analysis requires $\chi^2 \leq 30$ [72]

5.5 Muon Reconstruction Performance

The muon reconstruction algorithms undergo continuous performance evaluation to ensure high-quality reconstructed muons for all kinds of physics analyses. Before the actual data taking at the LHC started, the performance of the algorithms was estimated on MC simulated datasets [31]. Since then both cosmic and collision data were used to measure reconstruction efficiencies, momentum scale and resolution, and moreover provide correction factors for these quantities in cases where their MC simulation estimates differ from measurements in real data. The first measurements of muon reconstruction and identification efficiencies performed on real collision data have been carried out on proton-proton collision data collected by the ATLAS detector at a centre-of-mass energy of $\sqrt{s} = 7$ TeV in 2009 and 2010 [75, 76]. The results of the muon reconstruction performance evaluation presented in this section are based on an integrated luminosity of $\mathcal{L}_{int} = 20.4 \text{ fb}^{-1}$ of collision data at a centre-of-mass energy of $\sqrt{s} = 8$ TeV recorded by the ATLAS detector during the 2012 data taking period.

5.5.1 Reconstruction Efficiency

The reconstruction efficiency was determined employing a *tag and probe* method utilising the decay of the Z -boson to a muon pair. Events containing this decay signature are selected by requiring a pair of oppositely charged isolated muons¹⁶. One of these muons is required to have triggered the event readout, and to be a CB muon. An invariant mass requirement is imposed to the tag-and-probe pair of:

$$|m_{\mu\mu} - M_Z| < 10 \text{ GeV}.$$

The probe muon candidate is required to be either a ST, SA or CaloTag muon, depending on the reconstruction algorithm whose efficiency is measured. Details can be found in [73]. The efficiency for each algorithm type T (with T being either CB or ST algorithms) is then defined as:

$$\epsilon(T) = \epsilon(T|ID) \cdot \epsilon(ID). \quad (5.4)$$

Here $\epsilon(T|ID)$ denotes the muon spectrometer reconstruction and matching efficiency for a muon of type T , measured with CaloTag probes, and $\epsilon(ID)$ is the fraction of muon spectrometer probe candidates associated to an inner detector track.

The reconstruction efficiency measured in collision data and using MC simulated events are shown in figure 5.1. Differences between the measured efficiencies in data and MC are parametrised in a *scale factor* (SF) defined as:

$$SF = \frac{\epsilon^{Data}}{\epsilon^{MC}}. \quad (5.5)$$

The scale factor is then used in physics analyses to allow for a precise comparison between measured quantities and their expectation from MC simulated samples.

5.5.2 Momentum Scale and Resolution

Since the detector resolution is finite, the momentum determined by the reconstruction algorithms has an intrinsic uncertainty. This relative momentum resolution is measured from the track fit parameters during the reconstruction, and can be parametrised as:

$$\frac{\sigma(p_T)}{p_T} = a + b \cdot p_T, \quad (5.6)$$

where a describes the multiple scattering contribution and b denotes the intrinsic detector resolution and residual misalignment effects [77]. Differences between the resolution measurement in data and the estimation from MC simulation are parametrised in Δa and Δb . Additional differences between

¹⁶For the reconstruction efficiency studies, a relative track isolation criterion was used, with $Pt_{cone40}/p_T^\mu < 0.1$, see section

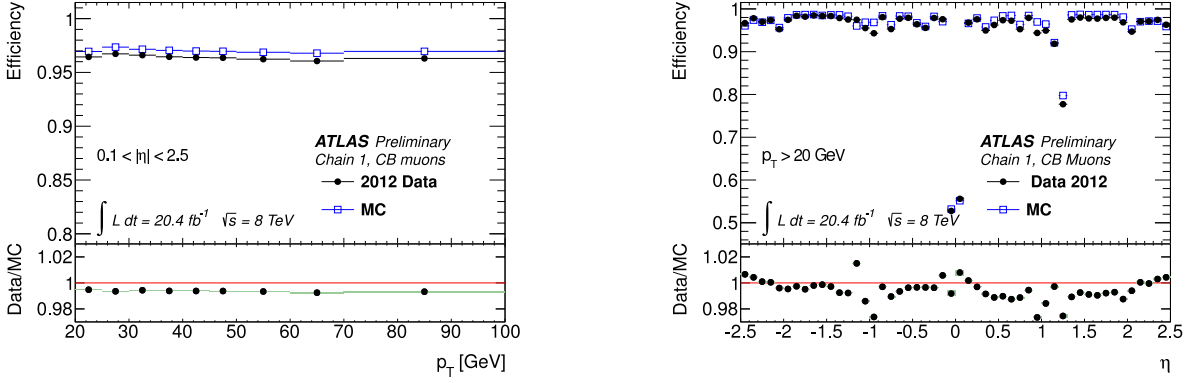


Figure 5.1: Reconstruction efficiency for STACO combined muons as a function of p_T (left) and η (right). The measurement from collision data is marked with black bullets, while the MC simulation is depicted with blue boxes. The bottom half of the plots show the ratio between the measurement in data and the prediction from MC. Taken from [73].

the measured muon momentum in collision data and its estimation from MC simulated events can be absorbed in the momentum scale s , leading to:

$$p_T^{Cor,det} = p_T^{MC,det} \cdot s^{det}(\eta) \left(1 + \Delta a^{det}(\eta) G_1(0, 1) + \Delta b^{det} G_2(0, 1) p_T^{MC,det} \right) \text{ with } det = MS, ID. \quad (5.7)$$

Here $G_1(0, 1)$ and $G_2(0, 1)$ are two random numbers distributed according to a standard normal Gaussian probability density function with a mean of 0 and a width of 1. The correction factors $s^{det}(\eta)$, $\Delta a^{det}(\eta)$ and $\Delta b^{det}(\eta)$ are derived via a template fitting technique of the invariant $m_{\mu\mu}$ distribution in MC simulation to the data spectrum in 16 η bins. The result of the correction procedure can be seen in Figure 5.2, and the η -dependent correction factors s , Δa and Δb are provided by the ATLAS Muon Combined Performance (MCP) group [73, 78].

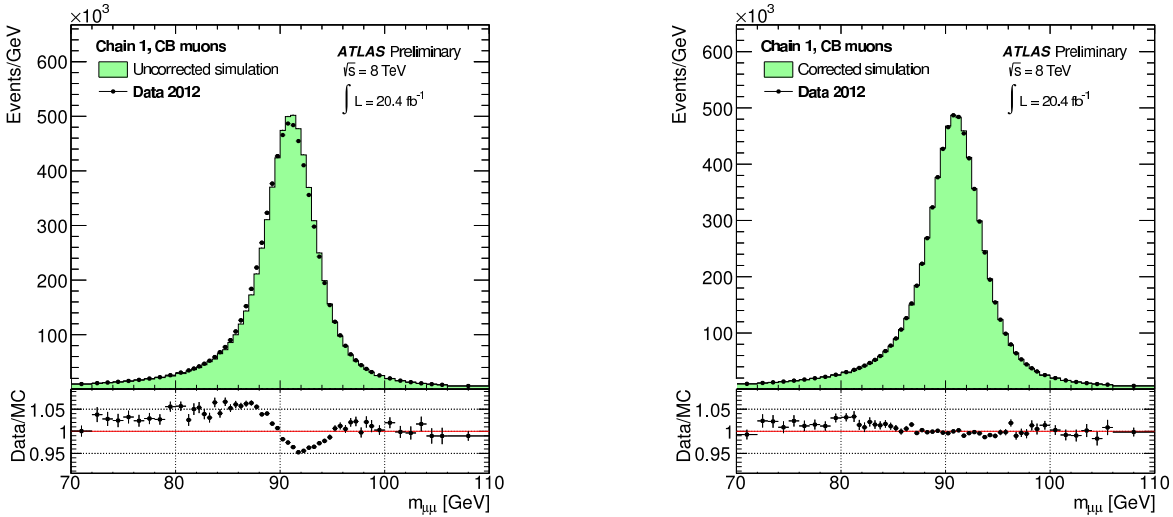


Figure 5.2: Dimuon invariant mass for STACO combined muons with $p_T > 25$ GeV. The left plot shows the distributions of 2012 data and simulated events before the correction, and the right plot shows the distributions with the best fit values of the correction parameters derived with the full 2012 dataset. The residual η dependence of the mass resolution can be observed both in data and simulated events. Taken from [73].

6 Event Selection

The selection of events is performed in a way to keep as many signal events as possible while reducing the background to a manageable amount. As stated before, the main caveat for this analysis is the fact that the Standard Model $Z/\gamma^* \rightarrow \mu\mu$ process has an indistinguishable final state. Thus, the main goal for the event selection is to reduce other backgrounds as far as possible. This is achieved primarily by a trigger requirement and a baseline event selection, which will be discussed below. After that, the remaining events are categorised using event kinematic variables. This is introduced in section 6.3. The goal of the categorisation is to increase the sensitivity of the analysis.

6.1 Trigger Selection

The presented analysis utilises unprescaled single muon triggers with the lowest transverse momentum threshold in order to select a data sample containing at least one muon. The triggers used to select the 2011 and 2012 datasets are listed in Table 6.1. For a detailed description of the muon trigger, see section 3.2.6.1. It is required for the event to pass either of the listed triggers in the respective data period.

year	trigger	comment
2011	EF_mu18_MG	inside-out, seeded by L1_MU10
	EF_mu18_MG_medium	inside-out, seeded by L1_MU11
2012	EF_mu24i_tight	with isolation, seeded by L1_MU15
	EF_mu36_tight	seeded by L1_MU15
	EF_mu18_tight_mu8_EFFS	dimuon trigger

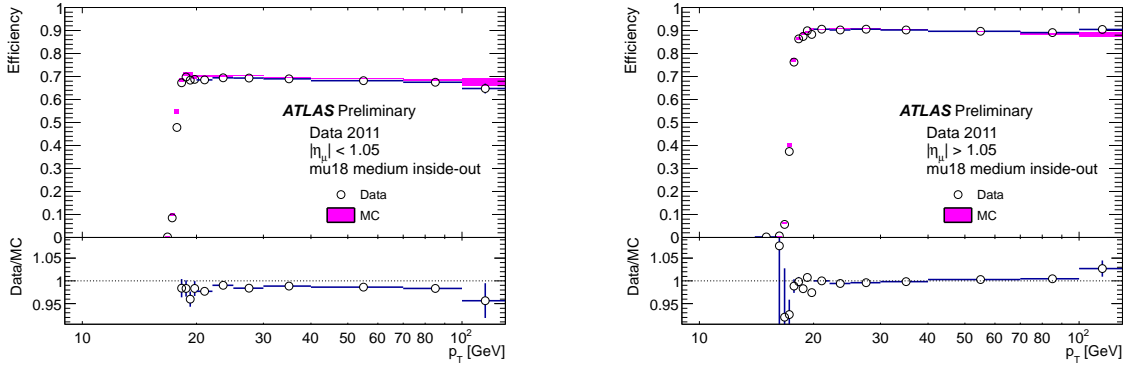
Table 6.1: Triggers used to select the datasets from 2011 and 2012 data taking periods.

In addition to the single muon triggers in 2012, a dimuon trigger is also utilised. Due to the increased instantaneous luminosity in 2012, the trigger rates for the lower threshold EF_mu24i_tight trigger became too high, such that the next higher EF_mu36_tight had to be used. This creates tensions with the later stage offline analysis selection (c.f. section 6.2). To avoid any bias in the event selection, the dimuon trigger, which has a lower momentum threshold, was therefore used as well.

6.1.1 Trigger Efficiencies

The efficiency of the triggers is an important figure for all physics analyses. A high acceptance efficiency is preferred to keep as many events as possible and to not create any selection bias. The trigger efficiency is repeatedly measured by the ATLAS trigger working groups using a tag-and-probe method. Hereby, $Z \rightarrow \mu\mu$ events are selected in data, where one of the muons is used to select the event (the tag muon), and the other one is used to measure the trigger efficiency (the probe muon). Details of the method can be found in [38]. The efficiency of the EF_mu18_MG_medium trigger as measured in 2011 collision data is shown in Figure 6.1. It can be observed that once the trigger plateau is reached, the efficiency of the trigger is flat with respect to the reconstructed muon's transverse momentum, with an average plateau efficiency of 69 (90)% in the barrel (endcap) region. The relatively low trigger efficiency in the barrel part of the detector is mainly due to the limited geometric coverage of the L1 muon trigger system of only 80% [38].

The higher instantaneous luminosity and centre-of-mass energy during 2012 resulted in tighter muon trigger requirements, otherwise the trigger rate would have been too high. The trigger efficiency of the two single muon triggers used for the 2012 data taking is therefore lower. Nevertheless, a high trigger efficiency is maintained by requiring a logical OR between the two triggers. Thus, the trigger efficiency was kept at 70 (84)% average plateau efficiency for the barrel (endcap) during 2012 [79]. The efficiency

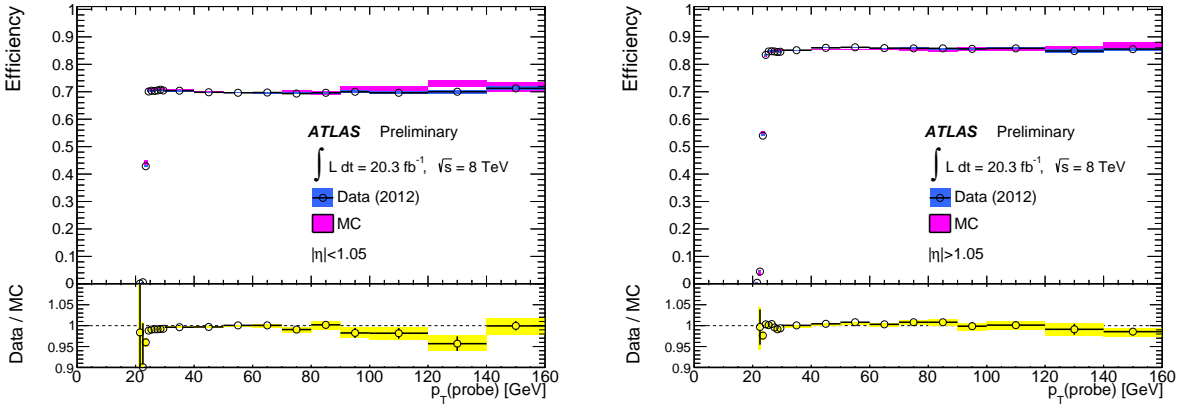


(a) 2011 EF muon trigger efficiency versus p_T of the reconstructed probe muon in the barrel part of the detector.

(b) 2011 EF muon trigger efficiency versus p_T of the reconstructed probe muon in the endcap part of the detector.

Figure 6.1: Single muon trigger efficiencies versus p_T of the reconstructed muon as measured in 2011 data, compared to MC simulation [38].

of the OR between the two applied triggers with respect to the reconstructed muon p_T is shown in Figure 6.2.



(a) 2012 muon trigger efficiency versus p_T of the reconstructed probe muon in the barrel part of the detector. The logical OR combination of the two triggers EF_mu24i_tight and EF_mu36_tight is shown.

(b) 2012 muon trigger efficiency versus p_T of the reconstructed probe muon in the endcap part of the detector. The logical OR combination of the two triggers EF_mu24i_tight and EF_mu36_tight is shown.

Figure 6.2: Combined single muon trigger efficiencies versus p_T of the reconstructed muon as measured in 2012 data, compared to MC simulation [79].

6.1.2 Trigger Scale Factors

The trigger efficiencies measured in data and estimated from Monte Carlo simulation do not agree perfectly, as can be seen from the Figures 6.1 and 6.2. In order to correct this mismodeling, scale factors have been introduced, defined as follows:

$$SF = \frac{1 - \prod_{n=1}^N (1 - \epsilon_{\text{Data}, n})}{1 - \prod_{n=1}^N (1 - \epsilon_{\text{MC}, n})}. \quad (6.1)$$

Here, N denotes the number of reconstructed offline objects satisfying the analysis-specific selection criteria, and $\epsilon_{\text{Data}, n}$ ($\epsilon_{\text{MC}, n}$) refer to the trigger efficiencies for these offline objects obtained in data

(MC), respectively. In equation 6.1, it is assumed that at least one offline reconstructed muon exists in an event, which has a corresponding trigger object associated within a geometrical cone of $\Delta R < 0.15$. The trigger scale factors are available binned in p_T , η and ϕ via a dedicated analysis tool provided by the ATLAS trigger group [80].

6.2 Baseline Selection

In this section, the basic object and event selection cuts are presented, as applied in both the 2012 standalone analysis and the combined analysis of the 2011 and 2012 dataset. Corrections which are necessary when selecting Monte Carlo simulated events are also described.

6.2.1 Physics Object Definitions

6.2.1.1 Muons The selection of muons for the presented analyses starts with the STACO muon collection. A muon is required to fulfil the *tight* muon identification criteria as defined by the Muon Combined Performance group [78], meaning it is a combined muon (c.f. section 5.2). Further, quality requirements on the inner detector track associated to the combined muon need to be fulfilled to ensure a good quality measurement of the track parameters. These quality criteria include:

- at least one hit in the B-layer
- at least one hit in the pixel detector
- at least 5 SCT hits
- less than three pixel and SCT holes
- $n_{TRT}^{outliers} < 0.9 \cdot (n_{TRT}^{outliers} + n_{TRT}^{hits})$.

Here, $n_{TRT}^{outliers}$ and n_{TRT}^{hits} refer to the number of outliers and hits in the TRT subdetector. The last criterion is only applied if the muon lies within the TRT acceptance ($0.1 < |\eta| < 1.9$). Next, the muon candidate has to meet isolation criteria in order to reduce the fraction of non-prompt muons from hadron decays in jets. Both track-based and calorimeter-based isolation criteria are applied. As a track-based isolation variable, the sum of the transverse momenta of inner detector tracks with $p_T > 1$ GeV within a geometrical cone around the muon candidate is used. Hereby, the muon track itself is not counted. The cone size in ΔR defines the name of the criterion: *PtCone30* is the p_T sum of tracks within a cone of $\Delta R < 0.3$, and *PtCone40* refers to a cone size of $\Delta R < 0.4$. The calorimeter-based isolation criteria is defined in a similar way, by summing up energy deposits in calorimeter cells within a geometrical cone around the muon track, removing the cells directly crossed by the muon candidate itself. Further, the calorimeter isolation energy receives a pile-up dependent correction based on the number of reconstructed pile-up vertices [81], and is thus referred to as *EtConeCor30*. The isolation variables further depend on the transverse momentum of the muon candidate, so relative isolation with respect to the candidate p_T is used. Table 6.2 gives an overview on the isolation criteria applied to the muon candidates. In addition, cuts are applied on the reduced longitudinal impact parameter, $z_0 \sin \theta$, and transverse impact parameter significance, $d_0/\sigma(d_0)$, to reject muon candidates from b-hadron decays and secondary vertices:

- $d_0/\sigma(d_0) < 3.0$
- $|z_0 \sin \theta| < 1.0 \text{ mm}$.

For Monte Carlo simulated samples, corrections are necessary to account for differences between quantities measured in data and their estimation from MC. These corrections include the muon momentum scale, muon momentum resolution and muon reconstruction efficiency. They were derived by comparing the simulated muon momenta and resolutions with those from collision data, obtained by a tag-and-probe analysis utilising the Z-boson resonance [82]. Official tools provided by the MCP group are used for efficiency scale factors and muon momentum corrections [83], and systematic uncertainties of these corrections are taken into account (see section 8.1)

Cut	Value
Calorimeter Isolation (2012)	EtConeCor30/ $p_T < 0.12$ for $15 \text{ GeV} < p_T < 20 \text{ GeV}$ EtConeCor30/ $p_T < 0.18$ for $20 \text{ GeV} < p_T < 25 \text{ GeV}$ EtConeCor30/ $p_T < 0.30$ for $p_T > 25 \text{ GeV}$
Calorimeter Isolation (2011)	EtConeCor30/ $p_T < \min(0.0125p_T - 0.14, 0.20)$
Track Isolation (2012)	PtCone40/ $p_T < 0.06$ for $15 \text{ GeV} < p_T < 20 \text{ GeV}$ PtCone30/ $p_T < 0.08$ for $15 \text{ GeV} < p_T < 20 \text{ GeV}$ PtCone30/ $p_T < 0.12$ for $p_T > 20 \text{ GeV}$
Track Isolation (2011)	PtCone30/ $p_T < \min(0.011p_T - 0.12, 0.15)$

Table 6.2: Muon candidate isolation criteria as applied in the 2012 standalone and the 2011-2012 combined analysis.

6.2.1.2 Jets Jets used in this analysis are reconstructed from topological clusters exploiting the anti- k_T clustering algorithm with a distance parameter of $D = 0.4$ [84]. Jets from pile-up vertices are suppressed by applying a jet vertex fraction cut of $JVF > 0.5$ for all jets within $|\eta| < 2.4$. The jet vertex fraction is defined as:

$$JVF = \frac{\sum_k^{\text{tracks}} p_T^k |vtx_{\text{primary}}|}{\sum_l^{\text{vertices}} \sum_m^{\text{tracks}} p_T^m |vtx_l|}, \quad (6.2)$$

where $p_T^k |vtx_{\text{primary}}|$ are the transverse momenta of tracks associated to the jet coming from the primary vertex, and $p_T^m |vtx_l|$ are the transverse momenta of associated tracks coming from vertex l . Jets originating from the primary vertex have a substantial fraction of their associated tracks compatible with the primary vertex, and therefore have a larger JVF than jets from pile-up interactions.

Reconstructed jets in collision data further undergo a jet cleaning procedure to reject jets reconstructed in a detector area which is known to have non-optimal readout conditions. This jet cleaning is applied following the official recommendations by the ATLAS Jet/ETMiss group [85]. On the simulation side, corrections are necessary similar to the muon case. These corrections include the jet energy scale and resolution [86]. Official tools by the Jet/ETMiss group are used to apply these corrections [87].

Aside from its kinematic 4-vector properties, another important figure for jets in the combined 2011-2012 data analysis is the probability that it originated from hadronisation of a b -quark. Assigning this probability is called b -tagging. In the presented analysis, a multivariate b -tagging algorithm called MV1 [88] is used, which combines jet kinematics, secondary vertex information and track impact parameters in an artificial neural network. A cut is placed on the neural network output w of $w > 0.39$, which corresponds to a b -tagging efficiency of 80% [89].

6.2.1.3 Missing Transverse Energy The missing transverse energy E_T^{miss} does not directly correspond to a physical object, but rather gives a hint that a particle left the detector volume undetected, e.g. a neutrino [18]. Based on the assumption that the transverse momentum and transverse energy in the initial state of the collision is zero, energy-momentum conservation dictates that the sum of all transverse momenta and energies after the collision adds up to zero aswell. That way, the missing transverse energy can be defined simply as the negative sum of all measured transverse momenta and energies:

$$\vec{E}_T^{\text{miss}} = - \sum \vec{E}_T. \quad (6.3)$$

In reality, the situation is much more complicated due to regions with less detector instrumentation, dead material, and different energy calibrations for different physics objects. As a starting point, the missing

transverse energy is calculated from calorimeter energy deposits, with corrections from muon spectrometer information. The calorimeter cells entering the E_T^{miss} calculation are calibrated to the reconstructed object they are associated to, e.g. electrons, photons or τ leptons. Calorimeter cells without an associated reconstructed object are calibrated at the electromagnetic scale per default. In addition, the missing transverse energy receives a pile-up suppression term, such that the x and y components of E_T^{miss} can be written as follows [90]:

$$E_{x(y)}^{\text{miss}} = E_{x(y)}^{\text{miss},e} + E_{x(y)}^{\text{miss},\gamma} + E_{x(y)}^{\text{miss},\tau} + E_{x(y)}^{\text{miss},\text{jets},JVF} + E_{x(y)}^{\text{miss},\text{CellOut_Eflow_STVF}} + E_{x(y)}^{\text{miss},\mu}, \quad (6.4)$$

where $E_{x(y)}^{\text{miss},\text{jets},JVF}$ is the missing transverse energy term for jets corrected by their respective jet vertex fraction JVF (c.f. section 6.2.1.2) and $E_{x(y)}^{\text{miss},\text{CellOut_Eflow_STVF}}$ is the pile-up corrected E_T^{miss} term for calorimeter cells not associated to a reconstructed object ¹⁷.

6.2.2 Event Preselection

The event preselection ensures a high quality of selected events with all relevant detector components performing within their nominal parameters. As a first step, a *good runs list* (GRL) is applied. This list contains detector performance and basic data quality information for each luminosity block. ¹⁸ The application of the GRL is therefore a way to ensure that no subdetector was malfunctioning, and that the data was correctly recorded. Table 6.3 lists the GRLs used for the 2011 and 2012 datataking periods. Next, events are rejected which are known to suffer from electronic noise bursts in the calorimeter. This

Year	GRL name
2011	data11.7TeV.periodAllYear_DetStatus-v36-pro10-02_CoolRunQuery-00-04-08_All_Good.xml
2012	data12.8TeV.periodAllYear_DetStatus-v61-pro14-02_DQDefects-00-01-00_PHYS_StandardGRL_All_Good_overlap.xml

Table 6.3: Good runs lists employed for the 2011 and 2012 datataking periods in the presented analyses.

is checked by evaluating a dedicated bit pattern flag in each event, provided by the Data Preparation Group [91]. Furthermore, the event has to have at least one reconstructed primary vertex with at least three associated tracks, which is compatible with the nominal beam spot position.

6.2.3 Candidate Event Selection

After the preselection stage, baseline candidate events are defined by the following selection criteria:

- exactly two reconstructed muons with opposite charge
- transverse momentum of the leading muon $p_T^{\mu 1} > 25$ GeV
- transverse momentum of the subleading muon $p_T^{\mu 2} > 15$ GeV
- geometrical matching of the leading muon and the trigger object within $\Delta R < 0.15$.

The leading and subleading muon p_T and η distributions after the candidate event selection are shown in figure 6.3 and 6.4 for the 2012 dataset and in figure 6.5 and 6.6 for 2011 data.

¹⁷STVF stands for *Soft Term Vertex Fraction*.

¹⁸A luminosity block is a short period of datataking, lasting ≈ 2 min.

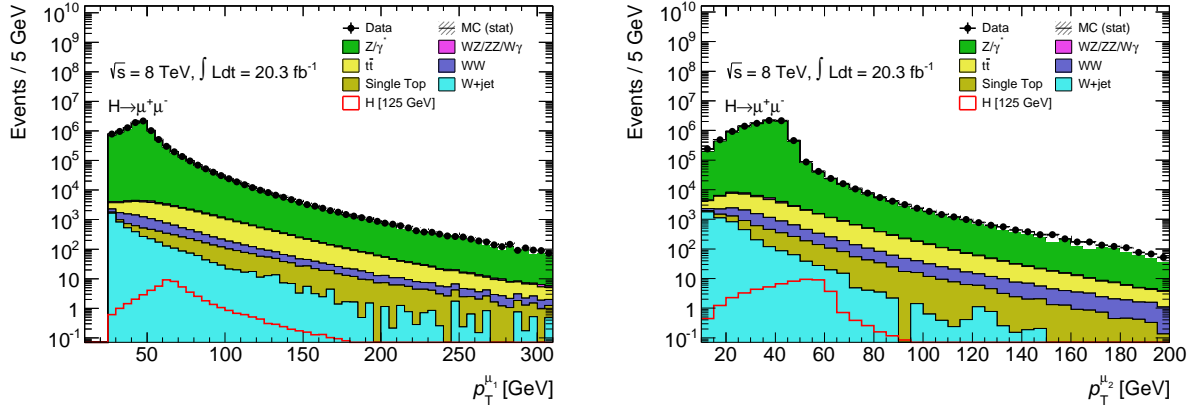


Figure 6.3: Leading (left) and subleading (right) muon transverse momentum distributions after the candidate event selection. The black dots indicate the 2012 measured data points, and the stacked color-coded histograms denote the expected background contributions estimated from MC simulation. The red line represents the expected contribution of a Higgs boson with a mass of 125 GeV.

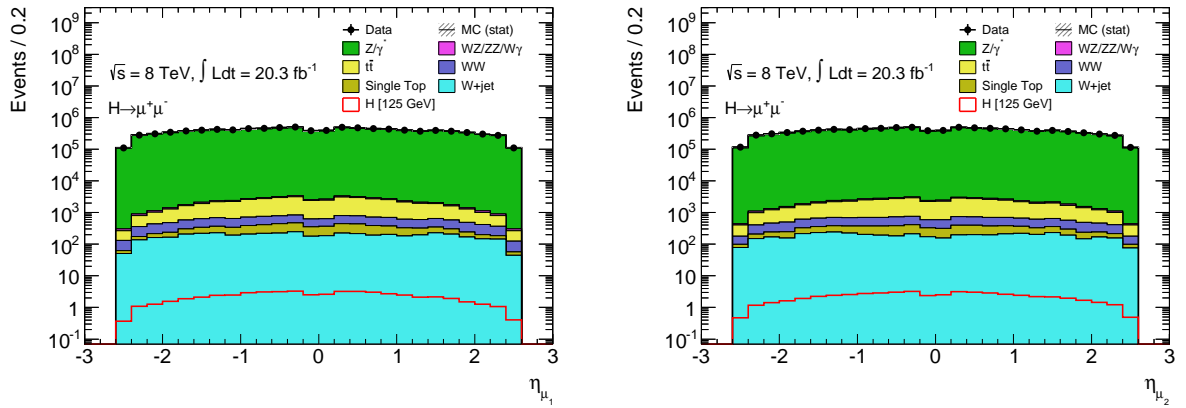


Figure 6.4: Leading (left) and subleading (right) muon pseudorapidity distributions after the candidate event selection. The black dots indicate the 2012 measured data points, and the stacked color-coded histograms denote the expected background contributions estimated from MC simulation. The red line represents the expected contribution of a Higgs boson with a mass of 125 GeV.

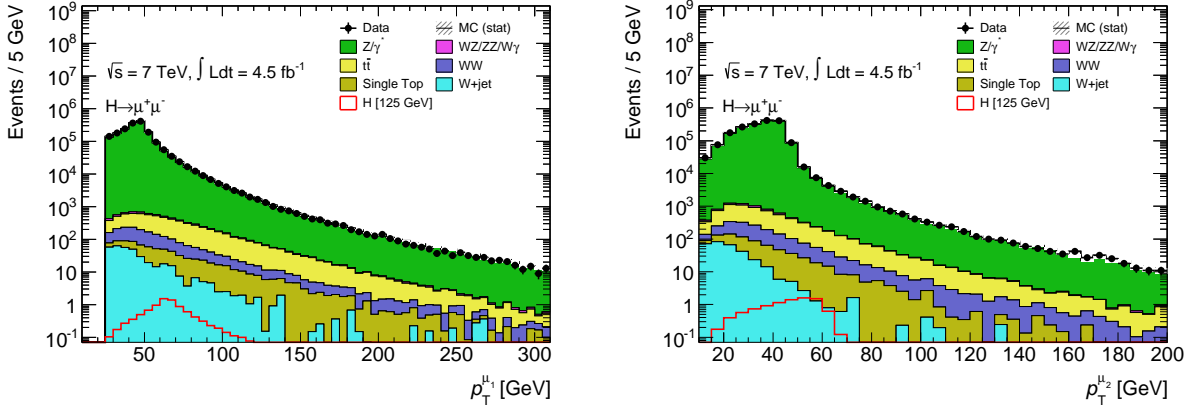


Figure 6.5: Leading (left) and subleading (right) muon transverse momentum distributions after the candidate event selection. The black dots indicate the 2011 measured data points, and the stacked color-coded histograms denote the expected background contributions estimated from MC simulation. The red line represents the expected contribution of a Higgs boson with a mass of 125 GeV.

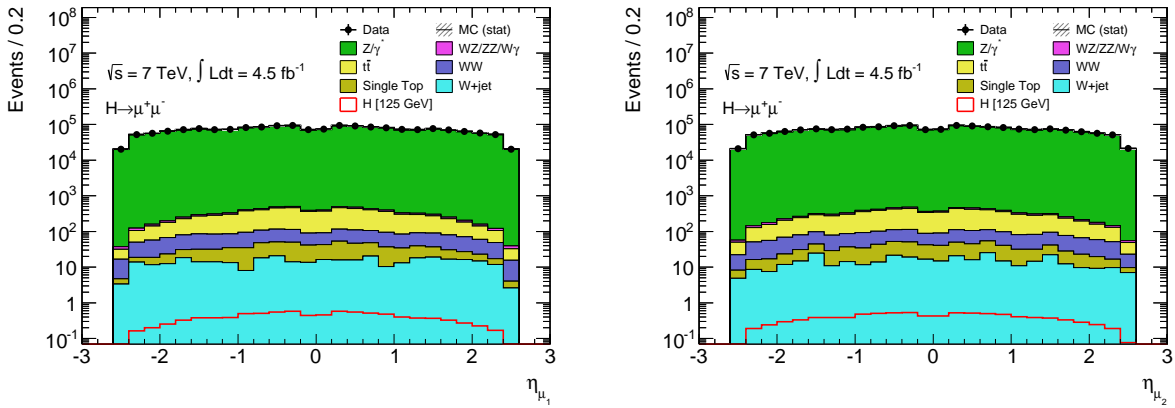


Figure 6.6: Leading (left) and subleading (right) muon pseudorapidity distributions after the candidate event selection. The black dots indicate the 2011 measured data points, and the stacked color-coded histograms denote the expected background contributions estimated from MC simulation. The red line represents the expected contribution of a Higgs boson with a mass of 125 GeV.

For a further categorisation, the dimuon transverse momentum, $p_T^{\mu\mu}$, is used (c.f. section 6.3). Its distribution after the baseline event selection is shown in figure 6.7. The invariant mass of the dimuon system is the target distribution for the presented analyses. Figure 6.8 shows the $m_{\mu\mu}$ distribution after the common baseline selection. The final baseline selection cut defines the dimuon invariant mass window, in which the search for a signal is later performed. This window is defined as $105 \text{ GeV} \leq m_{\mu\mu} \leq 160 \text{ GeV}$.

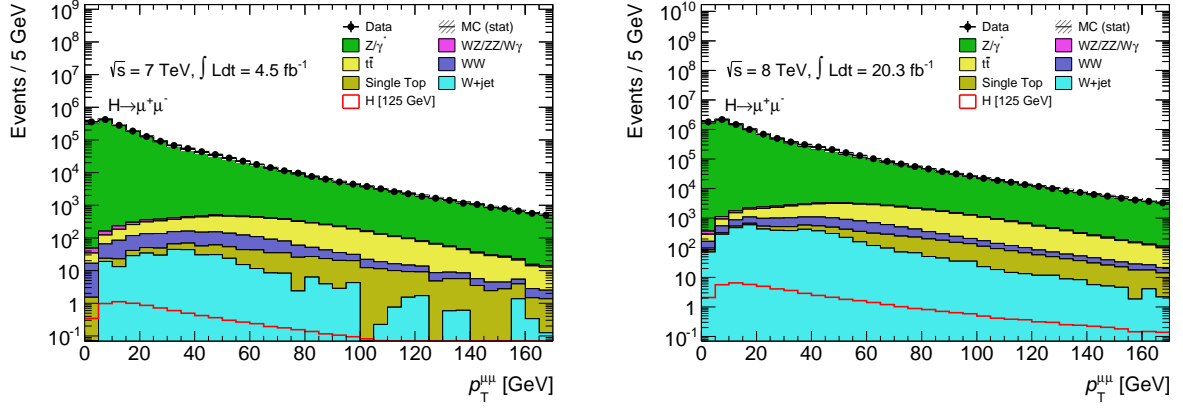


Figure 6.7: Dimuon transverse momentum distributions after baseline selection cuts for 2011 (left) and 2012 (right). The measured data is shown as black points, and expected contributions from simulated background processes is shown as stacked color-coded histograms. The contribution of a 125 GeV Higgs boson signal is shown as a red line.

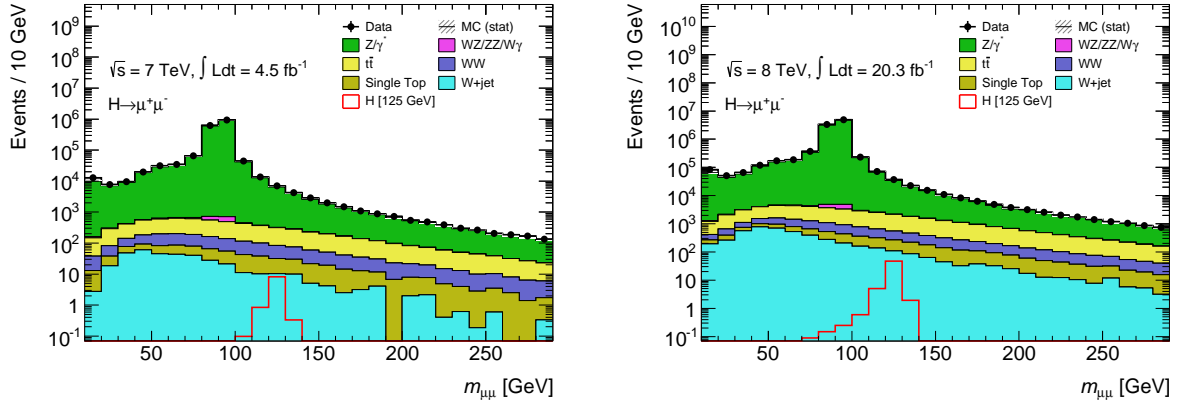


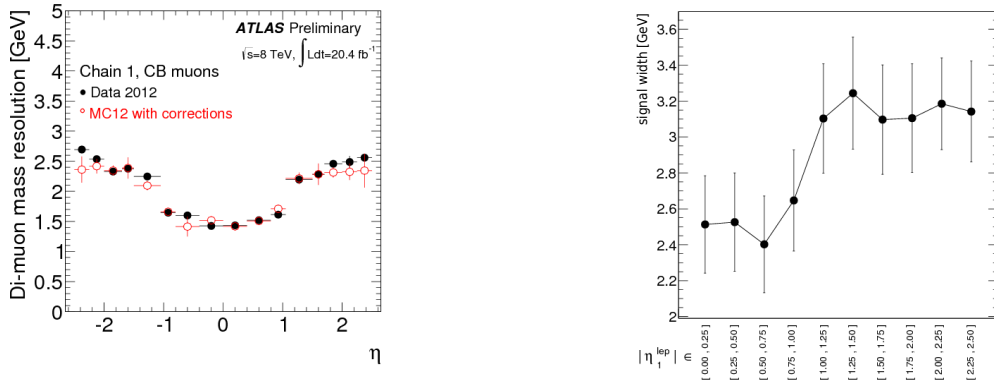
Figure 6.8: Dimuon invariant mass distributions after baseline selection cuts for 2011 (left) and 2012 (right). The measured data is shown as black points, and expected contributions from simulated background processes is shown as stacked color-coded histograms. The contribution of a 125 GeV Higgs boson signal is shown as a red line.

6.3 Analysis Categories

The sensitivity of the presented analyses is improved by exploiting both the detector performance parameters as well as the expected signal and background compositions in the event kinematics phase-space. While the former has been followed in both the 2012 standalone and the 2011+2012 combined analysis, the latter optimisation was only partly used in the 2012 analysis, and has received a major overhaul for the combination. The categorisation rooted in detector performance utilises different dimuon invariant mass resolutions in the barrel and endcap parts of the detector, whereas the categorisation based on signal and background kinematics uses the transverse momentum of the dimuon system, $p_T^{\mu\mu}$.

6.3.1 Resolution Categorisation

The Higgs boson in the considered search range has a very narrow decay width which is two to three magnitudes smaller than the detector resolution, as described in section 2.2.2. Thus, the observed width of the resonance is completely dominated by the resolution. In the barrel part of the detector, the invariant mass resolution is about 25% better than in the endcap, as studies using the Z -boson resonance decaying to a muon-antimuon-pair have shown [73]. This is also observed using simulated decays of a Higgs boson with a mass of 125 GeV. Figure 6.9 shows the invariant dimuon mass resolution for the Z resonance and the simulated Higgs boson, respectively. Based on these studies, two resolution categories are chosen:



(a) Invariant dimuon mass resolution of the Z -boson resonance measured in 2012 collision data (black) and estimated from corrected MC simulation (red) [73]

(b) Width of a gaussian fit to the invariant dimuon mass in a simulated $H \rightarrow \mu\mu$ sample versus η interval of the muons. The width is used as a measure for the detector resolution.

Figure 6.9: Dimuon invariant mass resolutions as a function of pseudorapidity. The transition from the barrel to the endcap spectrometer can be observed as a increase in the resolution at $|\eta| \approx 1.0$.

- central: $|\eta_{\mu,1}| < 1.0, |\eta_{\mu,2}| < 1.0$
- non-central: at least one $|\eta_{\mu}| > 1.0$.

This categorisation is used in the 2012 standalone analysis and throughout most of the reoptimised combined 2011+2012 analysis, except for the dedicated vector boson fusion (VBF) category (see section 6.3.3).

6.3.2 8 TeV Standalone Analysis Categories

From figure 6.7 it can be seen that the $Z/\gamma^* \rightarrow \mu\mu$ background dominates at low dimuon transverse momenta, whereas the expected signal tends to have higher dimuon p_T . Therefore, after an optimisation using the signal over square-root of background (S/\sqrt{B}) metric with a simulated 125 GeV Higgs signal, a cut value of $p_T^{\mu\mu} > 15$ GeV is placed [92]. The complementary region with $p_T^{\mu\mu} \leq 15$ GeV is used as a data control region. Table 6.4 summarises the standalone 2012 analysis selection in a cutflow.

	Signal [125 GeV]	WW	WZ/ZZ/W γ	$t\bar{t}$	Single Top	Z+jets	W+jets	Total Bkg.	Observed	Data/MC
MC weights	57.02 ± 0.26	6710 ± 20	4605 ± 15	32127 ± 64	3246 ± 24	8931800 ± 5500	14760 ± 170	8993300 ± 5500	9205567	1.02 ± 0.00
$p_T^{\mu,1} > 25$ GeV	56.84 ± 0.26	4281 ± 16	3275 ± 10	20963 ± 51	2167 ± 19	8720800 ± 5500	10890 ± 160	8762300 ± 5500	8593165	0.98 ± 0.00
$p_T^{\mu,2} > 25$ GeV	56.43 ± 0.26	4207 ± 16	3194 ± 10	20504 ± 50	2113 ± 19	8639600 ± 5400	10890 ± 160	8680500 ± 5400	8514523	0.98 ± 0.00
$p_T^{\mu\mu} > 15$ GeV	44.05 ± 0.22	3733 ± 15	2734 ± 10	19684 ± 49	2033 ± 19	3608100 ± 3500	5320 ± 120	3641600 ± 3500	3505195	0.96 ± 0.00
$105 < m_{\mu\mu} < 160$ GeV	43.53 ± 0.22	1254 ± 9	156.3 ± 2.8	6970 ± 29	723 ± 11	100840 ± 490	350 ± 21	110300 ± 490	106900	0.97 ± 0.01
central region	12.74 ± 0.12	227.5 ± 3.7	29.13 ± 1.03	1978 ± 15	208.0 ± 5.9	22110 ± 230	57.3 ± 9.4	24610 ± 230	23458	0.95 ± 0.01
non-central region	30.79 ± 0.19	1026.4 ± 8.0	127.1 ± 2.6	4992 ± 25	514.7 ± 9.5	78730 ± 430	293 ± 19	85680 ± 430	83442	0.97 ± 0.01

Table 6.4: Expected number of signal and background events after each selection step of the 2012 standalone analysis. The observed number of events in 2012 8 TeV collision data is given in the second last column, and the ratio between data and Monte Carlo expectation is shown in the last column. [92]

6.3.3 7 + 8 TeV Combined Analysis Categories

For the combined 2011 and 2012 search, various ways were investigated [93] how to improve the sensitivity of the analysis with respect to the 8 TeV standalone analysis. Inspired by other Higgs searches ([94], [95]), the definition of a vector boson fusion (VBF) production enriched category is carried out. The VBF selection cuts include:

1. at least 2 reconstructed jets
2. invariant jet mass $m_{jj} > 500$ GeV
3. forward jets: $|\Delta\eta_{jj}| > 3.0$
4. $\eta_{j1} \cdot \eta_{j2} < 0$.

Further, as can be seen from Figure 6.7 and Table 6.4, a small portion of the signal is lost due to the cut on the dimuon transverse momentum. Therefore, this cut is dropped in the combined search. Before the categorisation is done, an additional requirement on the missing transverse energy (c.f. section 6.2.1.3) of $E_T^{\text{miss}} < 80$ GeV is applied, to suppress contributions from top-quark related backgrounds. This is illustrated by Figure 6.10, which shows the E_T^{miss} distribution before applying the additional requirement. In addition it was shown that having categories in the dimuon transverse momentum, $p_T^{\mu\mu}$, further

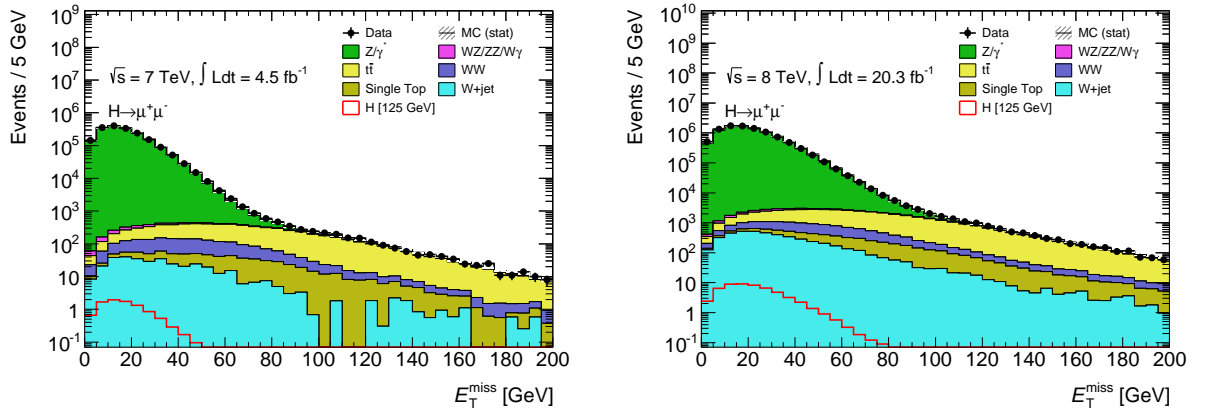


Figure 6.10: E_T^{miss} distributions after baseline selection cuts for 2011 (left) and 2012 (right). The measured data is shown as black points, and expected contributions from simulated background processes is shown as stacked color-coded histograms. The contributions of a 125 GeV Higgs signal is shown as colored lines.

improves the sensitivity, exploiting different signal to background ratios and background compositions. An optimisation based on the expected exclusion limit for a 125 GeV Higgs boson [93] resulted in an optimum of three $p_T^{\mu\mu}$ categories, which is illustrated in Figure 6.11.

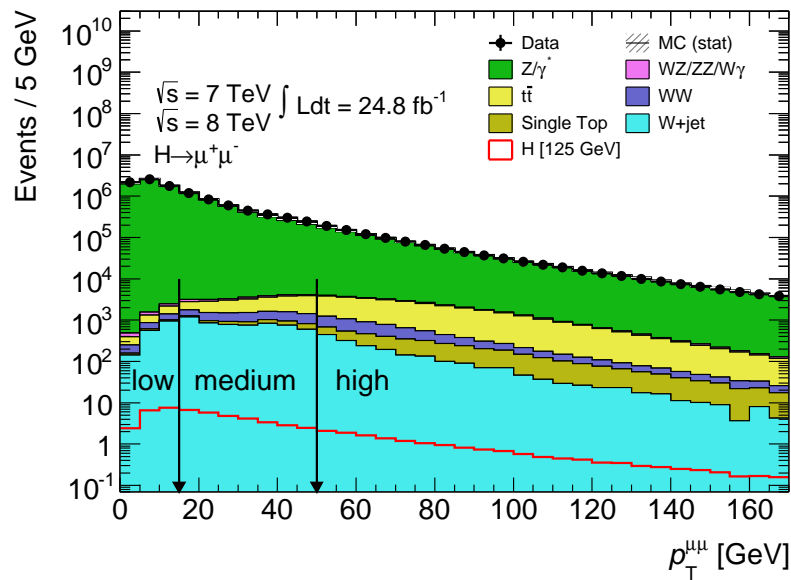


Figure 6.11: Illustration of the three $p_T^{\mu\mu}$ categories shown in the dimuon transverse momentum spectrum of the 7 and 8 TeV datasets. The category boundaries are indicated by black arrows. Different simulated background components are color-coded stacked histograms, and the expected signal for a Higgs boson with a mass of 125 GeV is shown as a red line.

The three categories are hence referred to as *low*, *medium* and *high* $p_T^{\mu\mu}$, respectively. The workflow to categorise an event is summarised in Figure 6.12, and in total there are 7 analysis categories in the combined 2011+2012 analysis:

- VBF
- low $p_T^{\mu\mu}$ central
- low $p_T^{\mu\mu}$ non-central
- medium $p_T^{\mu\mu}$ central
- medium $p_T^{\mu\mu}$ non-central
- high $p_T^{\mu\mu}$ central
- high $p_T^{\mu\mu}$ non-central.

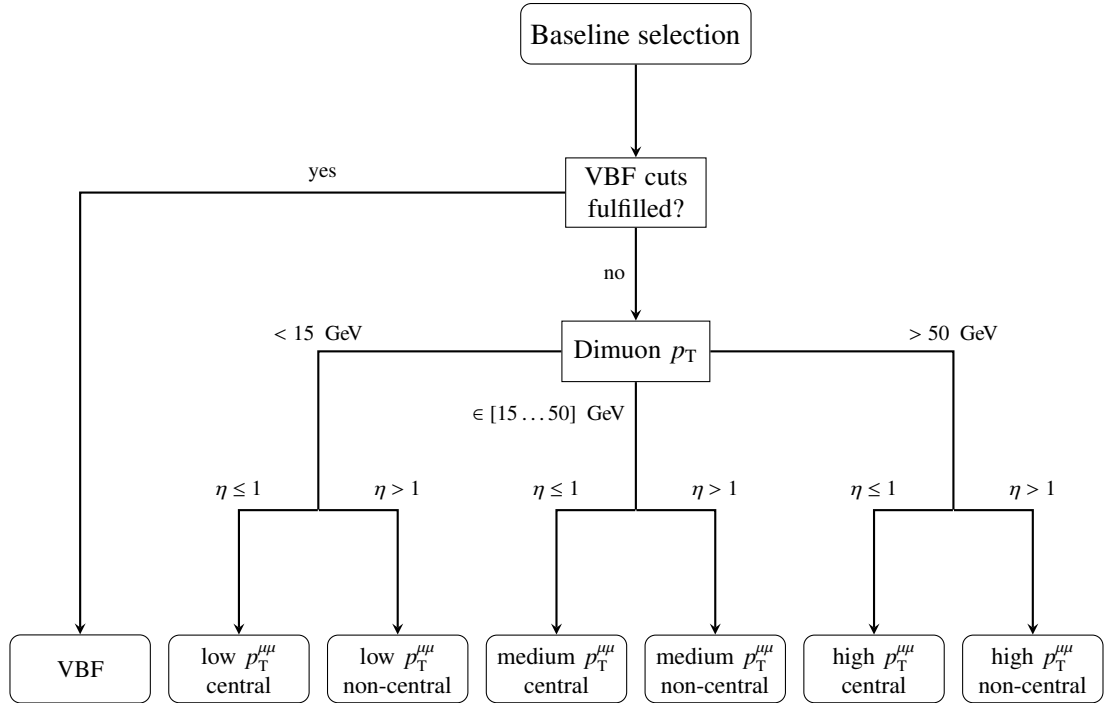


Figure 6.12: Flow chart of the event categorisation after the baseline selection for the combined 2011+2012 analysis.

The number of expected signal and background events as well as the observed data events for different stages in the combined analysis is summarised as a cutflow in Table 6.5

	Signal [125 GeV]	WW	WZ/ZZ/W γ	$t\bar{t}$	Single Top	Z+jets	W+jets	Total Bkg.	Observed	Data/MC
MC weights	65.69 ± 0.26	8600 ± 13	5781 ± 17	41020 ± 27	3927 ± 9	12092700 ± 3500	109100 ± 500	12261100 ± 3500	12381483	1.01 ± 0.00
$p_T^{\mu_1} > 25$ GeV	65.38 ± 0.25	8294 ± 12	5335 ± 16	40046 ± 27	3840 ± 9	11381600 ± 3400	77300 ± 400	11516400 ± 3400	11557343	1.00 ± 0.00
OS leptons	65.32 ± 0.25	8294 ± 12	4618 ± 13	40008 ± 27	3811 ± 9	11381600 ± 3400	5130 ± 40	11443400 ± 3400	11554933	1.01 ± 0.00
$m_{\mu\mu} > 70$ GeV	65.16 ± 0.25	5175 ± 10	3780 ± 12	25771 ± 22	2516 ± 7	10669800 ± 3300	1863 ± 27	10708900 ± 3300	10718377	1.00 ± 0.00
$p_T^{\mu_2} > 15$ GeV	64.67 ± 0.25	5082 ± 10	3683 ± 12	25172 ± 21	2451 ± 7	10561300 ± 3300	1480 ± 24	10599200 ± 3300	10610793	1.00 ± 0.00
$105 < m_{\mu\mu} < 160$ GeV	63.88 ± 0.25	1691 ± 6	193.8 ± 2.9	8918 ± 13	872 ± 4	249340 ± 180	452 ± 13	261470 ± 180	271330	1.04 ± 0.00
$E_T^{\text{miss}} < 80$ GeV	63.58 ± 0.25	1485 ± 5	164.2 ± 2.7	5837 ± 10	619.1 ± 3.5	249100 ± 180	388 ± 12	257590 ± 180	267602	1.04 ± 0.00
VBF signal region	1.500 ± 0.020	5.02 ± 0.27	0.86 ± 0.17	15.5 ± 0.5	1.89 ± 0.23	478 ± 6	2.4 ± 0.9	504 ± 6	512	1.02 ± 0.01
$p_T^{\mu\mu} < 15$ GeV, non-central	11.90 ± 0.12	150.2 ± 1.6	15.2 ± 0.7	166.3 ± 1.7	19.0 ± 0.6	104920 ± 120	59 ± 5	105320 ± 120	111102	1.05 ± 0.00
$p_T^{\mu\mu} < 15$ GeV, central	4.57 ± 0.08	31.0 ± 0.7	2.99 ± 0.25	58.7 ± 1.1	7.3 ± 0.4	26740 ± 60	3.1 ± 1.1	26840 ± 60	28547	1.06 ± 0.00
$15 < p_T^{\mu\mu} < 50$ GeV, non-central	20.90 ± 0.15	670.7 ± 3.5	65.8 ± 1.8	1320 ± 5	149.1 ± 1.7	70390 ± 100	166 ± 8	72760 ± 100	74629	1.03 ± 0.00
$15 < p_T^{\mu\mu} < 50$ GeV, central	8.21 ± 0.09	138.9 ± 1.6	13.5 ± 0.7	472.1 ± 2.9	50.4 ± 1.0	18880 ± 50	14.4 ± 2.5	19570 ± 50	19891	1.02 ± 0.00
$p_T^{\mu\mu} > 50$ GeV, non-central	11.44 ± 0.09	399.7 ± 2.7	54.2 ± 1.7	2683 ± 7	270.4 ± 2.3	20970 ± 50	115 ± 7	24500 ± 50	24978	1.02 ± 0.00
$p_T^{\mu\mu} > 50$ GeV, central	4.85 ± 0.06	88.8 ± 1.3	11.4 ± 0.6	1014 ± 4	115.7 ± 1.5	6640 ± 26	25.2 ± 3.1	7895 ± 26	7751	0.98 ± 0.00

Table 6.5: Expected number of signal and background events after each selection step of the combined 2011+2012 analysis. The observed number of events in collision data is given in the second last column, and the ratio between data and Monte Carlo expectation is shown in the last column. [93]

7 Signal and Background Modeling

The presented analysis is based on an accurate analytical model of both the signal and background dimuon invariant mass distributions. This chapter will describe these models and their properties in detail. Section 7.1 is hereby dedicated to the signal model, which is common for both the standalone 2012 and combined 2011-2012 data analyses, and section 7.2 focusses on the employed background models.

7.1 Signal Modeling

This section will elaborate on the functional form used to parametrise the expected dimuon invariant mass shape from Higgs decays to a muon-antimuon pair. The predicted natural width of the Standard Model Higgs within the investigated mass range varies between 2.85 MeV for $m_H = 110$ GeV and 17.3 MeV for $m_H = 150$ GeV. Since this width is much smaller than the dimuon mass resolution of the ATLAS detector (which is of the order of a few GeV, see section 5), the signal model is completely driven by detector resolution effects on a narrow resonance in the dimuon spectrum. Therefore, the chosen functional form is the sum of a Crystal Ball (CB) [96] and a Gaussian (GS) function, as defined in equation 7.1. The CB part hereby accounts for most of the resolution effects and radiative energy losses, whereas the Gaussian function models higher order resolution effects.

$$f_{SIG}(x, N_0, M, \sigma, \alpha, n) = N_0(f \cdot \underbrace{CB(x, M, \sigma_{CB}, \alpha, n)}_{\text{Crystal Ball}} + (1 - f) \cdot \underbrace{G(x, M, \sigma_G)}_{\text{Gaussian}}), \quad (7.1)$$

where the Crystal Ball function is defined as

$$CB(x, M, \sigma, \alpha, n) = \begin{cases} e^{\left(-\frac{(x-M)^2}{2\sigma_{CB}^2}\right)} & \text{if } \frac{x-M}{\sigma_{CB}} > -\alpha \\ A \cdot \left(B - \frac{x-M}{\sigma_{CB}}\right)^{-n} & \text{if } \frac{x-M}{\sigma_{CB}} \leq -\alpha \end{cases}. \quad (7.2)$$

The coefficients A, B are defined such that the function and its first derivative is smooth at the transition point between the gaussian core and the power law tail:

$$A = \left(\frac{n}{|\alpha|}\right)^n \cdot e^{-\frac{|\alpha|^2}{2}},$$

$$B = \frac{n}{|\alpha|} - |\alpha|.$$

In order to stabilise the fit, some of the function parameters have been fixed [92]. In particular, the exponent n of the Crystal Ball is fixed to $n = 2$, the transition point α between the Crystal Ball power tail and its Gaussian core is set to $\alpha = 1.75$ and the fraction f of the Crystal Ball is fixed to $f = 0.9$. The other parameters and the overall normalization N_0 , and hence the number of expected signal events, are left free floating in the signal fit. The model performance for a simulated Higgs boson mass of 125 GeV for the two standalone analysis categories is shown in Figure 7.1, and for the seven categories of the combined analysis for a centre-of-mass energy of $\sqrt{s} = 8$ TeV in Figure 7.2.

The signal model as defined in equation 7.1 is used for all tested mass hypotheses in both the standalone and the combined search. To obtain the results presented in chapter 10, all of the signal shape parameters are fixed to their expected values, obtained from fits to MC simulated distributions. Thus, the shape parameters need to be fixed for each tested mass point. However, signal MC are not available for each mass hypothesis, so the shape parameters need to be extrapolated between the available mass points. The mean M and widths σ_{CB}, σ_G are interpolated with a first order polynomial, and the expected event yield for each mass hypothesis is extrapolated with a fourth-order polynomial, following the expectation of the Higgs boson cross section times branching ratio as a function of the Higgs boson mass (see section 2.2.2). The interpolation interleaved with the signal model fits to the simulated dimuon spectra is shown in Figure 7.3 for the standalone analysis categories, and in Figure 7.4 for the combined analysis categories for a centre-of-mass energy of $\sqrt{s} = 8$ TeV.

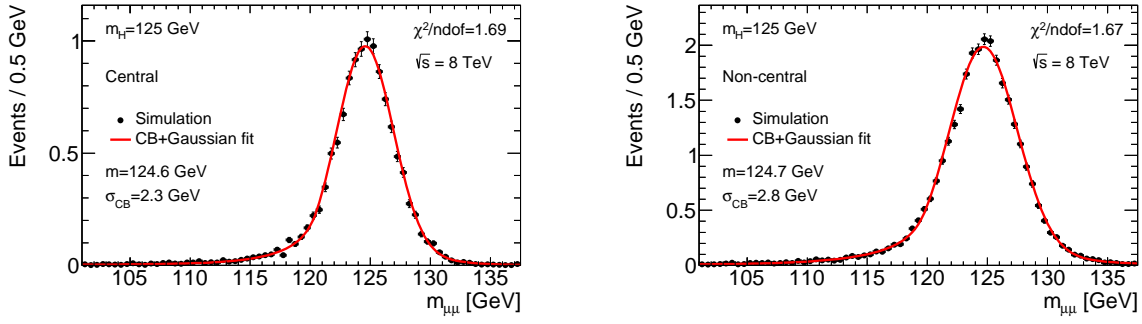


Figure 7.1: Invariant dimuon mass distribution and signal fit for the standalone analysis for a simulated Higgs boson with a mass of $m_H = 125$ GeV. The left plot shows the distribution for the central resolution category, and the right plot depicts the non-central category. The black dots mark the simulated mass distribution, and the fit is indicated by the red line. The parameters M and σ_{CB} of the signal fit are also shown.

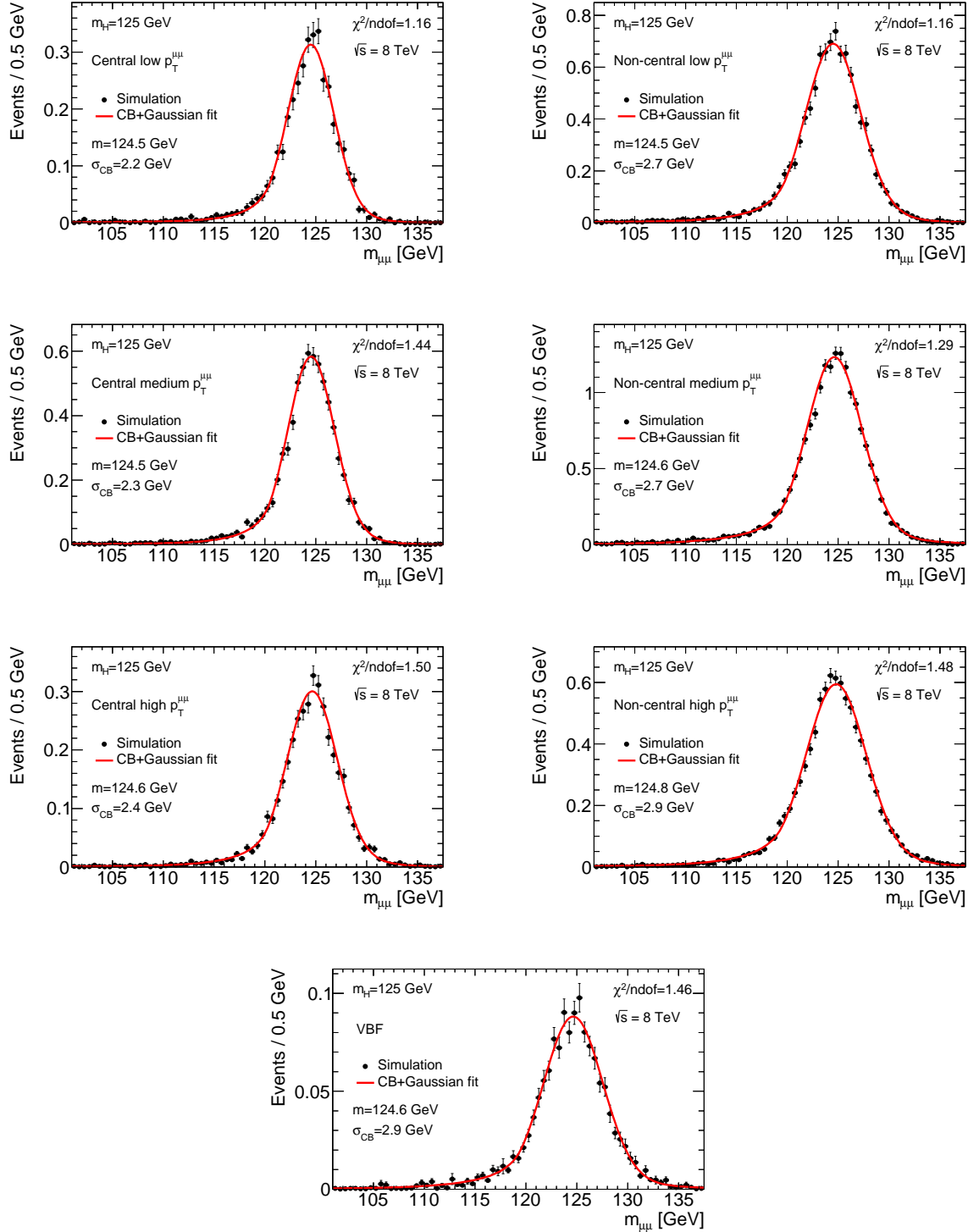


Figure 7.2: Invariant dimuon mass distributions and signal fits in the combined analysis categories for a simulated Higgs boson with a mass of $m_H = 125$ GeV.

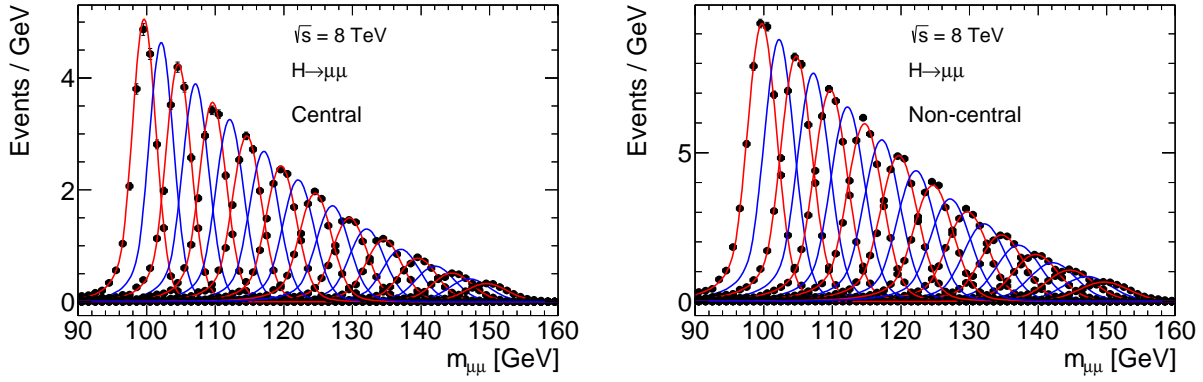


Figure 7.3: Interpolation of the signal model for different Higgs mass hypotheses in the standalone analysis. The simulated data points are shown as black points, the signal model fit is depicted as red lines, and the interpolated models for a collection of Higgs boson mass hypotheses is shown as blue lines.

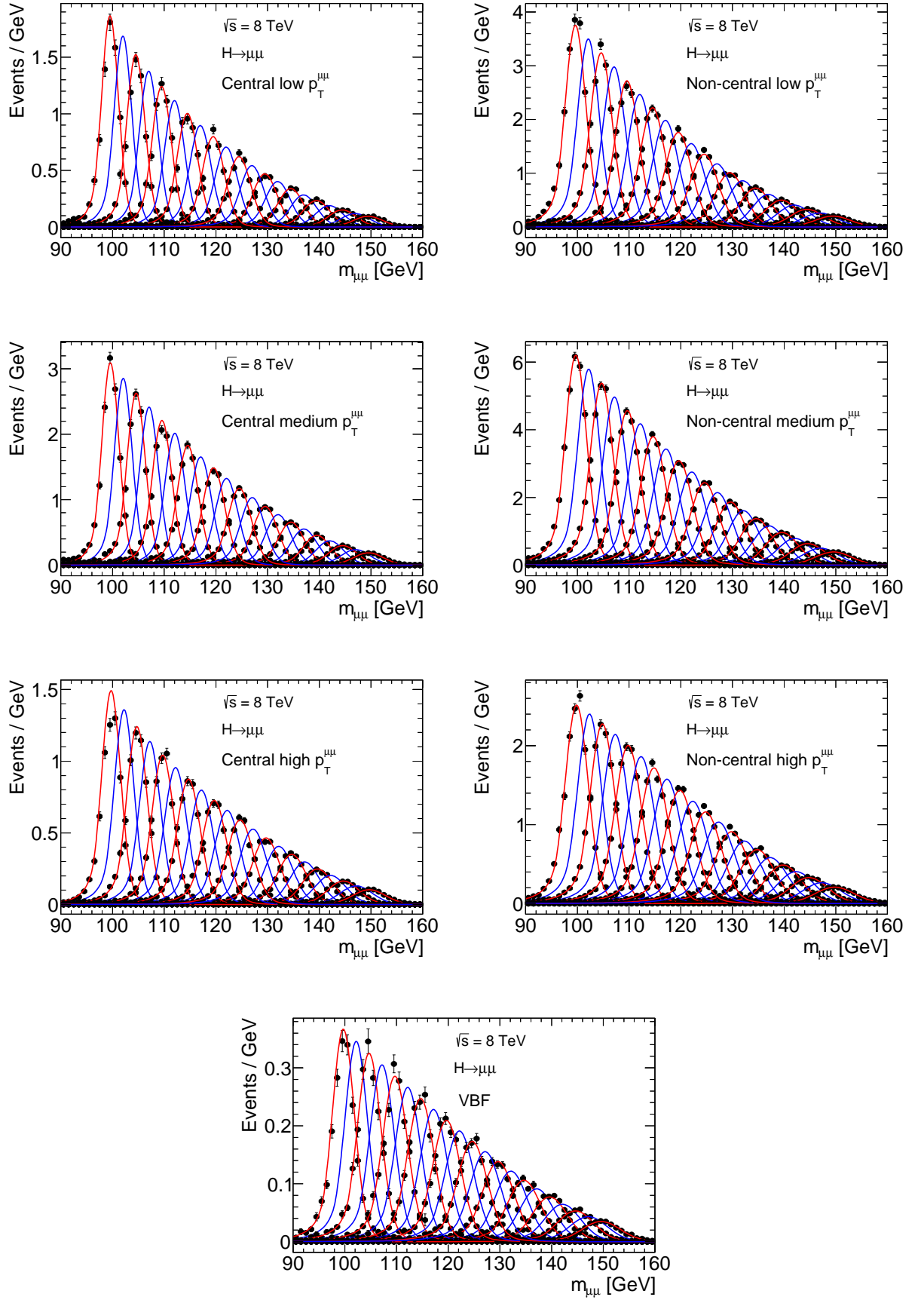


Figure 7.4: Interpolation of the signal model for different Higgs mass hypotheses in the combined analysis categories for a center-of-mass energy of $\sqrt{s} = 8$ TeV. The simulated data points are shown as black points, the signal model fit is depicted as red lines, and the interpolated models for a collection of Higgs boson mass hypotheses is shown as blue lines.

7.2 Background Modeling

In this section, the background estimation in the search for $H \rightarrow \mu^+\mu^-$ will be described. The strategy of performing a global fit with a signal plus background p.d.f. of the invariant dimuon mass spectrum puts high and partially concurring demands on the background model. The global fit has to be stable, so a simple model with only a few free parameters is preferred. On the other hand, the background model has to describe the expected background very well to avoid any fit bias. On top of that, the model has to be flexible enough to account for varying background compositions and different background sources.

The major expected background component originates from the Standard Model $Z/\gamma^* \rightarrow \mu^+\mu^-$ process (see section 6.2). This process is very well understood both experimentally [97] and theoretically (c.f. section 2.2.1). However, a simple description of the invariant dimuon mass spectrum including the Z peak is not possible due to non-linear momentum-dependent detector resolution effects [73], and the interference term between the s-channel Z and virtual photon exchange. Therefore, the choice of the background model, though motivated by the underlying physical process, is based on its performance in the region of interest of the presented analyses.

The performance and validity of the background model is evaluated both on Monte Carlo simulated background spectra and data control regions for the standalone analysis. The lack of a data control region for the combined analysis demands the performance to be evaluated on Monte Carlo simulated events only. This poses a problem insofar as it then becomes potentially sensitive to systematic uncertainties of the underlying simulated spectra. Albeit, none of the free parameters in the background model is actually fixed from fits to simulated distributions, but instead left free floating during the calculation of the observed limits, so the final shape and normalization of the background is determined from the fits to the observed data spectra.

7.2.1 Standalone Analysis Background Model

In the 8 TeV standalone analysis, one single background model for its two resolution categories is used. The model consists of a Breit-Wigner core and an additional exponential function, defined as:

$$f_{BKG}(x, N_0, B, f) = N_0 \cdot \left(f \cdot \underbrace{\frac{1}{(x - M_{BW})^2 + \left(\frac{\Gamma_{BW}}{2}\right)^2}}_{\text{Breit-Wigner}} + (1 - f) \cdot \underbrace{e^{B \cdot x}}_{\text{exp.}} \right). \quad (7.3)$$

The Breit-Wigner part of the function hereby models most of the $Z \rightarrow \mu^+\mu^-$ contribution to the total background expectation, and the exponential function is intended to cover both the falling Drell-Yan component and non-Drell-Yan backgrounds. The absolute normalisation is expressed in the N_0 parameter. The Breit-Wigner mass parameter M_{BW} and the width parameter Γ_{BW} are hereby fixed to the expected values for the Z boson, obtained from the global average given by the Particle Data Group [18], such that $M_{BW} \stackrel{!}{=} M_Z = 91.2$ GeV, and $\Gamma_{BW} \stackrel{!}{=} \Gamma_Z = 2.46$ GeV. Strictly speaking, the non-relativistic Breit-Wigner shape in (7.3) is incorrect, because the Z lineshape component follows a relativistic Breit-Wigner distribution (see section 2.2.1). However, this apparent flaw was not discovered before the results were finalised, and a significant improvement by using the correct form is not expected. Fit results to Monte-Carlo simulated background spectra in the signal categories are shown in Figure 7.5 and to the data control region in Figure 7.6.

7.2.1.1 Goodness-of-fit Studies The performance of the background fit model is evaluated using both its χ^2 value and utilising toy experiments. Since the background fit is carried out via a binned maximum likelihood fit, the χ^2 normalised to the number of degrees of freedom, $\chi^2/ndof$, is expected to be close to one [98]. This is observed in both the fits to MC spectra, and in the fits to the data control region. Moreover, the integrated pull distribution is expected to follow a normal Gaussian distribution

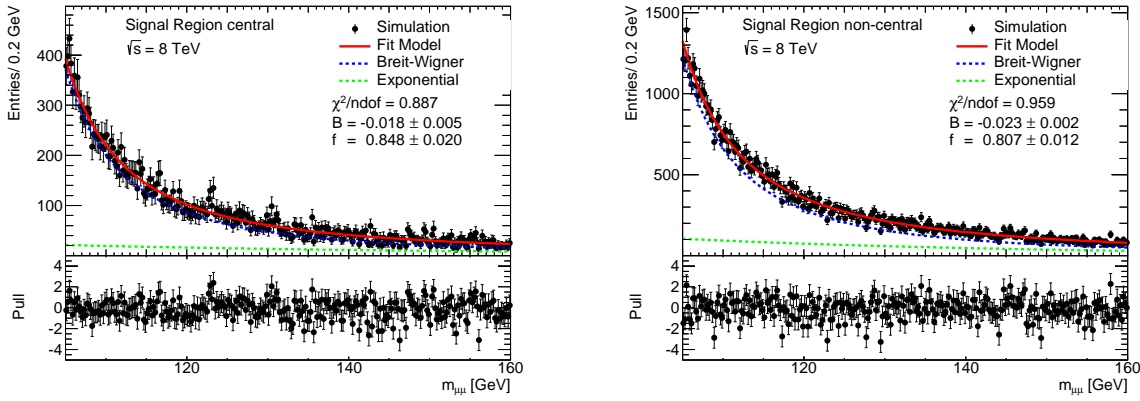


Figure 7.5: Simulated dimuon invariant mass distributions and background fit for the signal region in the central (left) and non-central (right) resolution categories. The black dots mark the simulated mass distribution, and the fit model is indicated by the blue red. The two function components are also shown individually by the dotted blue and green lines, respectively. The bottom plots depict the differential pull distribution.

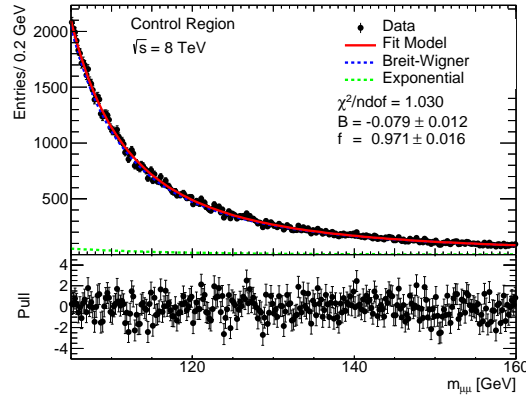


Figure 7.6: Dimuon invariant mass distributions and background fit for the data control region. The black dots mark the data mass distribution, and the fit model is indicated by the red line. The two function components are also shown individually by the blue and green lines, respectively. The bottom plots depict the differential pull distribution.

with a mean of zero and a standard deviation of one. This is also observed, as shown in Figures 7.7 and 7.8.

To investigate the stability of the background model, a toy study is employed. Hereby, the expected background dimuon invariant mass distribution is used as a template to generate 1000 distributions with the same statistical properties, and then apply the background model fit to each one of them. The fit parameter distributions, the parameter uncertainties and the resulting parameter pull distributions are then examined for unexpected features. These distributions are shown in Figure 7.9. No bias is observed for either of the fit parameters, and the fit model is therefore used without assigning a systematic uncertainty.

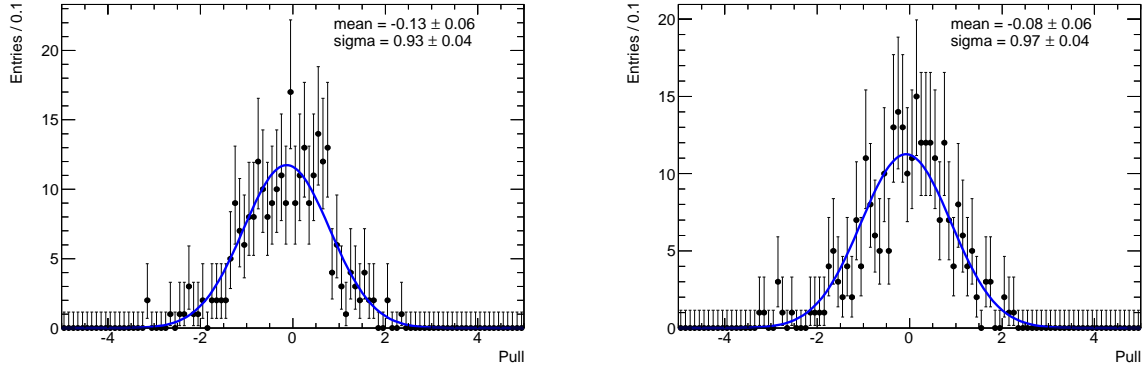


Figure 7.7: Integrated pull distributions obtained from the background model fit to the simulated dimuon mass spectrum in the signal region for central (left) and non-central (right) events. The pulls are integrated over the whole range of the differential pulls shown on the bottom of Figure 7.5. A Gaussian function is fitted to the pull distribution, and its parameters are shown.

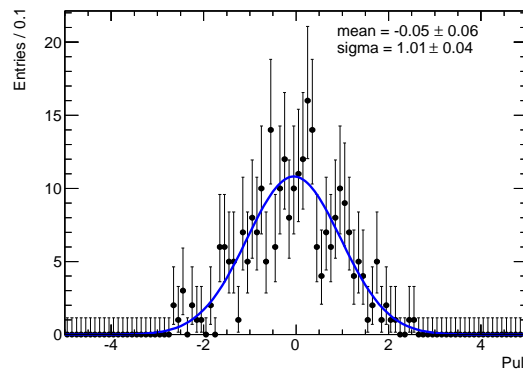


Figure 7.8: Integrated pull distribution obtained from the background model fit to the dimuon mass spectrum in the data control region. The pull is integrated over the whole range of the differential pull shown on the bottom of Figure 7.6. A Gaussian function is fitted to the pull distribution, and its parameters are shown.

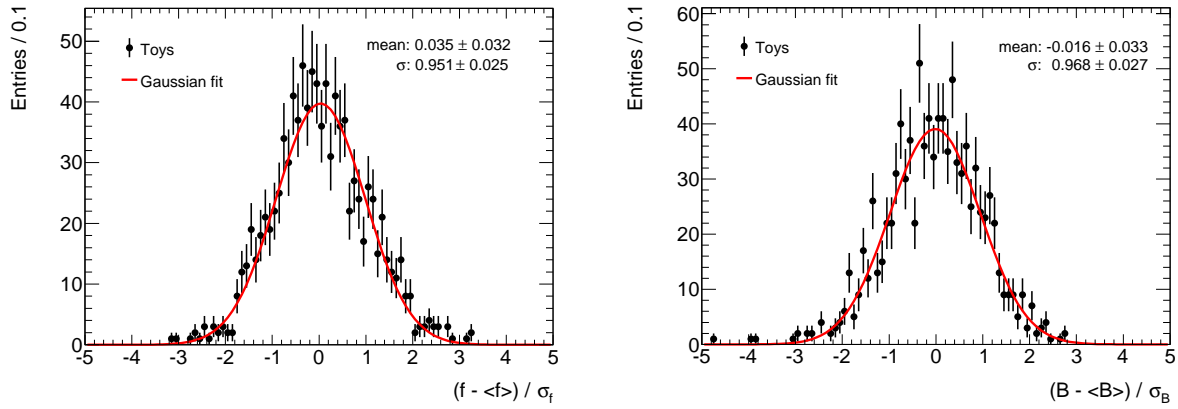


Figure 7.9: Pull distributions for the two free fitting parameters in the background model: the fraction parameter f (left) and the exponential parameter B (right). The distributions are obtained from fits to 1000 generated toy invariant mass distributions for the simulated signal region. A Gaussian function is fitted to the pull distribution, and its parameters are shown.

7.2.2 Combined Analysis Background Model

7.2.2.1 Background Model for the $p_T^{\mu\mu}$ categories For the combined analysis, the background model discussed in section 7.2.1 is used as a starting point. However, the addition of more analysis categories (c.f. section 6.2) and the availability of MC simulated samples with better statistical significance requires further fine-tuning and investigation of the background model behaviour. For the $p_T^{\mu\mu}$ categories, the background model was refined to include a first-order resolution term, modeled by a convolution of a Gaussian function and the Breit-Wigner function. In addition, a $\frac{1}{x^3}$ term is multiplied to the exponential function to better account for the Drell-Yan contribution to the dimuon background distribution (c.f. section 2.2.1). The refined background model for the $p_T^{\mu\mu}$ categories is thus defined as follows:

$$f_{BKG}(x, N_0, B, f) = N_0 \left(f \cdot \frac{1}{(x - M_{BW})^2 + \left(\frac{\Gamma_{BW}}{2}\right)^2} * \frac{1}{\sqrt{2\pi\sigma_{GS}^2}} e^{-\frac{1}{2}\left(\frac{x}{\sigma_{GS}}\right)^2} + (1 - f) \cdot \frac{e^{B \cdot x}}{x^3} \right). \quad (7.4)$$

Again, m_{BW} and Γ_{BW} are fixed to the world average values for the Z -boson [18]. The determination of the width of the Gaussian resolution term, σ_{GS} , is described in the following paragraph.

7.2.2.2 Determination of the Mass Resolution The width of the Gaussian distribution for the resolution term in the refined background model (7.4) is determined by a fit of the mass difference distribution $m_{\mu\mu}^{reco} - m_{\mu\mu}^{truth}$, which is obtained from PowHEG $Z/\gamma^* \rightarrow \mu\mu$ simulated samples. The combined analysis selection and categorisation is applied (see section 6.3.3). In addition, a geometric matching with a distance parameter of $\Delta R < 0.01$ of the two reconstructed muons to their truth counterparts is imposed, and the difference between the truth and reconstructed invariant masses is obtained. This distribution is fitted with two different simple resolution models: a simple Gaussian distribution (SG) and the sum of two Gaussian distributions (CG+OG). The mass difference distributions along with the two resolution models for the $p_T^{\mu\mu}$ categories are presented in Figures 7.10 - Figures 7.12. Though slightly less performant, the

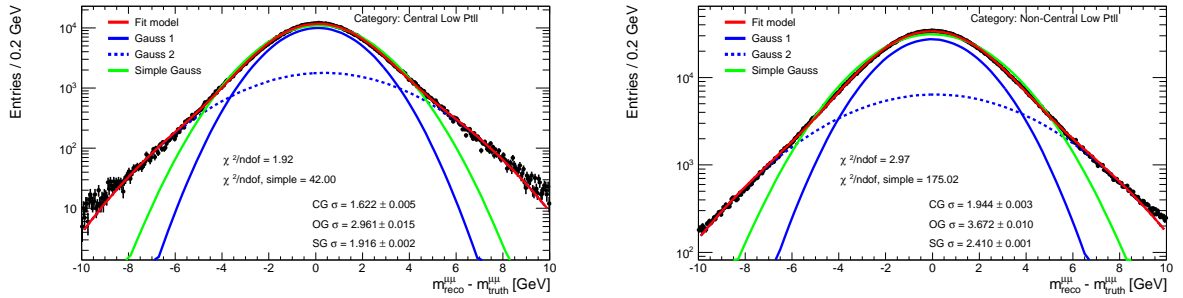


Figure 7.10: Dimuon mass difference distribution in the low $p_T^{\mu\mu}$ category for central (left) and non-central (right) events. The black points indicate the simulation, the simple Gaussian model fit is depicted as a green line and the sum of two Gaussians is shown in red, with the two components as solid and dashed blue lines. The $\chi^2/ndof$ for both fits is shown, as well as the widths σ of each component.

simple Gaussian resolution model is adopted for the combined analysis background model. The effects of the higher order resolution terms are partly modeled by the exponential component, and the functional form of the background model is kept as simple as possible to avoid computing performance issues. The resolutions utilised in the background model are collected in Table 7.1

7.2.2.3 Background Model for the VBF category The free parameters of equation 7.4 cannot be sufficiently constrained by the $m_{\mu\mu}$ spectrum in the VBF category, so a simplified background model

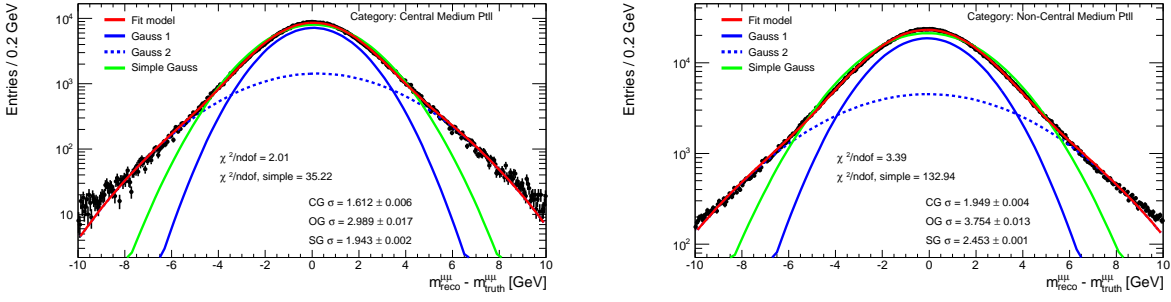


Figure 7.11: Dimuon mass difference distribution in the medium $p_T^{\mu\mu}$ category for central (left) and non-central (right) events. The black points indicate the simulation, the simple Gaussian model fit is depicted as a green line and the sum of two Gaussians is shown in red, with the two components as solid and dashed blue lines. The $\chi^2/ndof$ for both fits is shown, as well as the widths σ of each component.

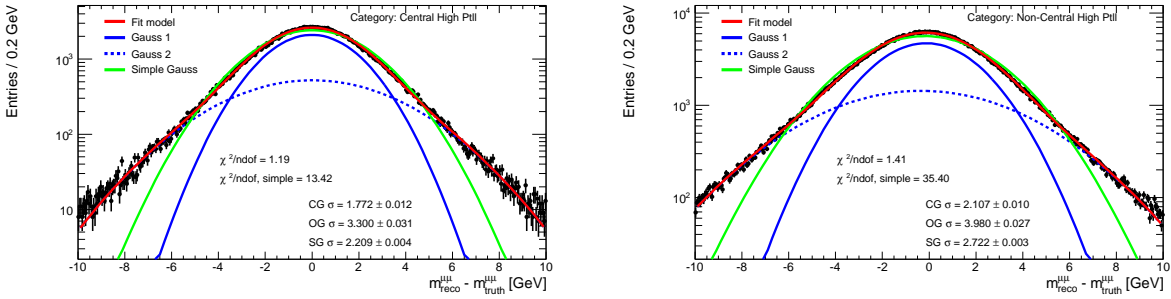


Figure 7.12: Dimuon mass difference distribution in the high $p_T^{\mu\mu}$ category for central (left) and non-central (right) events. The black points indicate the simulation, the simple Gaussian model fit is depicted as a green line and the sum of two Gaussians is shown in red, with the two components as solid and dashed blue lines. The $\chi^2/ndof$ for both fits is shown, as well as the widths σ of each component.

$p_T^{\mu\mu}$ category	σ_{GS} [GeV]
Lowl central	1.92
Low non-central	2.41
Medium central	1.94
Medium non-central	2.45
High central	2.21
High non-central	2.72

Table 7.1: Mass resolution parameters σ_{GS} for the combined analysis background model in the $p_T^{\mu\mu}$ categories, derived from the simple Gaussian fits to the mass difference spectra.

with only one free parameter is used there. It is defined as:

$$f_{VBF}(x, N_0, B) = N_0 \cdot \frac{e^{B \cdot x}}{(x - M_{BW})^2 + \left(\frac{\Gamma_{BW}}{2}\right)^2}. \quad (7.5)$$

7.2.2.4 Background Fit Results The background fit results to background only simulated invariant mass spectra are shown in figures 7.13-7.16 for each of the seven analysis categories. Besides the

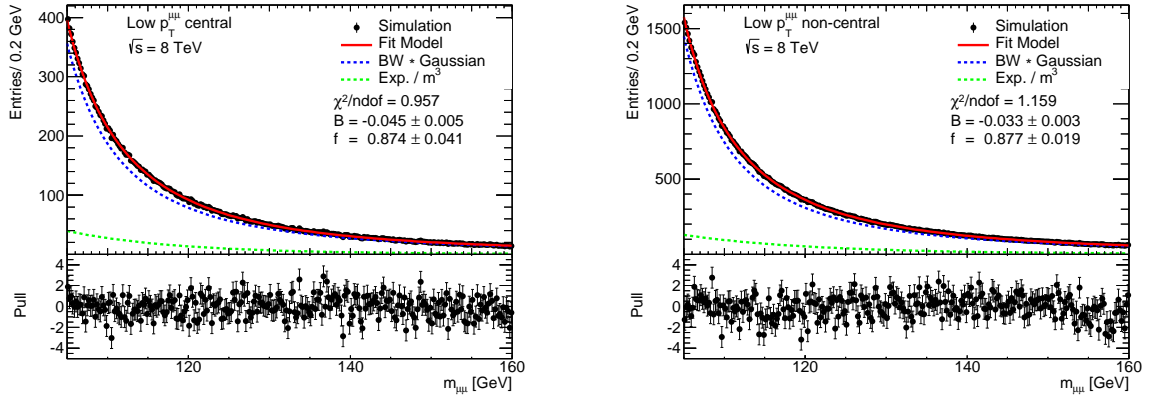


Figure 7.13: Background model fits and differential pull distributions in the low $p_T^{\mu\mu}$ category for central (left) and non-central(right) events, obtained from Monte Carlo simulated spectra. The simulated data points are shown in black, and the fit model is depicted in red. The individual components of the background model are indicated as dashed blue and green lines. The best fit parameters and the $\chi^2/ndof$ for the fit are also shown.

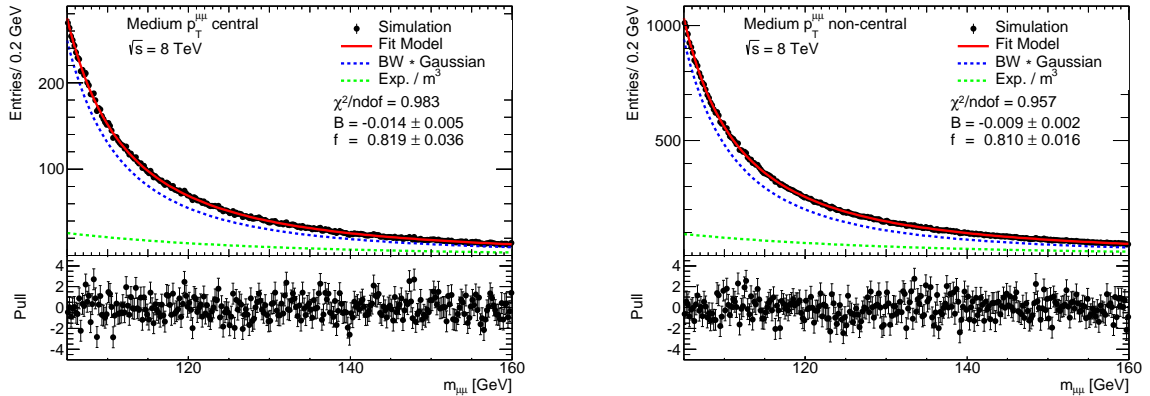


Figure 7.14: Background model fits and differential pull distributions in the medium $p_T^{\mu\mu}$ category for central (left) and non-central(right) events, obtained from Monte Carlo simulated spectra. The simulated data points are shown in black, and the fit model is depicted in red. The individual components of the background model are indicated as dashed blue and green lines. The best fit parameters and the $\chi^2/ndof$ for the fit are also shown.

$\chi^2/ndof$ values as a goodness-of-fit measure, the spurious signal technique is applied in the combined analysis to gauge the capability of the background models to correctly describe the expected background distribution. In addition, the spurious signal technique provides a quantification of any residual systematic bias introduced by the background model fit. The spurious signal method as employed in the combined analysis is described in detail in section 8.3.2.

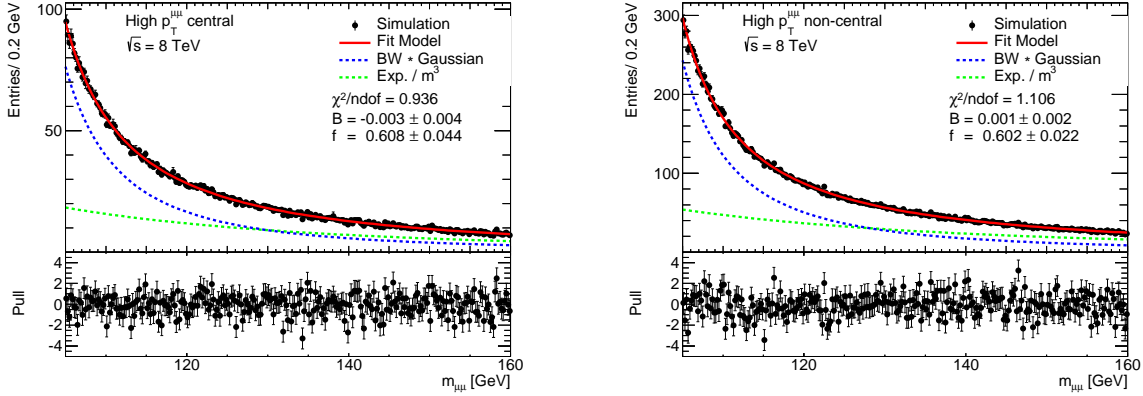


Figure 7.15: Background model fits and differential pull distributions in the high $p_T^{\mu\mu}$ category for central (left) and non-central(right) events, obtained from Monte Carlo simulated spectra. The simulated data points are shown in black, and the fit model is depicted in red. The individual components of the background model are indicated as dashed blue and green lines. The best fit parameters and the $\chi^2/ndof$ for the fit are also shown.

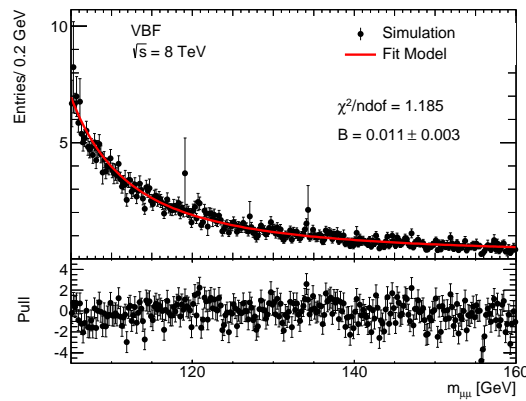


Figure 7.16: Background model fit and differential pull distribution in the VBF category, obtained from Monte Carlo simulated spectra. The simulated data points are shown in black, and the fit model is depicted in red. The best fit parameter and the $\chi^2/ndof$ for the fit are also shown.

8 Systematic Uncertainties

In this section, the systematic uncertainties affecting the search are presented. These are split into experimental systematic uncertainties which arise from measurement and calibration uncertainties of the detector, theoretical systematic uncertainties due to the methods of calculating cross sections and branching ratios, and methodical systematic uncertainties which are derived from the analysis strategy itself.

8.1 Experimental Systematic Uncertainties

The integrated luminosity is directly proportional to the number of expected signal events, therefore the uncertainty on the luminosity measurement plays a key role in the experimental systematic uncertainties. The remaining experimental systematic uncertainties can be classified in event-related uncertainties and object related uncertainties. The former include the uncertainty in the modeling of pile-up collisions and the expected muon trigger response in MC simulation, while the latter involve known discrepancies between expected and measured values of the muon momentum scale and resolution, and muon isolation. The inclusion of the VBF category for the combined analysis further requires the determination of jet and missing transverse energy (E_T^{miss}) related uncertainties, namely the jet energy scale (JES) and jet energy resolution (JER) and their impact on the missing transverse energy.

All systematic uncertainties discussed in this section are evaluated with respect to their impact on the expected signal yield, since the background normalisation is completely determined from the background model fit to the collision data spectrum, and only the expected signal yield is extracted from signal model fits to MC simulated samples. Thus, only uncertainties on the expected signal yield affect the fitted signal strength of the final result.

For the standalone 2012 analysis, a simplified treatment of the experimental systematic uncertainties is employed. They are evaluated for one single Higgs mass point of $m_H = 125$ GeV and applied as a global systematic uncertainty for each mass hypothesis. The experimental systematic uncertainties for the combined 2011-2012 data analysis are evaluated for each simulated Higgs mass point, and a linear function is used to interpolate between the mass points in case a mass-dependence is observed. A summary of the experimental systematic uncertainties for the standalone analysis is given in section 8.1.5, and the uncertainties derived for the combined analysis are summarised in section 8.1.6.

8.1.1 Uncertainty of the Luminosity Measurement

The luminosity is measured by dedicated detectors and specific algorithms monitoring the average particle flux in the ATLAS detector components (c.f. 3.2.7). Uncertainties in the luminosity measurement mainly arise from uncertainties in the *van de Meer* scan calibration [41]. The resulting relative uncertainty of the luminosity measurement is 1.8% for the 2011 dataset, and 2.8% for the 2012 dataset [99].

8.1.2 Pile-up Reweighting

The simulation of pile-up produces a different distribution of the number of interactions per proton bunch-crossing than observed in data. Therefore, the simulated events are reweighted such that these distributions agree (see section 6.2). Residual uncertainties of the pile-up event simulation originating from the minimum-bias modeling are accounted for by varying the original weight by $\pm 10\%$. The amount of pile-up interactions affects the jet and E_T^{miss} reconstruction, so this variation is also propagated to the jet and E_T^{miss} systematic uncertainties (c.f. section 8.1.4).

8.1.3 Muon Trigger, Reconstruction and Identification Uncertainties

The simulation of the muon trigger, reconstruction and identification are known to have tensions with their observed counterparts in collision data events. Therefore, corrections have to be applied in the form of trigger scale factors, muon momentum scale and resolution corrections, which depend on the muon momentum and pseudorapidity. These corrections are determined by the Muon Combined Performance

group through measurements using the Z -boson resonance in a tag-and-probe analysis [78]. The uncertainties of these measurements enter as systematic uncertainties. The evaluation of these uncertainties is described briefly in the following paragraphs.

8.1.3.1 Muon Trigger Uncertainties The simulated muon trigger efficiency is multiplied by a scale factor to match the observed muon trigger efficiency measured in a tag-and-probe analysis [80]. This scale factor depends on the trigger threshold, the p_T and η of the respective trigger object, and is within a few (< 2) percent of unity [80]. The systematic uncertainty connected with this scaling is evaluated by comparing the signal event yield obtained with regular scaling, and with the scale factor varied within its 1σ uncertainty.

8.1.3.2 Muon Reconstruction and Identification Uncertainty In analogy to the trigger scale factors, the reconstruction efficiency in MC simulated events is corrected to match the efficiency observed in data. This correction depends on the p_T and η of the muon, and is applied to each muon separately. Again, the systematic uncertainty is obtained by comparing the nominal signal event yield with the one when the efficiency scale factors are varied within their 1σ uncertainty.

A similar correction is applied to match the muon isolation efficiency in MC simulation and collision data using the *PtCone* and *EtCone* isolation criteria (see section 6.2). The uncertainties on the isolation efficiency scale factors propagate as systematic uncertainty to the analysis.

8.1.4 Jet and Missing Transverse Energy Related Uncertainties

The inclusion of the VBF analysis category in the combined 2011-2012 analysis introduces both jets and missing transverse energy as objects in the event selection (c.f section 6.3.3), and thus makes the combined analysis potentially sensitive to jet and E_T^{miss} uncertainties. The jet uncertainties are driven by uncertainties of the jet energy scale (JES), which is determined by a combination of testbeam studies of the calorimeter components, and a large variety of data-driven calibration methods [100]. The jet energy scale uncertainty is also dependent on the number of pile-up vertices, so variations of the amount of pile-up is taken into account. The uncertainties of the calibration are further propagated to the E_T^{miss} calculation, in addition to the aforementioned muon related uncertainties and pile-up variations.

8.1.5 Experimental Systematic Uncertainties for the Standalone Analysis

The standalone 2012 analysis is only affected by the luminosity uncertainty, the pile-up uncertainty and the systematics caused by muon related uncertainties. The former imposes a global normalisation uncertainty, while the latter are category-dependend. The muon related uncertainties described in detail in section 8.1.3 are evaluated for a Higgs boson mass of 125 GeV. The uncertainties are summarised in Table 8.1, and are used for the complete search range of the standalone analysis.

category	\mathcal{L} unc. [%]	pile-up [%]	trigger SF [%]	reco SF[%]	iso SF [%]
central	2.8	0.5	0.9	0.1	0.8
non-central	2.8	0.3	0.8	0.0	0.8

Table 8.1: Experimental systematic uncertainties of the signal event yield as used for the 2012 standalone analysis. The values are obtained from a simulated Higgs signal sample with a mass hypothesis of $m_H = 125$ GeV [101]. The systematic effect of the muon reconstruction scale factor uncertainty for non-central events is negligible.

8.1.6 Experimental Systematic Uncertainties Summary for the Combined Analysis

For the combined analysis, the experimental systematic uncertainties were derived for each of the available MC simulated Higgs signal mass points. Table 8.2 summarises the relative uncertainties in the signal yield for a simulated Higgs mass of 125 GeV. All experimental systematics except the luminosity uncertainty are combined to give one uncertainty in each category, split into the three production modes (ggF, VBF and VH), by adding the individual contributions in quadrature and taking the square root. Correlations between contributions are neglected.

Analysis Category	total yield uncertainty [%]					
	ggF mode		VBF mode		VH mode	
	7 TeV	8 TeV	7 TeV	8 TeV	7 TeV	8 TeV
Low $p_T^{\mu\mu}$ central	2.2	2.5	3.0	5.1	3.0	5.1
Low $p_T^{\mu\mu}$ non-central	2.1	2.0	3.0	4.3	2.6	3.2
Medium $p_T^{\mu\mu}$ central	2.2	2.5	3.0	4.1	2.5	3.1
Medium $p_T^{\mu\mu}$ non-central	2.1	2.1	2.8	3.6	2.4	2.3
High $p_T^{\mu\mu}$ central	2.2	2.8	3.9	5.3	2.4	2.6
High $p_T^{\mu\mu}$ non-central	2.2	2.4	3.6	4.6	2.4	2.2
VBF	21.4	20.5	9.3	8.1	26.5	28.1

Table 8.2: Experimental systematic uncertainties given as relative yield uncertainties for a Higgs mass hypothesis of $m_H = 125$ GeV. All uncertainties for one Higgs boson production process are combined by adding the individual contributions in quadrature.

8.2 Theoretical Systematic Uncertainties

Theoretical systematic uncertainties playing a key role in the presented analysis originate from the calculation of the SM Higgs boson production cross section and decay branching fraction. These two quantities are directly proportional to the number of expected signal events, and their associated uncertainties are discussed in sections 8.2.1 and 8.2.2. The impact of theoretical and MC generator related uncertainties on the signal acceptance is covered in section 8.3.1.

8.2.1 Higgs Boson Production Cross Section Uncertainty

The SM Higgs production cross sections for proton-proton collisions are calculated by the LHC cross-section working group. The different Higgs boson production modes are investigated separately, and dedicated analytical calculations and tools are used in each of them [24][102].

8.2.1.1 Gluon-Fusion Production Mode The cross-section for the gluon-fusion Higgs boson production is calculated at full next-to-leading order (NLO) in QCD, with next-to-next-to leading order (NNLO) QCD corrections and NLO EW corrections applied [24]. Uncertainties arise from the omission of higher order QCD terms, estimated through the scale uncertainty of the renormalisation and factorisation scales, μ_F and μ_R . Additional uncertainties originate from the parton distribution function and the uncertainty of the strong coupling α_S . The gluon-fusion Higgs boson production cross sections and their uncertainties are summarised in Table 8.3.

8.2.1.2 Vector-Boson Fusion Production Mode The vector-boson fusion production cross-sections are calculated including full NLO electroweak and NNLO QCD corrections, under the assumption that these contributions completely factorise [24]. The scale and PDF+ α_S uncertainties are a factor of ≈ 5

m_H [GeV]	σ [pb]	7 TeV		σ [pb]	8 TeV	
		scale	PDF		scale	PDF
110	19.56	$+7.5\%$ -8.1%	$+7.7\%$ -6.9%	24.70	$+7.6\%$ -8.2%	$+7.7\%$ -6.7%
115	17.89	$+7.4\%$ -8.0%	$+7.7\%$ -7.0%	22.66	$+7.4\%$ -8.1%	$+7.6\%$ -6.8%
120	16.43	$+7.2\%$ -7.9%	$+7.6\%$ -7.0%	20.86	$+7.3\%$ -7.9%	$+7.5\%$ -6.9%
125	15.13	$+7.1\%$ -7.8%	$+7.6\%$ -7.1%	19.27	$+7.2\%$ -7.8%	$+7.5\%$ -6.9%
130	13.98	$+7.0\%$ -7.7%	$+7.6\%$ -7.2%	17.85	$+7.1\%$ -7.7%	$+7.5\%$ -6.9%
135	12.95	$+6.9\%$ -7.6%	$+7.6\%$ -7.3%	16.57	$+7.0\%$ -7.7%	$+7.4\%$ -7.0%
140	12.02	$+6.8\%$ -7.5%	$+7.6\%$ -7.3%	15.42	$+6.9\%$ -7.6%	$+7.4\%$ -6.9%
145	11.24	$+6.7\%$ -7.5%	$+7.6\%$ -7.4%	14.46	$+6.8\%$ -7.5%	$+7.3\%$ -6.9%
150	10.51	$+6.6\%$ -7.4%	$+7.6\%$ -7.5%	13.55	$+6.7\%$ -7.4%	$+7.4\%$ -7.0%

Table 8.3: Higgs boson production cross-section and uncertainties in the gluon-fusion mode for different Higgs mass hypotheses [102]. The uncertainties are separated in scale uncertainties and PDF+ α_S uncertainties.

m_H [GeV]	σ [pb]	7 TeV		σ [pb]	8 TeV	
		scale	PDF		scale	PDF
110	1.410	$+0.4\%$ -0.3%	$+2.2\%$ -2.1%	1.809	$+0.3\%$ -0.2%	$+2.5\%$ -2.8%
115	1.344	$\pm 0.2\%$	$+2.3\%$ -2.1%	1.729	$\pm 0.2\%$	$+2.5\%$ -2.8%
120	1.279	$+0.3\%$ -0.4%	$+2.4\%$ -2.1%	1.649	$\pm 0.2\%$	$+2.6\%$ -2.8%
125	1.222	$\pm 0.3\%$	$+2.5\%$ -2.1%	1.578	$\pm 0.2\%$	$+2.6\%$ -2.8%
130	1.168	$+0.3\%$ -0.2%	$+2.5\%$ -2.1%	1.511	$\pm 0.2\%$	$+2.6\%$ -2.7%
135	1.117	$+0.5\%$ -0.1%	$+2.6\%$ -2.1%	1.448	$\pm 0.2\%$	$+2.6\%$ -2.7%
140	1.069	$\pm 0.2\%$	$+2.6\%$ -2.1%	1.389	$\pm 0.2\%$	$+2.5\%$ -2.7%
145	1.023	$+0.4\%$ -0.0%	$+2.7\%$ -2.1%	1.333	$+0.3\%$ -0.1%	$+2.5\%$ -2.7%
150	0.980	$+0.2\%$ -0.1%	$+2.7\%$ -2.1%	1.280	$+0.3\%$ -0.2%	$+2.5\%$ -2.7%

Table 8.4: Higgs boson production cross-section and uncertainties in the VBF mode for different Higgs mass hypotheses [102]. The uncertainties are separated in scale uncertainties and PDF+ α_S uncertainties.

smaller than for the gluon-fusion production process, since the QCD contributions to the VBF topology are driven by small vertex corrections to the EW vertices in the dominant t - and u -channel diagrams [103] (see section 2.2.2). The cross-sections and their respective uncertainties for different Higgs boson mass hypotheses are collected in Table 8.4.

m_H [GeV]	7 TeV		8 TeV	
	σ [pb] \pm unc.		σ [pb] \pm unc.	
	WH mode	ZH mode	WH mode	ZH mode
110	0.884 \pm 3.3 %	0.498 \pm 5.0 %	1.071 \pm 3.4 %	0.613 \pm 5.1 %
115	0.763 \pm 3.4 %	0.435 \pm 5.4 %	0.927 \pm 3.3 %	0.536 \pm 5.3 %
120	0.662 \pm 3.5 %	0.381 \pm 5.6 %	0.805 \pm 3.4 %	0.471 \pm 5.5 %
125	0.579 \pm 3.5 %	0.335 \pm 5.6 %	0.705 \pm 3.3 %	0.415 \pm 5.6 %
130	0.506 \pm 3.6 %	0.296 \pm 5.8 %	0.617 \pm 3.3 %	0.367 \pm 5.7 %
135	0.443 \pm 3.5 %	0.262 \pm 6.0 %	0.542 \pm 3.4 %	0.326 \pm 6.1 %
140	0.390 \pm 3.5 %	0.232 \pm 6.2 %	0.477 \pm 3.3 %	0.290 \pm 6.3 %
145	0.344 \pm 3.7 %	0.207 \pm 6.3 %	0.422 \pm 3.4 %	0.258 \pm 6.5 %
150	0.303 \pm 3.7 %	0.184 \pm 6.6 %	0.373 \pm 3.5 %	0.231 \pm 6.6 %

Table 8.5: Associated Higgs boson production cross-section and uncertainties for different Higgs mass hypotheses [102], shown separately for WH and ZH modes. The uncertainty of the latter is larger due to additional gluon-induced NNLO diagrams not present for WH [24].

8.2.1.3 Production through Higgs-strahlung The cross-section calculation of the associated Higgs boson production together with a weak vector boson (Higgs-strahlung) involves NLO EW and NNLO QCD corrections. The cross-sections and their scale and PDF+ α_S uncertainties for the associated production are presented in Table 8.5.

m_H [GeV]	$\frac{\Gamma_{H \rightarrow \mu^+ \mu^-}}{\Gamma_{\text{tot}}} [\times 10^{-4}]$	total unc.
110	2.76	+7.0% -6.8%
115	2.63	+6.7% -6.6%
120	2.44	+6.4% -6.3%
125	2.20	+6.0% -5.9%
130	1.90	+5.5% -5.4%
135	1.55	+5.0% -4.9%
140	1.22	+3.7% -3.8%
145	0.91	+3.4% -3.4%
150	0.62	+3.1% -3.2%

Table 8.6: Branching ratios $\Gamma_{H \rightarrow \mu^+ \mu^-} / \Gamma_{\text{tot}}$ and their uncertainty for different Higgs boson masses. The quoted uncertainty is the combination of parametric and theoretical uncertainties [27].

8.2.2 Branching Ratio Uncertainty

Similarly to the production cross sections, the Higgs boson branching ratios and their respective uncertainties are provided by the LHC Higgs cross section working group [27]. The uncertainties in the branching ratio are parametric uncertainties arising from the input parameters of the calculation (such as quark masses), and theoretical uncertainties originating from higher order contributions omitted from the calculation. The branching ratios for different Higgs mass scenarios and their total uncertainty are given in Table 8.6.

8.3 Methodical Systematic Uncertainties

Two conceptual premisses in the analysis method presented in this thesis mark the entry point for potential systematic uncertainties housed in the method itself. At first, the expected signal normalization in each analysis category is derived from MC simulated events. Therefore, the expected exclusion limits are sensitive to systematic uncertainties from the signal acceptance in the categories. Secondly, the description of the background by an analytical function leaves the freedom of the actual choice of the functional form, and this choice has an influence on the results as well.

The standalone 2012 analysis has only one signal region with two resolution categories (see section 6.3.2), and the chosen background model is flexible enough to correctly model the background distributions both in MC simulation as well as the data control region without any observed bias, as shown in section 7.2.1. Thus, the focus is placed on the signal acceptance systematic uncertainty for the standalone analysis, and no systematic uncertainty is assigned to the choice of the background model. This signal acceptance uncertainty determination will be addressed in section 8.3.1.

In contrast to this, the seven analysis categories and the availability of MC simulated background samples with higher statistics for the combined analysis made it crucial to investigate the background model systematic uncertainties in more detail. This is done via the spurious signal technique, which will be described in detail in section 8.3.2.

8.3.1 Signal Acceptance Systematic Uncertainties

Besides the systematic uncertainties on the signal normalisation arising from sources discussed in sections 8.1 and 8.2, the placement of selection and categorisation cuts can affect the expected signal acceptance and thus the expected limits if the shape of the underlying distribution is sensitive to theoretical or simulation uncertainties. These shape systematics resulting in a changed acceptance is referred to as signal acceptance uncertainty. The signal acceptance uncertainties are studied separately for the standalone and the combined analyses. The common basic idea is that uncertainties on the signal production cross section and branching fraction on the one side and the aforementioned shape uncertainties on the other side are completely decoupled. Given that, the impact of uncertainties in the MC simulation are studied using the default event generator setup as for the nominal signal sample generation, and then varying the generation parameters within their uncertainties.

8.3.1.1 Acceptance Uncertainties of the Standalone Analysis In the standalone analysis, a custom setup was developed to study signal acceptance systematic effects. It consists of the POWHEG matrix element generator (c.f. section 4.2.1) interfaced to PYTHIA8 for the parton shower and PHOTOS++ [104] for QED radiation simulation. No detector simulation and event reconstruction is used at this stage, since systematic uncertainties due to these are already covered in the experimental systematic uncertainties described in section 8.1. The simulation output is analysed with a custom RIVET [105] analysis developed to resemble the standalone analysis selection cuts as closely as possible. This RIVET analysis involves the following selection steps:

- exactly two muons originating from the Higgs boson decay
- leading muon $p_T > 25$ GeV
- subleading muon $p_T > 15$ GeV
- both $|\eta_\mu| < 2.4$
- track isolation: $PtCone30/p_T < 0.15$
- opposite charge
- $p_T^{\mu\mu} > 15$ GeV

resolution category	ΔA , scales up [%]	ΔA , scales down [%]
central	0.3 ± 0.5	-2.1 ± 0.5
non-central	0.0 ± 0.3	0.7 ± 0.3

Table 8.7: Relative acceptance deviations ΔA in percent obtained by varying the renormalisation and factorisation scales. The statistical uncertainty of the deviations is also given.

Hereafter, the event categorisation in central (both $|\eta_\mu| < 1.0$) and non-central (at least one $|\eta_\mu| > 1.0$) events is applied. The calorimeter isolation requirement on the muons has to be dropped for obvious reasons, since there is no calorimeter information available without the detector simulation. Alas, no deterioration of the result is expected, since the efficiency and rejection of the isolation criteria is driven by the track-based PtCone isolation criterion, which is applied. The acceptance A after the analysis selection cuts is defined as:

$$A = \frac{N_{\text{passed}}}{N_{\text{total}}}, \quad (8.1)$$

where N_{passed} is the number of events passing the selection cuts and N_{total} is the total number of generated events. The relative difference of the acceptance between the nominal generator setup and the varied generator setup is then calculated as:

$$\Delta A_{\text{rel}} = \left(\frac{A_{\text{var}}}{A_{\text{nom}}} - 1 \right). \quad (8.2)$$

This quantity is then directly used as the acceptance systematic uncertainty. Three independent variations are studied:

- Renormalisation and factorisation scales μ_R, μ_F
- Initial and final state radiation (ISR and FSR)
- Parton distribution function (PDF).

Renormalisation and Factorisation Scales Perturbative QCD calculations have to be truncated, and the contribution of omitted terms are absorbed in the renormalisation and factorisation scales (see section 4.1). These two scales are highly correlated at leading and next-to-leading order [106], and an estimate of the systematic uncertainty introduced by the choice of the scales is obtained by coherently varying them with a factor. The renormalisation scale is thus multiplied by a factor of 1.1 (0.9), and at the same time the factorisation scale is multiplied by 2.0 (0.5), respectively. The chosen values give a good approximation on the residual scale dependence of relevant observables (e.g. $m_{\mu\mu}, p_T^{\mu\mu}$) [24]. The generator-level dimuon invariant mass and transverse momentum distributions under these variations are shown in Figures 8.1 and 8.2, respectively.

No statistically significant shape differences in the invariant mass and dimuon transverse momentum is observed between the nominal and varied setup. The relative acceptance difference ΔA for the scale variations is summarised in Table 8.7.

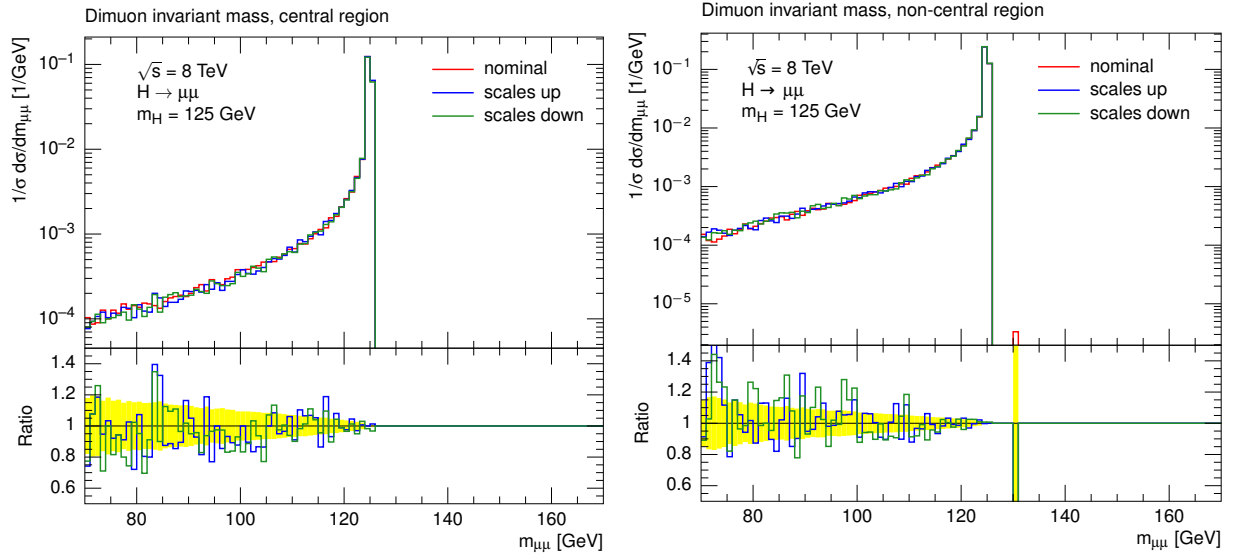


Figure 8.1: Generator-level dimuon invariant distribution for central (left) and non-central (right) events under scale variations. The nominal distribution is shown in red, the blue line indicates the shape when μ_R and μ_F are scaled up, and the green line depicts the distribution when both scales are scaled down. The ratio plot underneath further shows the statistical uncertainty of the nominal distribution as a yellow band.

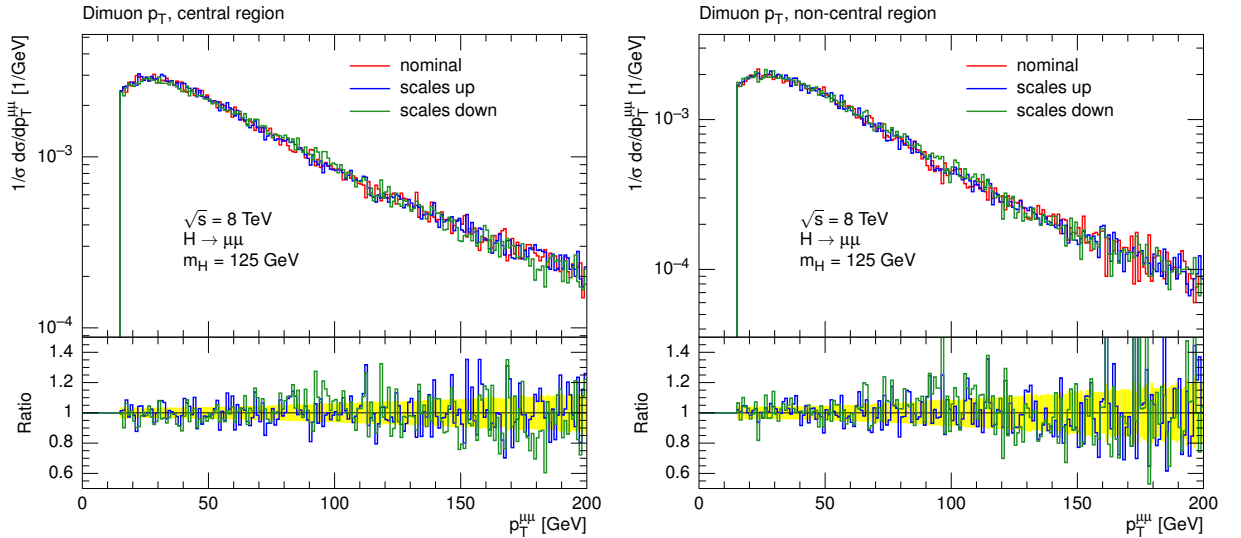


Figure 8.2: Generator-level dimuon transverse momentum distribution for central (left) and non-central (right) events under scale variations. The nominal distribution is shown in red, the blue line indicates the shape when μ_R and μ_F are scaled up, and the green line depicts the distribution when both scales are scaled down. The ratio plot underneath further shows the statistical uncertainty of the nominal distribution as a yellow band.

category	ΔA [%]
central	1.05 ± 0.37
non-central	0.25 ± 0.05

Table 8.8: Relative acceptance deviation in percent originating from PDF uncertainties obtained via a Gaussian fit of the deviation distribution. The statistical uncertainty of ΔA is also given.

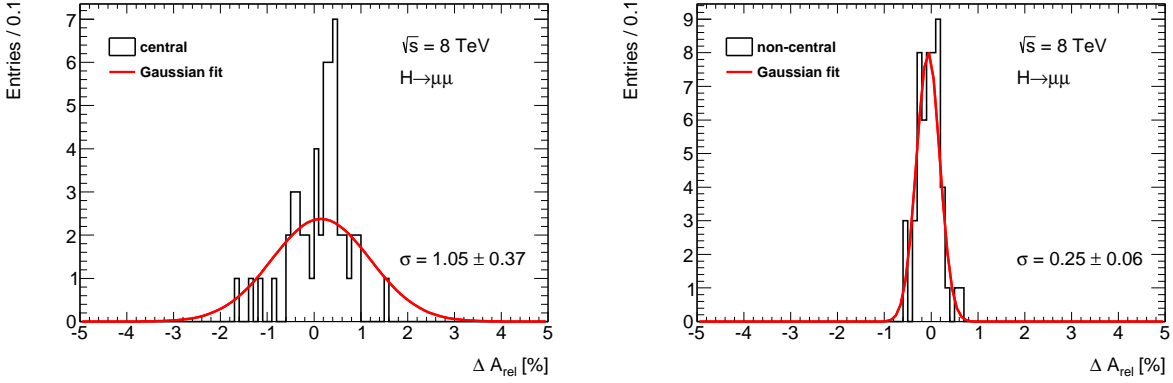


Figure 8.3: Acceptance deviation distribution obtained using each of the 52 error PDFs in the CT10nlo PDF set in the generation for the central (left) and non-central (right) resolution category. The Gaussian fit to the distribution and the respective fit parameters are also displayed.

Parton Distribution Function Uncertainties The parton distribution function used to simulate the $H \rightarrow \mu\mu$ sample is the CT10nlo [107] PDF. This PDF set is based on 26 eigenvectors which span up the function. Each of these eigenvectors has an uncertainty resulting from the fits used to obtain them, and thus the whole PDF set contains in total 52 error PDFs, two for each eigenvector. In these error PDFs, one eigenvector is varied up and down within its 90% CL uncertainty [46]. The effects of these PDF uncertainties are studied in terms of the acceptance systematics by using each of the error PDFs as input for the event generation, and compare the relative acceptance deviation ΔA from the nominal PDF. When this deviation is plotted and fitted with a Gaussian distribution, the standard deviation of the Gaussian distribution directly corresponds to the acceptance systematic uncertainty caused by the PDF uncertainty: since each eigenvector variation is independent from all others, the total acceptance uncertainty is the square root of the sum of each individual deviation, divided by the number of acceptances entering the sum minus 1. This is the definition of the standard deviation of the acceptance difference histogram, which is approximated by the standard deviation of its Gaussian fit. Table 8.8 summarises the obtained systematic uncertainties, and the distribution of ΔA for the PDF variation is shown in Figure 8.3.

resolution category	ΔA , ISR up [%]	ΔA , ISR down [%]	ΔA , FSR up [%]	ΔA , FSR down [%]
central	2.5 ± 0.5	-3.4 ± 0.5	-0.3 ± 0.5	0.1 ± 0.5
non-central	0.8 ± 0.3	-2.0 ± 0.3	-0.4 ± 0.3	0.1 ± 0.3

Table 8.9: Relative acceptance deviations in percent obtained by varying the ISR and FSR emission probability. The statistical uncertainty of the deviations is also given.

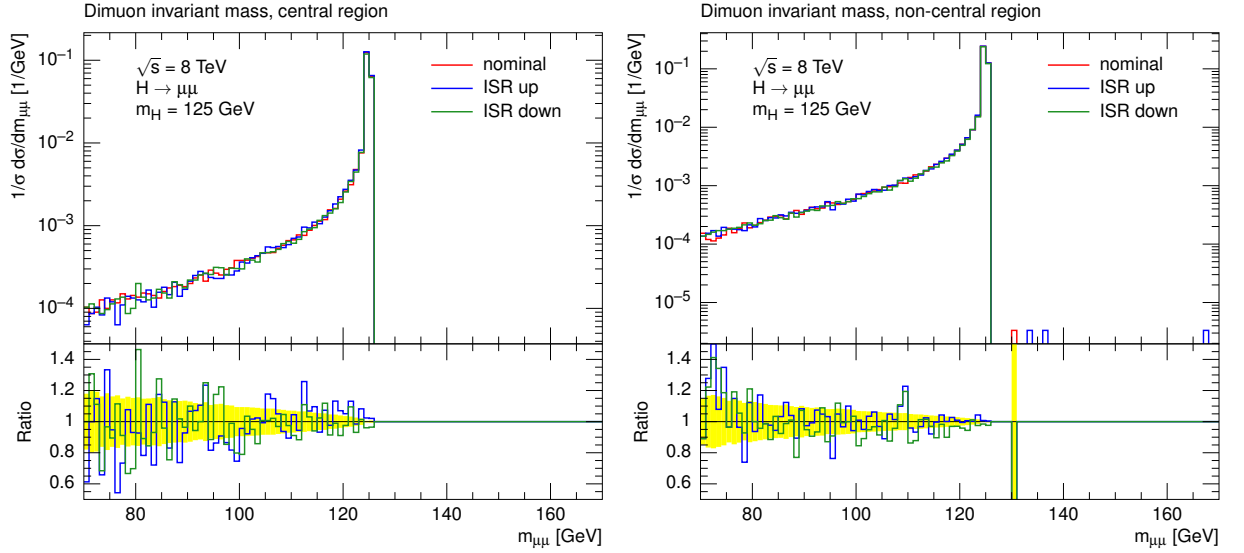


Figure 8.4: Generator-level dimuon invariant mass distribution for central (left) and non-central (right) events with varied ISR probability. The nominal distribution is shown in red, the blue line indicates the shape when α_S is scaled up, and the green line depicts the distribution when ISR is scaled down. The ratio plot underneath further shows the statistical uncertainty of the nominal distribution as a yellow band.

Initial and Final State Radiation The modeling of initial and final state radiation (ISR and FSR) involves many parameters depending on the shower generator (see section 4.1.3). ISR and FSR are one of the main tuning areas for MC event generators, and measurements from collision data is continuously used to tune the ISR and FSR shower simulation [108]. A simple yet conservative way to estimate the systematic uncertainties arising from ISR and FSR shower modeling is to scale the involved couplings, such that the probability of emissions is increased or decreased. This is done for the standalone analysis separately for ISR and FSR, since the former only involves QCD vertices in the investigated gluon-gluon fusion production process, while the latter contains both QCD and QED emissions. Thus, for the ISR uncertainty estimation, the strong coupling constant α_S used by the PYTHIA8 shower generator is scaled up and down by $\pm 20\%$, whereas the FSR uncertainty is estimated by scaling α_S by $\pm 20\%$ and α_{EM} by $\pm 5\%$. The values are chosen because QED showers are much better understood theoretically [109] and thus less subject to uncertainties. QCD shower evolution, on the other hand, is far more complicated, and a 20% scaling is needed to engulf all involved uncertainties [110]. The relative acceptance uncertainties obtained with these variations are summarised in Table 8.9. The dimuon invariant mass and transverse momentum distributions with varied ISR probability after the analysis selection are shown in figures 8.4 and 8.5. It can be observed that the invariant mass shape is not affected by the variation, but the $p_T^{\mu\mu}$ distributions differ from the nominal one. This is expected, as emissions in the initial state affect the p_T balance of the dimuon system, so more (less) emissions lead to a higher (lower) dimuon transverse momentum, respectively. This is also the driving force behind the large acceptance differences for ISR variations, since events migrate between the signal and control regions. The picture is different for final

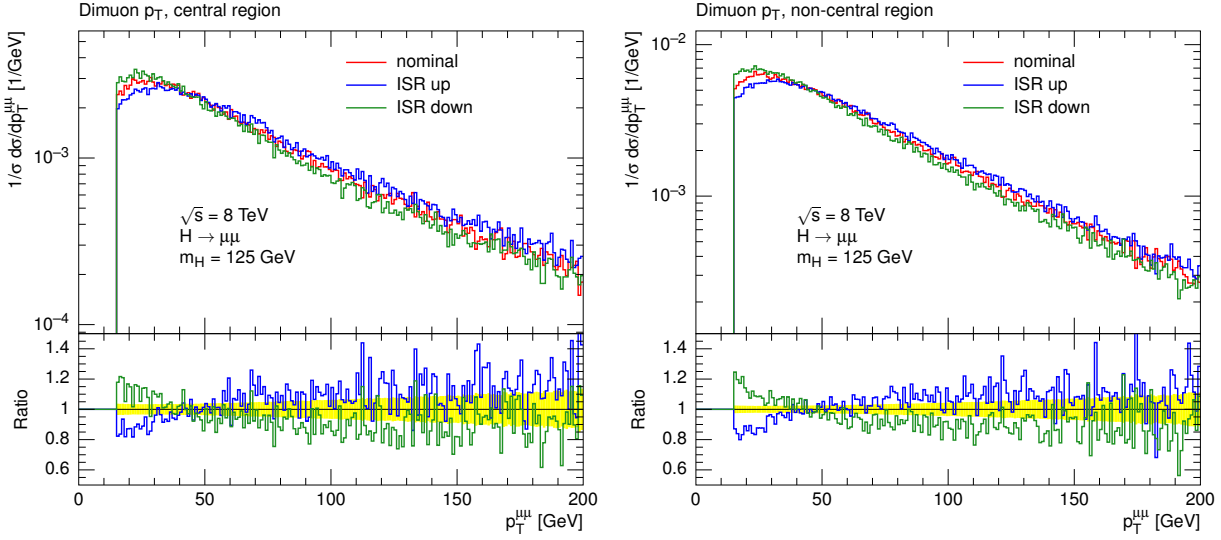


Figure 8.5: Generator-level dimuon transverse momentum distribution for central (left) and non-central (right) events with varied ISR probability. The nominal distribution is shown in red, the blue line indicates the shape when α_S is scaled up, and the green line depicts the distribution when ISR is scaled down. The ratio plot underneath further shows the statistical uncertainty of the nominal distribution as a yellow band.

state radiation variation, as can be observed in figures 8.6 and 8.7. QCD emissions driven by α_S do not affect the dimuon system, so no significant deviations from the nominal distribution in $p_T^{\mu\mu}$ are seen. The scaling of α_{EM} in principle affects the dimuon kinematics, but since the probability of emissions from muons is low, and the uncertainty of the QED FSR shower is small (reflected by the small scaling of α_{EM} of $\pm 5\%$), the overall effect of the FSR uncertainty on the signal acceptance is very small.

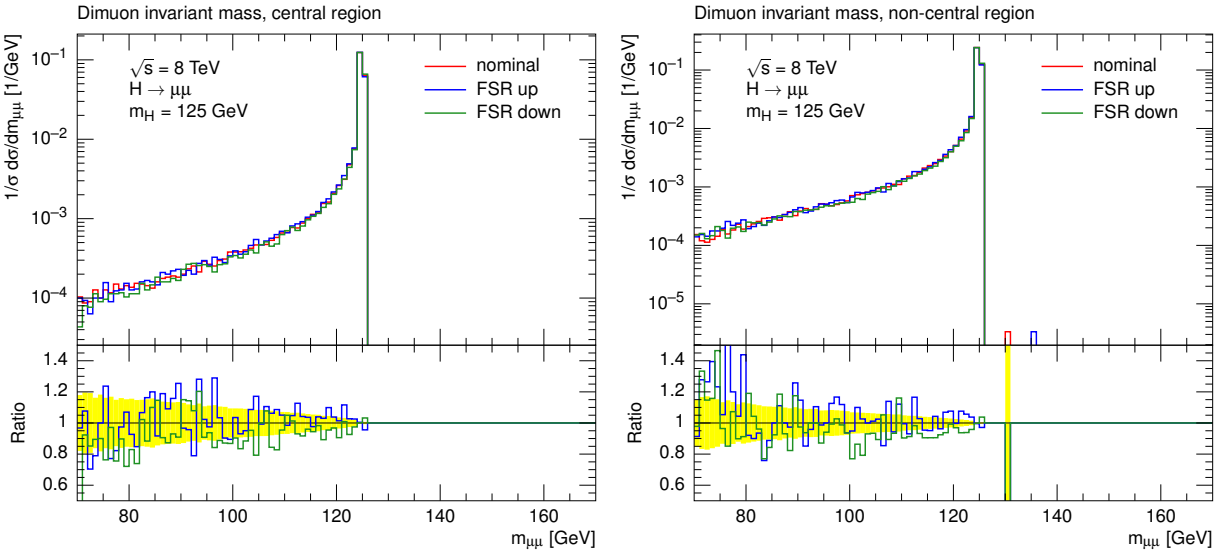


Figure 8.6: Generator-level dimuon invariant mass distribution for central (left) and non-central (right) events with varied FSR probability. The nominal distribution is shown in red, the blue line indicates the shape when α_S and α_{EM} are scaled up, and the green line depicts the distribution when FSR is scaled down. The ratio plot underneath further shows the statistical uncertainty of the nominal distribution as a yellow band.

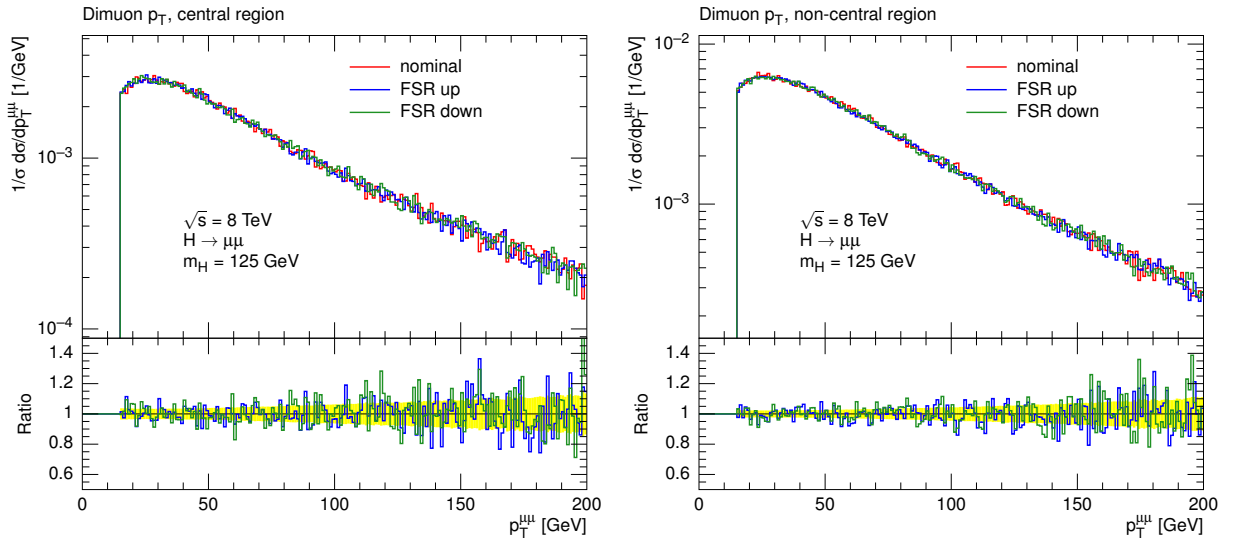


Figure 8.7: Generator-level dimuon transverse momentum distribution for central (left) and non-central (right) events with varied FSR probability. The nominal distribution is shown in red, the blue line indicates the shape when α_S and α_{EM} are scaled up, and the green line depicts the distribution when FSR is scaled down. The ratio plot underneath further shows the statistical uncertainty of the nominal distribution as a yellow band.

category	+ ΔA [%]	- ΔA [%]
central	2.7	-4.1
non-central	1.0	-2.0

Table 8.10: Total signal acceptance systematic uncertainty in percent of the standalone analysis, obtained combining all individual contributions. The middle column is the quadratic sum of all positive deviations, and the right column combines all negative contributions, thus asymmetric uncertainties are formed.

Summary of Standalone Signal Acceptance Systematic Uncertainties Since each of the investigated systematic uncertainties is considered uncorrelated, the total acceptance uncertainty is obtained by adding each individual contribution in quadrature. Hereby, deviations with the same sign are grouped together, and deviations smaller than their statistical uncertainty are omitted from the calculation. The combined signal acceptance systematic uncertainties for the two resolution categories are summarised in Table 8.10.

8.3.1.2 Acceptance Uncertainties of the Combined Analysis In the combined analysis, acceptance systematic uncertainties are treated according to recommendations by the LHC Higgs cross section group [102], which were not available for the standalone analysis. These recommendations cover uncertainties in the Higgs boson transverse momentum prediction, uncertainties of the gluon-fusion contribution to the VBF selection event yield due to missing higher order terms in the differential cross-section calculation, and uncertainties in the modeling of multiple parton interactions. These are presented in following paragraphs. Improvements in the ISR and FSR shower tuning [69] for the signal MC simulated samples used in the combined analysis made a dedicated investigation of ISR and FSR modeling uncertainties obsolete.

Uncertainties of the Higgs Boson Transverse Momentum In the combined analysis, the Higgs boson transverse momentum spectra in the simulated signal samples are reweighted to obtain the NNLO differential p_T distribution. The uncertainty of the reweighting factors is therefore caused by the uncertainty of the NNLO differential cross section determination. This includes uncertainties due to missing higher order terms, again absorbed in the renormalisation and factorisation scale variations, PDF+ α_S uncertainties, and additional uncertainties due to non-perturbative QCD effects [27]. The impact of the Higgs p_T reweighting uncertainty on the combined analysis is evaluated for a Higgs boson mass of 125 GeV by varying the reweighting factors within their uncertainty and comparing the event yield in each category. The reweighted of the Higgs boson p_T spectra are shown in Figure 8.8 for a Higgs boson mass of 125 GeV. The resulting systematic uncertainties range from 0.3 % in the low transverse momentum categories to 4.9 % in the high transverse momentum central category [93], and are summarised in Table 8.11.

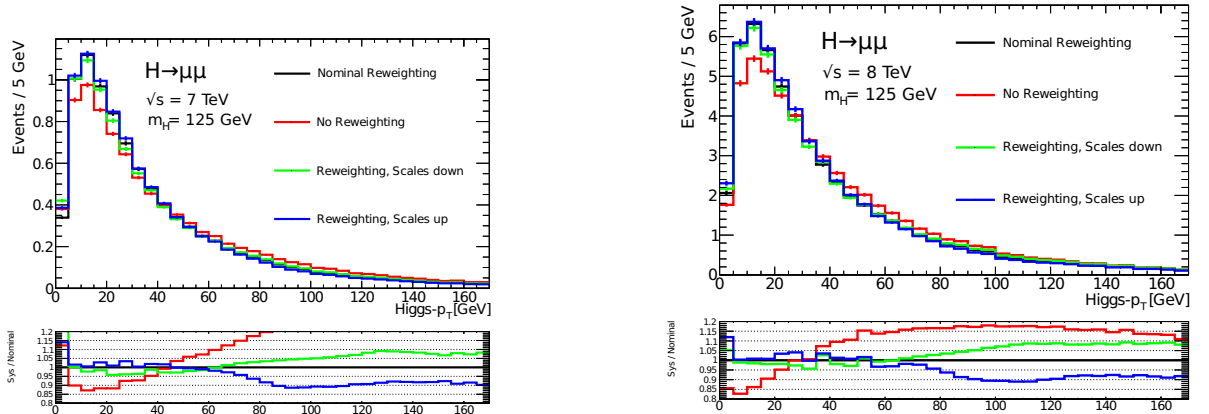


Figure 8.8: Higgs boson p_T spectra after applying the invariant mass window of $105 \text{ GeV} < m_{\mu\mu} < 160 \text{ GeV}$ for a centre-of-mass energy of $\sqrt{s} = 7 \text{ TeV}$ (left) and 8 TeV (right). The black line shows the nominal reweighted spectrum, and the blue and green lines depict the reweighted spectra with the factors varied within their uncertainties. For comparison, the unweighted spectrum is shown in red. [93]

analysis category	7 TeV [%]	8 TeV [%]
Low $p_T^{\mu\mu}$ central	0.3	1.3
Low $p_T^{\mu\mu}$ non-central	0.3	1.3
Medium $p_T^{\mu\mu}$ central	2.3	1.9
Medium $p_T^{\mu\mu}$ non-central	2.3	1.9
High $p_T^{\mu\mu}$ central	-4.8	-4.9
High $p_T^{\mu\mu}$ non-central	-4.4	-4.5
VBF	-1.3	-1.7

Table 8.11: Systematic uncertainties in each analysis category arising from uncertainties in the Higgs boson transverse momentum distribution, obtained for a Higgs boson mass of 125 GeV [93].

Higgs boson production process	MPI uncertainty [%]
gluon-fusion	8.5
vector-boson-fusion	4.0

Table 8.12: Systematic uncertainty of the signal event yield in the VBF selection category of the combined analysis due to multi-parton interaction, shown separately for the gluon-fusion and vector-boson-fusion Higgs boson production mechanisms.

Uncertainties from Missing Higher Order Corrections In the combined analysis, the signal yield in the VBF category (see section 6.3.3) is not only due to VBF events, but to a non-negligible extend also caused by gluon-fusion events with two additional jets. Since the gluon-fusion Higgs boson production matrix element is generated with the POWHEG NLO generator, only the hardest additional QCD emission is expected to be modeled correctly, and the yield of two-jet signature events is subject to theoretical uncertainties due to missing higher order terms in the matrix element calculation. These uncertainties are estimated by varying the renormalisation and factorisation scales μ_F and μ_R , but in particular for the VBF selection phase space, where the induced uncertainties are expected to be higher. A detailed description of this method is given in [102]. For the combined analysis, the relative systematic uncertainty on the gluon-fusion signal event yield in the VBF selection category is 21.7% [93].

Multi-Parton Interaction Uncertainty The multi-parton interaction (MPI) affects the hadronic activity in the event and thus the jet kinematics. Thus, uncertainties of the MPI are expected in the VBF selection category of the combined analysis. The uncertainty is estimated in a conservative way by switching the MPI on and off in the event generation for both gluon-fusion and vector-boson fusion events, and compare the event yield in the VBF selection category, following the recommendations of [102]. The relative systematic uncertainties in the signal event yield in the VBF selection category are summarised in table 8.12. The gluon-fusion induced signal events are more influenced by MPI, since only the hardest emission is simulated by the matrix element. Thus, the second leading jet tends to be softer than in the vector-boson fusion events, and the additional hadronic activity of the MPI contributes a more significant portion to its momentum.

8.3.2 Spurious Signal Method

Since the total expected background is modeled with an analytical function whose normalization and shape parameters are completely determined from the fit to the invariant dimuon mass spectrum observed in data, there are no direct systematic uncertainties arising from the usage of Monte Carlo simulated datasets. However, the background model in itself might be inadequate to correctly follow the shape of the expected background. This might cause so-called spurious signal, where this background mismodeling is compensated by the signal model giving rise to additional unwanted pseudo signal. This section will introduce the spurious signal technique and elaborate on how the spurious signal is determined in this analysis.

8.3.2.1 Spurious Signal in a Nutshell The spurious signal method is a way to address and quantify a systematic uncertainty to the choice of a particular background model. The basic idea is that in the limit of an infinite number of pure background events, meaning zero statistical uncertainty of the investigated spectrum, the residual discrepancies between the spectrum and the model are no longer statistically dominated, but caused by the background model itself. The combined signal plus background fit will then 'fill up' these discrepancies with the signal model causing spurious signal, as illustrated in Figure 8.9. The spurious signal is thus quantified in the spurious signal strength μ_{SP} in the combined signal plus

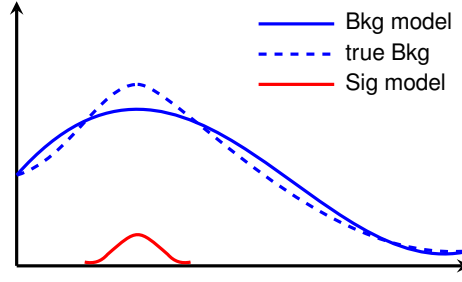


Figure 8.9: Schematic view of the spurious signal effect. The true background spectrum in dashed blue is fitted with an inadequate background model in solid blue, which leaves room for the signal model to fill up the discrepancy (red) although no signal is present.

sample	mass range [GeV]	number of events	σ [pb]
low mass	60 - 100	103,776,477	1064.82
high mass	100 - 200	156,223,214	43.4665

Table 8.13: Properties of the generator-level samples utilised in the spurious signal method.

background fit applied to the background only spectrum:

$$f_{\text{combined}} = f_{\text{BKG}} + \mu_{\text{SP}} \cdot f_{\text{sig}}. \quad (8.3)$$

Here, f_{bkg} describes the respective background function for the combined analysis as introduced in section 7.2.2, and f_{sig} denotes the signal shape parametrisation described in section 7.1. The signal shape parameters are hereby fixed to their expected values from fits to MC simulated signal samples for each tested mass point, similarly to the final limit setting procedure. Only the background model parameters and the spurious signal strength μ_{SP} are allowed to float freely in the fit. The spurious signal is determined by these fits for a centre-of-mass energy of 8 TeV only, the results are extrapolated for the 7 TeV dataset using luminosity and background cross-section scaling.

8.3.2.2 Generator-Level Smeared Background Samples As described earlier, the spurious signal technique is valid only in the limit of infinite statistics, implying no statistical fluctuations in the tested background spectrum. For the presented analysis, a new procedure was developed to produce simulated background spectra with very small statistical fluctuations. However, it is technically extremely challenging and very CPU-intensive to produce MC simulated background samples in a sufficient amount to justify the application of the spurious signal method. The available Z/γ^* dimuon background MC samples with full detector simulation correspond to an integrated luminosity of $\mathcal{L} \approx 800 \text{ fb}^{-1}$, which is not sufficient. However, the detector response to muons can be approximated by a fairly simple resolution model. That way, it is possible to mimic the reconstructed dimuon mass spectrum by applying the resolution model to the generator-level four-momentum vectors of the simulated muons, without the need to simulate the complete detector response. These generator-level samples can be produced in large quantities with only a fraction of the CPU time needed to simulated the detector response. For this analysis, two generator-level dimuon datasets at a centre-of-mass energy of 8 TeV were produced, which are summarised in Table 8.13. Together, these correspond to an integrated luminosity of $\mathcal{L} \approx 3600 \text{ fb}^{-1}$.

Simplified Muon Resolution Model The simplified muon resolution model is based on the relative transverse momentum difference $\Delta p_{\text{T}}^{\text{rel}}$ between the generated (*truth*) muon and the reconstructed (*reco*)

muon, defined as:

$$\Delta p_T^{rel} = \frac{p_T^{truth} - p_T^{reco}}{p_T^{truth}}. \quad (8.4)$$

This quantity is derived from the fully simulated POWHEG inclusive $Z/\gamma^* \rightarrow \mu\mu$ sample. In order to have a sufficiently large dataset to reduce statistical uncertainties of the resolution, only minimal selection steps are applied:

- 1: select truth muons originating from the hard process, after FSR corrections are applied
- 2: select reconstructed muons as described in section 6.2.1.1
- 3: geometric match between reconstructed and truth muons within a cone $\Delta R < 0.01$

Table 8.14 summarises the event yield of this selection.

Selection Step	Number of events
All events	30,000,000
Truth muon selection	21,122,300
Truth match	20,080,710

Table 8.14: Event yields of the resolution selection derived from the inclusive POWHEG sample.

As a resolution model, the sum of two Gaussian distributions was chosen, based on the observation that one single Gaussian distribution cannot account for the tails in the Δp_T^{rel} spectra. The exact functional form is:

$$F(\Delta p_T^{rel}) = A \left(f \cdot e^{-0.5 \left(\frac{\Delta p_T^{rel} - \mu_{CG}}{\sigma_{CG}} \right)^2} + (1 - f) \cdot e^{-0.5 \left(\frac{\Delta p_T^{rel} - \mu_{OG}}{\sigma_{OG}} \right)^2} \right), \quad (8.5)$$

where A corresponds to the overall normalisation and f denotes the fraction between the central Gauss (CG) and outer Gauss (OG). The expectation values of the two Gaussian distributions are expressed by the parameters μ_{CG} and μ_{OG} , and the widths are called σ_{CG} and σ_{OG} , respectively.

Since the detector resolution for muons depends on p_T and η , and on the charge of the muon (c.f. section 5), the resolution model parameters are obtained by fitting the Δp_T^{rel} distribution in bins of p_T^{truth} and η^{truth} , separately for positive and negative truth muons. The bins in p_T and η have been chosen based on the detector design, taking the central crack region and barrel-endcap muon spectrometer transition region into account. The fit results of the central gaussian width σ_{OG} is shown in Figure 8.10, the results for the other parameters are collected in appendix C. The widths σ_{CG}, σ_{OG} hereby follow the expectation from the detector performance, where the resolution is getting worse for high transverse momenta and in the endcap region above $\eta \approx 1.0$.

The obtained resolution model parameters are then used to “smear” the transverse momenta of generator-level muons in order to reproduce the reconstructed dimuon invariant mass spectrum. The “smeared” transverse momentum p_T^S is obtained as follows:

$$p_T^S = p_T^{truth} \cdot (\Delta p_T^{rel} + 1) \quad (8.6)$$

$$= p_T^{truth} \cdot \left(\underbrace{f \cdot e^{-0.5 \left(\frac{x - \mu_{CG}}{\sigma_{CG}} \right)^2} + (1 - f) \cdot e^{-0.5 \left(\frac{x - \mu_{OG}}{\sigma_{OG}} \right)^2}}_{p.d.f} - 1 \right), \quad (8.7)$$

where Δp_T^{rel} is now treated as a random variable distributed according to the functional form denoted by $p.d.f$. Hence, for each generated muon a random number is drawn from $p.d.f$, setting its parameters $f, \mu_{CG}, \mu_{OG}, \sigma_{CG}$ and σ_{OG} to the values corresponding to the p_T and η of the respective muon.

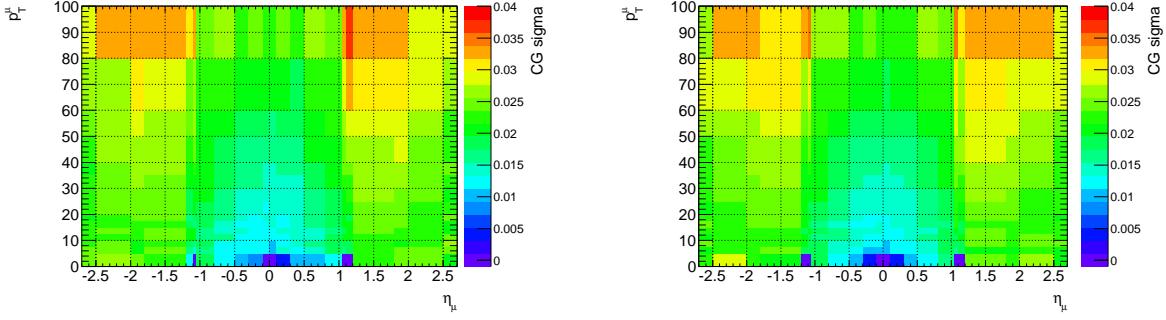


Figure 8.10: Parameter distribution of the central Gauss (CG) width parameter σ_{CG} after fitting to the Δp_T^{rel} distributions, binned in η^{truth} and p_T^{truth} . The left plot shows the distribution for anti-muons, and the values obtained for muons are displayed on the right.

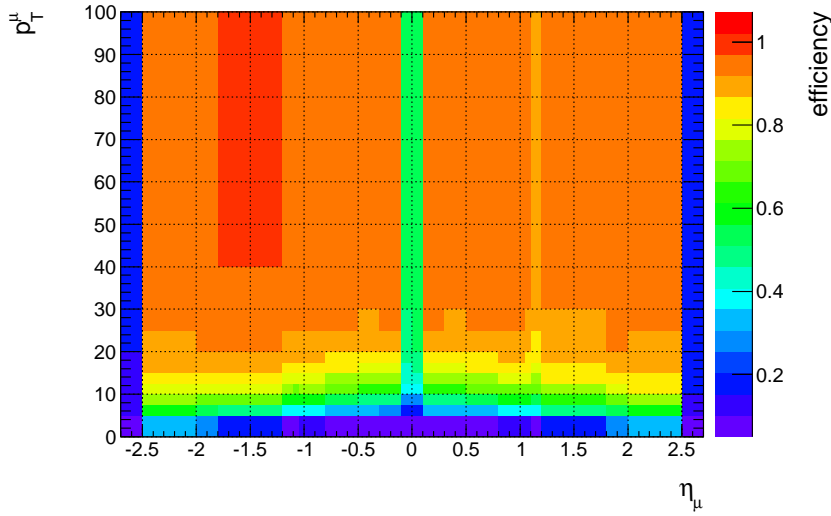


Figure 8.11: Reconstruction and identification efficiency as a function of η and p_T of the generated muon.

Reconstruction Efficiency Effects The reconstruction efficiency for muons is not uniform in η and p_T , as pointed out in section 5.5.1. Since this affects the shape of kinematic distributions, the reconstruction efficiency ϵ has to be taken into account when using smeared generator-level muons. This is done by assigning a weight to each generated muon, which is equal to its probability of being reconstructed and identified as described in section 6.2.1.1. This probability can be identified with the reconstruction efficiency:

$$\epsilon = \frac{N_{\text{reco,TM}}(p_T, \eta)}{N_{\text{truth}}(p_T, \eta)}. \quad (8.8)$$

Hereby, $N_{\text{reco,TM}}$ refers to the number of reconstructed muons with a match to a generated truth muon, and N_{truth} denotes the total number of generated truth muons, both numbers are binned in p_T and η . The reconstruction and identification probability was derived on the same fully simulated Powheg dimuon sample as used for the resolution. Figure 8.11 shows the dependence of ϵ on η and p_T . The expected drops in ϵ around the central crack region near $\eta = 0$, in the transition region of $|\eta| \approx 1$ and at the boundary of the inner detector at $|\eta| > 2.5$ are visible. The reconstruction efficiency increases with rising transverse momentum as expected (c.f. section 5.5.1).

Validation of the Smearing Procedure The final step involves applying the smearing procedure and the reconstruction efficiency weights to the generator-level samples. Then these samples are used

similarly to the regular simulated samples, meaning the combined analysis selection and categorisation is applied (see section 6.3.3), the samples are normalised to the data luminosity and the non-Drell-Yan background components are added. Since the generator-level samples do not contain any information about jets, the VBF category has to be omitted. The method of smearing generator-level events is only valid if the dimuon invariant mass distribution of the smeared muons is in agreement with the one from reconstructed muons. This consistency check was done using the fully simulated PowHEG dimuon samples, where both generator-level truth muons and reconstructed muons are available. The event selection and categorisation is hereby done in parallel for both reconstructed muons and smeared truth muons, and the dimuon invariant mass spectra are compared. The resulting spectra are shown in Figures 8.12-8.14.

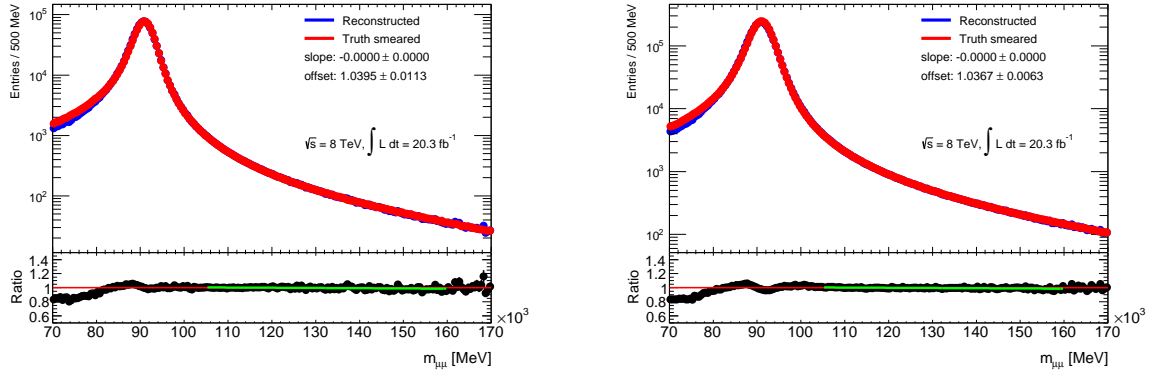


Figure 8.12: Comparison of the reconstructed and smeared dimuon invariant mass spectra of the low $p_T^{\mu\mu}$ category for central (left) and non-central (right) events, obtained using the fully simulated PowHEG samples. The reconstructed spectrum is shown in blue, and the smeared truth spectrum is marked with red points. The black points below show indicate the ratio between the reconstructed and truth spectrum, and a linear fit to this ratio in the range between 105 and 160 GeV is shown in green, with the fit parameters displayed in the main canvas.

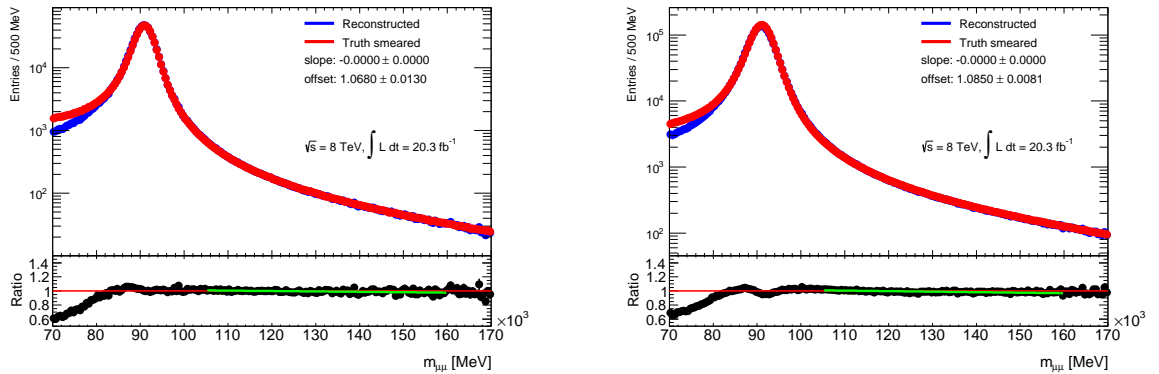


Figure 8.13: Comparison of the reconstructed and smeared dimuon invariant mass spectra of the medium $p_T^{\mu\mu}$ category for central (left) and non-central (right) events, obtained using the fully simulated PowHEG samples. The reconstructed spectrum is shown in blue, and the smeared truth spectrum is marked with red points. The black points below show indicate the ratio between the reconstructed and truth spectrum, and a linear fit to this ratio in the range between 105 and 160 GeV is shown in green, with the fit parameters displayed in the main canvas.

It is observed that the reconstructed and smeared truth spectra do not agree very well in the low in-

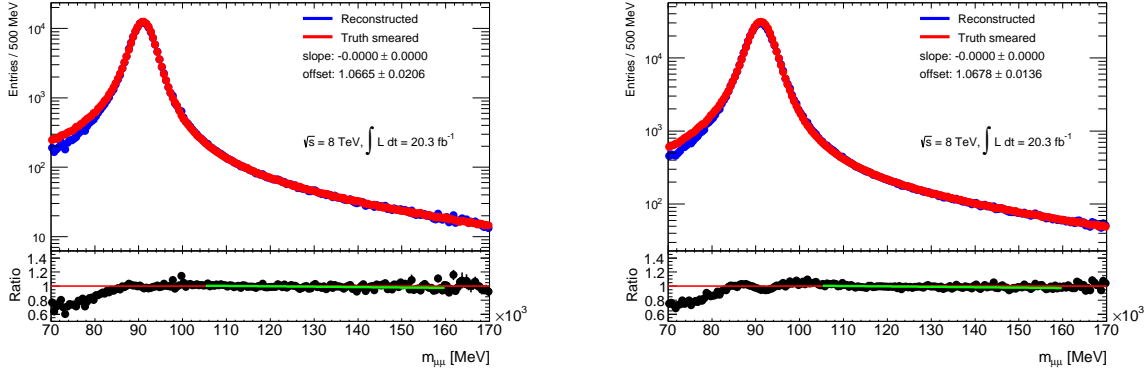


Figure 8.14: Comparison of the reconstructed and smeared dimuon invariant mass spectra of the high $p_T^{\mu\mu}$ category for central (left) and non-central (right) events, obtained using the fully simulated POWHEG samples. The reconstructed spectrum is shown in blue, and the smeared truth spectrum is marked with red points. The black points below show indicate the ratio between the reconstructed and truth spectrum, and a linear fit to this ratio in the range between 105 and 160 GeV is shown in green, with the fit parameters displayed in the main canvas.

variant mass region, below approximately 90 GeV. This is expected to some extent, because the applied simple resolution model cannot compensate for all detector effects, which are especially complicated and subtle at the mass of the Z -boson resonance and below [77]. Albeit, as the linear fit to the ratio between the reconstructed and truth spectrum shows, the two distributions agree remarkably well within the region of interest of the combined data analysis.

8.3.2.3 Spurious Signal Results The spurious signal fits are performed differentially in the invariant mass according to Equation 8.3. For the dimuon transverse momentum categories, the aforementioned smeared generator-level samples with added non-Drell-Yan background components are used, whereas for the VBF category only fully simulated 8 TeV POWHEG samples are utilised. The spectra are all normalised to the luminosity of the 2012 dataset. Further, the amount of spurious signal is compared to the expected statistical error on the signal strength μ , assuming the luminosity in data. This value, $\mu_{SP}/\sigma^{exp}(\mu)$, is a measure of how precisely the spurious signal is determined. Previous analyses, including the observation of the Higgs boson in the diphoton final state, aimed for a $\mu_{SP}/\sigma^{exp}(\mu)$ of less than 0.2 [111]. The usage of very high statistics generator-level samples however enables an actual measurement of the differential spurious signal with a much higher precision of $\mu_{SP}/\sigma^{exp}(\mu) \simeq 0.01$.

Since a differential spurious signal term would include too many parameters in the limit setting and would thus destabilise the fit, the amount of spurious signal is averaged over the whole mass range of 120 GeV–150 GeV. The RMS of the differential distribution is chosen, which is a good compromise between the maximum (too conservative) and the mean (too optimistic). The results of the differential spurious signal fits in the dimuon transverse momentum categories are shown in Figures 8.15 - 8.17. The spurious signal distribution in the VBF category is depicted in Figure 8.18. It can be seen that the low $p_T^{\mu\mu}$ non-central category exhibits relatively large spurious signal. Nevertheless, the advantages of the background model in terms of simplicity and flexibility to describe varying background compositions in the analysis categories outweigh this apparent shortcoming by far. The amount of spurious signal in each category is summarised in Table 8.15. The values for 8 TeV are obtained from the aforementioned fits, and the 7 TeV results are extrapolated using luminosity and cross-section scaling.

category	spurious signal	
	7 TeV	8 TeV
low $p_T^{\mu\mu}$ central	1.6	7.9
low $p_T^{\mu\mu}$ non-central	4.4	23.3
medium $p_T^{\mu\mu}$ central	0.2	1.3
medium $p_T^{\mu\mu}$ non-central	0.8	4.6
high $p_T^{\mu\mu}$ central	0.2	1.1
high $p_T^{\mu\mu}$ non-central	0.5	2.8
VBF	0.3	1.6

Table 8.15: Averaged spurious signal events in each of the analysis categories, for both 7 and 8 TeV centre-of-mass energies. The 7 TeV results are obtained by scaling the 8 TeV values according to the ratios of cross-section and integrated luminosity.

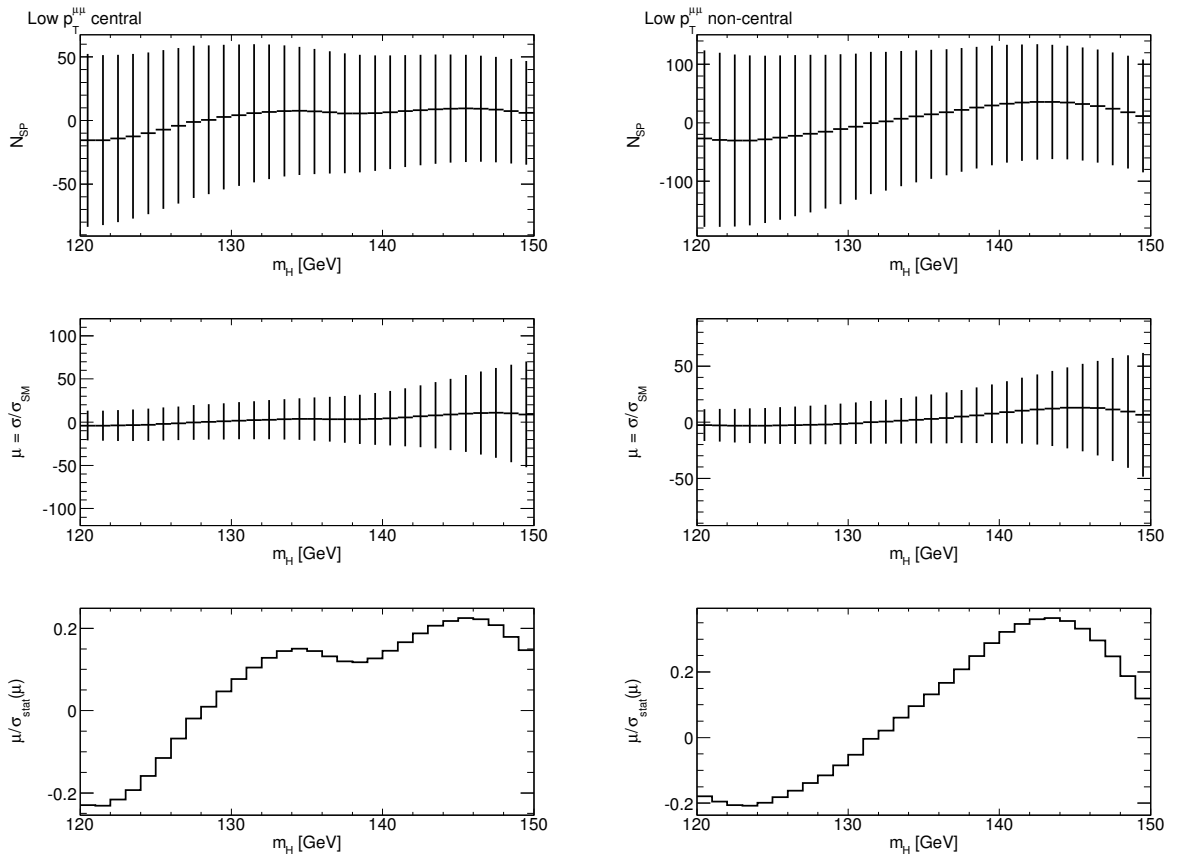


Figure 8.15: Results of the spurious signal fit in the low $p_T^{\mu\mu}$ category for central (left) and non-central (right) events. The top plots show the fitted number of spurious signal events, the distributions in the middle row depict the spurious signal strength μ_{SP} and the bottom histograms exhibit the distribution of $\mu_{SP}/\sigma^{exp}(\mu)$. The uncertainty bars of the upper two plots indicate the expected statistical uncertainty assuming the luminosity in data.

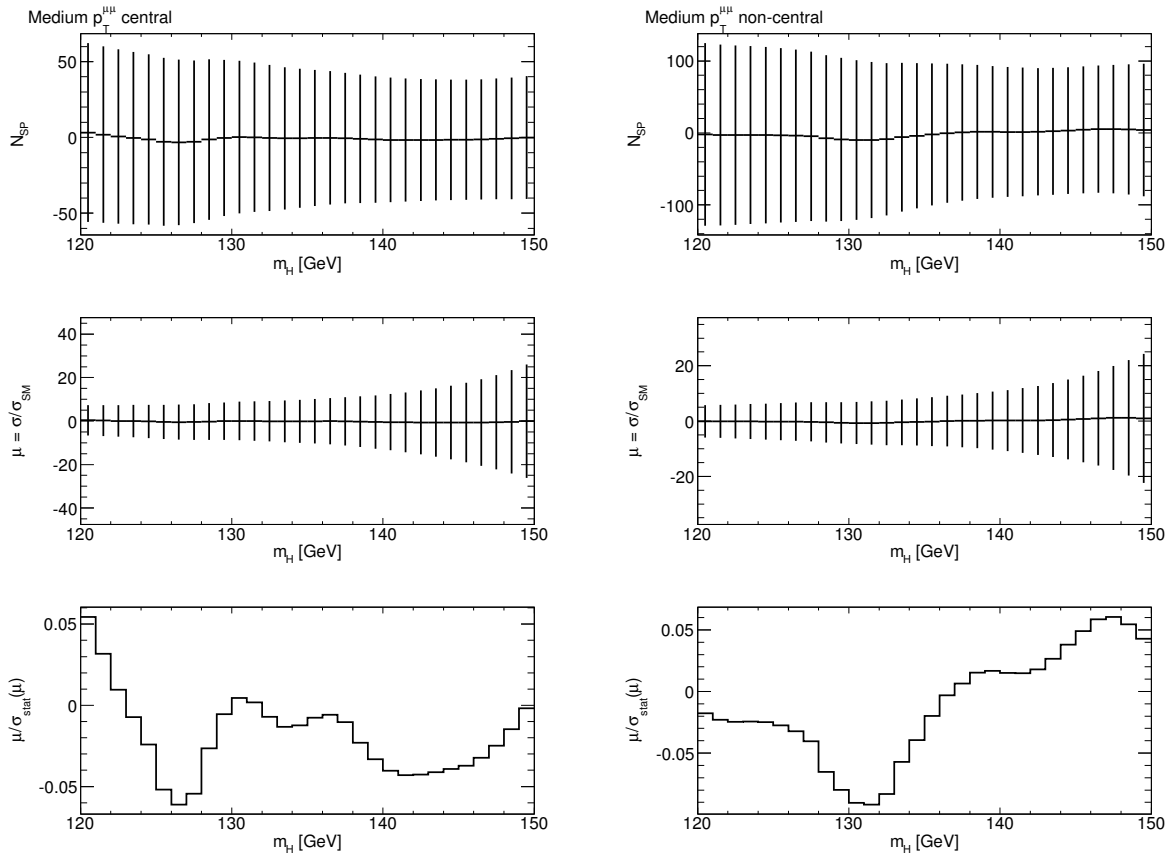


Figure 8.16: Results of the spurious signal fit in the medium $p_T^{\mu\mu}$ category for central (left) and non-central (right) events. The top plots show the fitted number of spurious signal events, the distributions in the middle row depict the spurious signal strength μ_{SP} and the bottom histograms exhibit the distribution of $\mu_{SP}/\sigma^{exp}(\mu)$. The uncertainty bars of the upper plots indicate the expected statistical uncertainty assuming the luminosity in data.

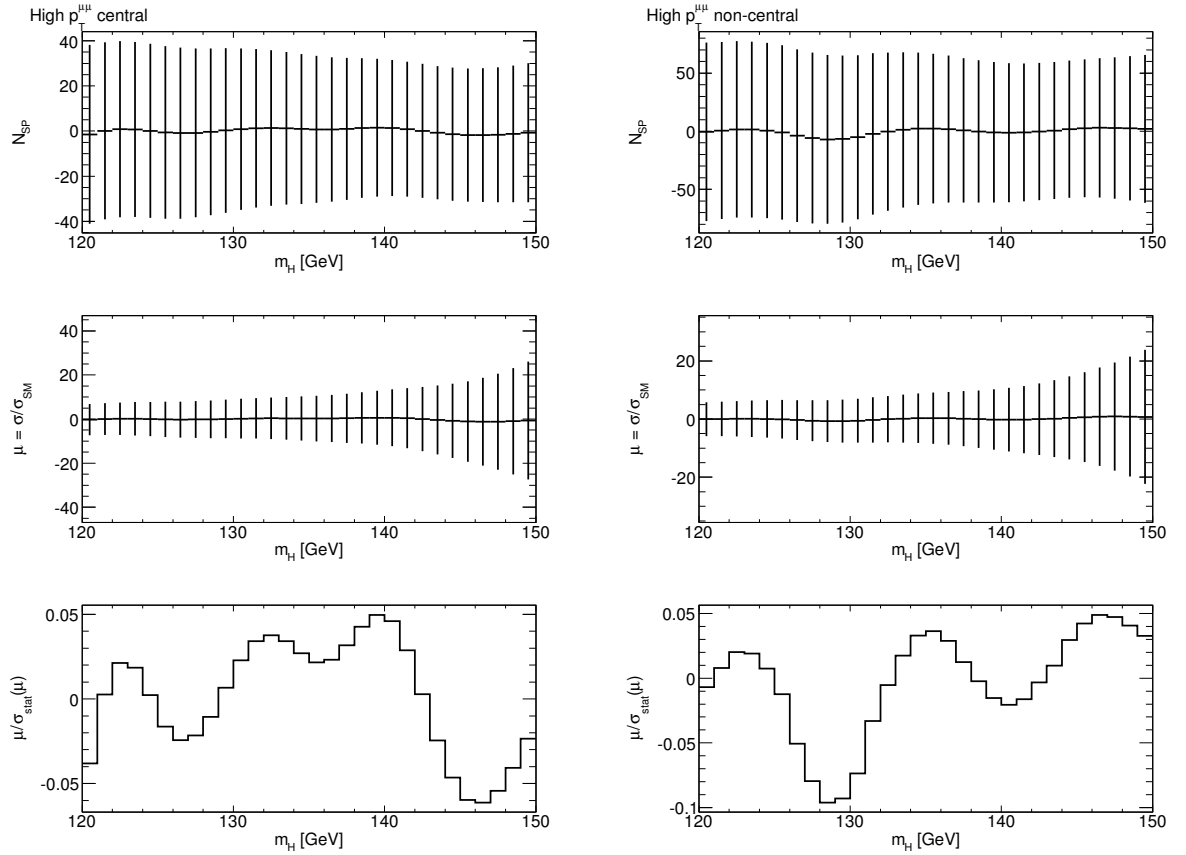


Figure 8.17: Results of the spurious signal fit in the high $p_T^{\mu\mu}$ category for central (left) and non-central (right) events. The top plots show the fitted number of spurious signal events, the distributions in the middle row depict the spurious signal strength μ_{SP} and the bottom histograms exhibit the distribution of $\mu_{SP}/\sigma^{exp}(\mu)$. The uncertainty bars of the upper plots indicate the expected statistical uncertainty assuming the luminosity in data.

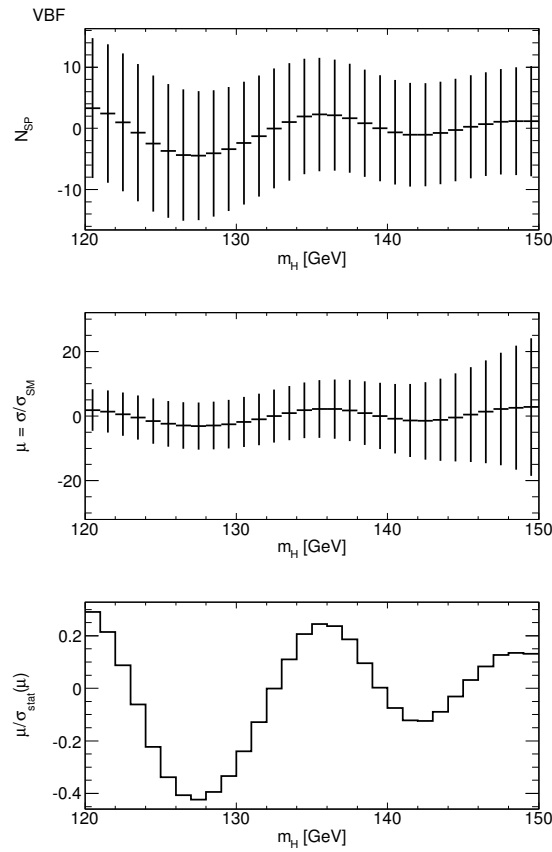


Figure 8.18: Result of the spurious signal fit in the VBF category. The top plot show the fitted number of spurious signal events, the distribution in the middle row depicts the spurious signal strength μ_{SP} and the bottom histogram exhibits the distribution of $\mu_{SP}/\sigma^{exp}(\mu)$. The uncertainty bars in the two upper plot indicate the expected statistical uncertainty assuming the luminosity in data.

9 Statistical Methods

This chapter will introduce the statistical methods employed to obtain the results for the presented analyses.

9.1 Likelihood Definition

The search is performed in a binned histogram of the invariant dimuon mass observable x with a number of observed events in each bin, n_i . The expectation values for n_i can be expressed in terms of the distribution f :

$$f = N_{sig}(\mu, \theta_{norm,s}) \cdot f_{sig}(x) + N_{bkg} \cdot f_{bkg}(x, \vec{\theta}_b), \quad (9.1)$$

with the signal and background probability density functions (p.d.fs), f_{sig} and f_{bkg} , as described in section 7. The signal normalisation N_{sig} hereby depends on the signal strength parameter μ and a normalisation nuisance parameter $\theta_{norm,s}$. The background normalisation N_{bkg} is calculated as the integral of the invariant dimuon mass distribution, and the background p.d.f. is parametrised by the nuisance parameters $\vec{\theta}_b$. Assuming Poisson statistics, the likelihood function \mathcal{L} takes the form:

$$\mathcal{L}(\mu, \vec{\theta}) = \prod_i \frac{f(\mu, \vec{\theta})^{n_i}}{n_i!} \exp(-f(\mu, \vec{\theta})). \quad (9.2)$$

Here, the abbreviation $\vec{\theta} = (\theta_{norm,s}, \vec{\theta}_b)^T$ for all nuisance parameters is used. The likelihood is a function of the tested signal strength hypothesis μ . According to the Neyman-Pearson lemma [112], the optimal statistical test to distinguish two hypotheses is the ratio of the likelihoods of the two hypotheses. This is adopted in the likelihood ratio test statistic $\lambda(\mu)$, defined as:

$$\lambda(\mu) = \frac{\mathcal{L}(\mu, \hat{\hat{\theta}}(\mu))}{\mathcal{L}(\hat{\mu}, \hat{\hat{\theta}}(\hat{\mu}))}, \quad (9.3)$$

where $\hat{\hat{\theta}}$ is the maximum likelihood estimator of the nuisance parameters for the tested value of μ maximising the conditional likelihood, and $\hat{\mu}$ and $\hat{\hat{\theta}}$ are the corresponding estimators maximising the unconditional likelihood. This likelihood function is easily extended to describe multiple categories and datasets by multiplying the individual likelihoods \mathcal{L}_C in each category:

$$\mathcal{L} = \prod_C \mathcal{L}_C, \quad (9.4)$$

where C is the index denoting the category.

9.2 Test Statistic and Sampling Distribution

The likelihood ratio $\lambda(\mu)$ defined in Equation (9.3) is transformed into the test statistic q_μ :

$$q_\mu = -2 \ln \lambda(\mu). \quad (9.5)$$

This log-likelihood ratio test statistic is asymptotically χ^2 distributed with one degree of freedom in the limit of a sufficient number of bins $N \geq 20$, according to Wilk's theorem [98]. From Equ. (9.5) it can be seen that $q_\mu = 0$ describes perfect agreement between the tested μ and the best fit value $\hat{\mu}$, and the higher the value of q_μ the lower the compatibility with the hypothesised μ . The test statistic is modified to include prior assumptions on the signal strength: First, an upward fluctuation in the data should not be regarded as lower compatibility with the μ hypothesis, i.e. if the best fit value $\hat{\mu}$ is larger than the tested hypothesis for μ , the test statistic should evaluate to zero. Further, the background-only hypothesis

should not be excluded, such that the closest *physical* model for a best fit value $\hat{\mu} < 0$ is $\mu = 0$.¹⁹ With these two ingredients, the modified test statistic \tilde{q}_μ reads as:

$$q_\mu \rightarrow \tilde{q}_\mu = \begin{cases} -2 \ln \lambda(\mu) & 0 \leq \hat{\mu} \leq \mu \\ 0 & \hat{\mu} > \mu \\ -2 \ln \frac{\mathcal{L}(\mu, \hat{\theta}(\mu))}{\mathcal{L}(0, \hat{\theta}(0))} & \hat{\mu} \leq 0. \end{cases} \quad (9.6)$$

The next ingredient for the hypothesis testing is the sampling distribution, or p.d.f. $f(\tilde{q}_\mu|\mu')$, of the test statistic given the hypothesis for $\mu = \mu'$. In general, this sampling distribution is unknown, but it can be obtained using MC methods by generating pseudo-data. However, this is CPU-intensive, and an alternative method also employed in this thesis is to use asymptotic formulae for $f(\tilde{q}_\mu|\mu')$, as described in [113]. For each hypothesis for the true value μ' , one gets a distribution $f(\tilde{q}_\mu|\mu')$, which is schematically shown in Figure 9.1. The p -value p_μ describes the probability to get a result with equal or less compatibility as

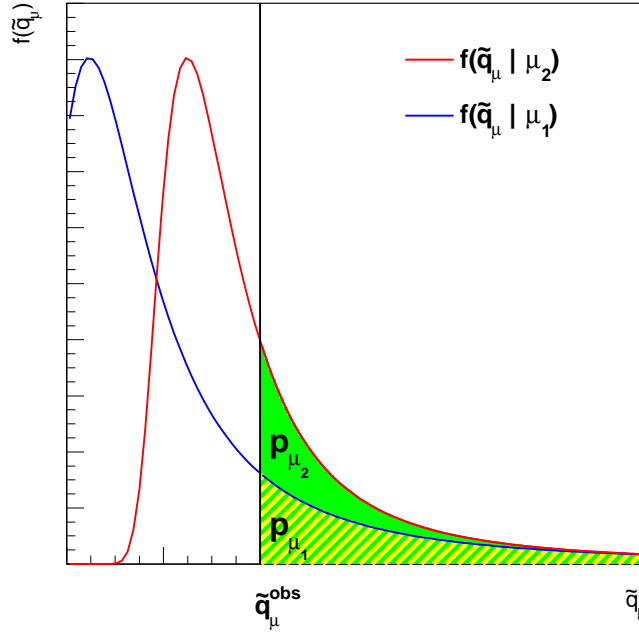


Figure 9.1: Schematic illustration of the sampling distribution $f(\tilde{q}_\mu)$ for two hypothesised true values μ_1, μ_2 . The shaded areas depict the p -values of the sampling distributions for an observed value \tilde{q}_μ^{obs} .

the observed \tilde{q}_{obs} given the assumption on the true value of $\mu = \mu'$:

$$p_\mu = \int_{\tilde{q}_{obs}}^{+\infty} f(\tilde{q}_\mu|\mu') d\tilde{q}_\mu. \quad (9.7)$$

9.3 Modified Frequentist Confidence CL_S

To set an upper limit on μ with a confidence level CL_{S+B} of 95%, one scans the hypotheses μ' to find the value for which $p_\mu = 0.05$. One problem of this hypothesis test is that an exclusion can be claimed even when the experiment has very little sensitivity to μ' , i.e. when the sampling distributions $f(\tilde{q}_\mu|\mu')$ and $f(\tilde{q}_\mu|0)$ are very similar. This situation is depicted schematically in Figure 9.2. The CL_S method was

¹⁹This constraint is specific to this kind of search, other searches may have deviating definitions and may allow for negative signal strengths, as in e.g. neutrino oscillations.

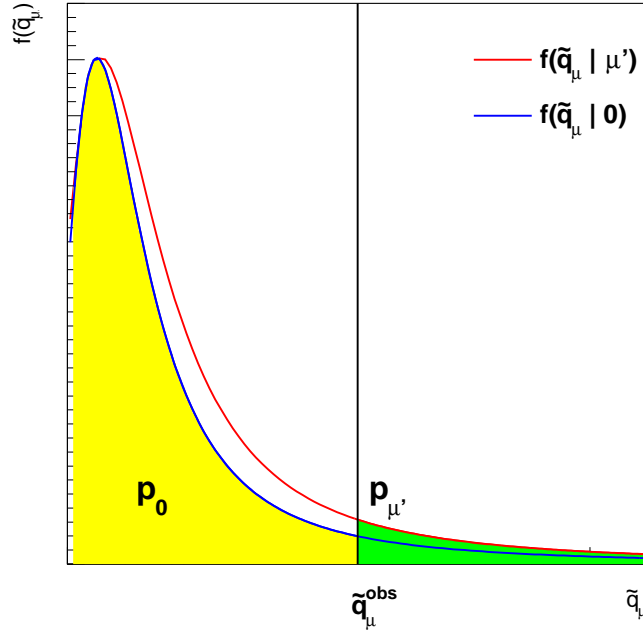


Figure 9.2: Schematic illustration of sampling distributions $f(\tilde{q}_\mu|\mu')$ and $f(\tilde{q}_\mu|0)$ for a low sensitivity measurement, showing the definition of p_0 . The CL_S is, figuratively, the ratio of the green area and one minus the yellow area.

developed to overcome this issue [114]. The CL_S confidence level is defined as:

$$CL_S = \frac{CL_{S+B}}{CL_B} = \frac{p_\mu}{1 - p_0}, \quad (9.8)$$

where p_0 is one minus the p -value for the hypothesis $\mu' = 0$:

$$p_0 = \int_0^{\tilde{q}_{obs}} f(\tilde{q}_\mu|0) d\tilde{q}_\mu. \quad (9.9)$$

The definition of CL_S can be interpreted as a modification of CL_{S+B} , which receives a penalty factor $(1 - p_0)^{-1}$, which gets larger the worse the separation between the sampling distributions $f(\tilde{q}_\mu|\mu')$ and $f(\tilde{q}_\mu|0)$.

9.4 Inclusion of Systematic Uncertainties

The systematic uncertainties described in section 8 are incorporated as additional nuisance parameters modifying the expected signal normalisation:

$$N_{sig}(\mu, \vec{\theta}) = \mu N_{ggF}(\vec{\theta}) + \mu N_{VBF}(\vec{\theta}) + \mu N_{VH}(\vec{\theta}) + N_{SP}(\vec{\theta}), \quad (9.10)$$

with the expected yields from each of the Higgs boson production processes. These yields are no longer fixed, but allowed to vary within the systematic uncertainties, expressed as a constraint and a nuisance parameter for each systematic uncertainty. In addition, the spurious signal N_{SP} is also included as part of the expected signal normalisation, with a corresponding nuisance parameter. The parametrisation of the constraints $K(\theta_u, u)$ for the systematic uncertainty u are implemented as log-normal response terms:

$$K(\theta_u, u) = \exp\left(\theta_u \sqrt{\ln(1 + \sigma_u^2)}\right), \quad (9.11)$$

where σ_u is the relative size of the systematic uncertainty (c.f. section 8). The p.d.f. for the nuisance parameter θ_u itself is a Standard Gaussian distribution with a mean of 0 and a variance of 1. The spurious signal term in Equation (9.10) is implemented as the product of the number of spurious signal events and a Standard Gaussian p.d.f for the θ_{SP} nuisance parameter. Some of the systematic uncertainties are identical among multiple analysis categories, e.g. the luminosity uncertainty. These 100% correlations are taken into account by adding the response term (9.11) in each category, but adding only one nuisance parameter. The systematic uncertainties, the analysis category they affect, and their correlation are listed in Table 9.1 for the standalone 2012 analysis, and in Table 9.2 for the combined 2011+2012 analysis.

uncertainty	affected categories	correlation	comment
\mathcal{L}	all	100%	luminosity
σ_{ggF}	all	100%	gluon fusion cross section
σ_{VBF}	all	100%	VBF cross section
$BR(H \rightarrow \mu\mu)$	all	100%	Higgs branching ratio
$\Delta_{A,central}$	central	none	Acceptance uncertainty, central category
$\Delta_{A,noncentral}$	non-central	none	Acceptance uncertainty, non-central category
experimental	all	none	experimental systematic uncertainties

Table 9.1: Listing of the standalone analysis systematic uncertainties and their treatment in the statistical analysis of the data. A correlation of 100 % means one nuisance parameter for both categories.

uncertainty	affected categories	correlation	comment
\mathcal{L}	all	100% for each CME	luminosity
σ_{ggF}	all	100% for each CME	gluon-fusion cross-section
σ_{VBF}	all	100% for each CME	vector-boson fusion cross-section
σ_{VH}	all	100% for each CME	Higgsstrahlung cross-section
$BR(H \rightarrow \mu\mu)$	all	100%	Higgs branching ratio
MPI_{ggF}	VBF	100% between 7+8 TeV	multi-parton interaction of ggF
MPI_{VBF}	VBF	100% between 7+8 TeV	multi-parton interaction of VBF
$n_{jet_{ggF}}$	VBF	100% between 7+8 TeV	missing terms of ggF events
p_T^H	all	100%	Higgs boson p_T uncertainty
experimental	all	none	experimental systematic uncertainties

Table 9.2: Listing of the combined analysis systematic uncertainties and their treatment in the statistical analysis of the data. The correlation is either between all categories for one centre-of-mass energy (CME), for one category in both CME datasets, or among all categories in both datasets.

10 Results

This section presents the results of the search for the SM Higgs boson in the dimuon decay mode. The dimuon invariant mass spectra observed in data are fitted with the combined signal plus background models for the respective analysis and category, where the signal strength is parametrised by the strength parameter μ . Since there is no hint for a significant signal in the investigated mass range, 95% C.L. upper limits on μ are calculated as a function of the tested Higgs boson mass, following the statistical procedure introduced in section 9.

10.1 Standalone Search Results

The standalone analysis is carried out on the dataset of proton-proton collisions at a centre-of-mass energy of $\sqrt{s} = 8$ TeV recorded by the ATLAS detector in 2012. The target dimuon invariant mass distributions are obtained by applying the trigger and baseline selections as outlined in section 6.2 and the selection cuts specific for the standalone analysis (see section 6.3.2). Then, the signal model (7.1) and background model (7.3) are used in the likelihood function (9.2) for the definition of the test statistic (9.6), and upper limits on μ as a function of the tested SM Higgs boson mass hypothesis are calculated with a 95% confidence level using the CL_s definition (9.8). The range of the tested masses extends between 110 GeV and 150 GeV, in steps of 1 GeV. Figure 10.1 shows the obtained limit together with its one and two σ uncertainty bands, including the systematic uncertainties summarised in section 8. A signal strength of $\mu \geq 10.13$ is excluded for a SM Higgs boson with a mass of 125.5 GeV with 95% confidence level. The observed and expected exclusion limits of the standalone analysis for different SM Higgs boson mass hypotheses are summarised in Table 10.1.

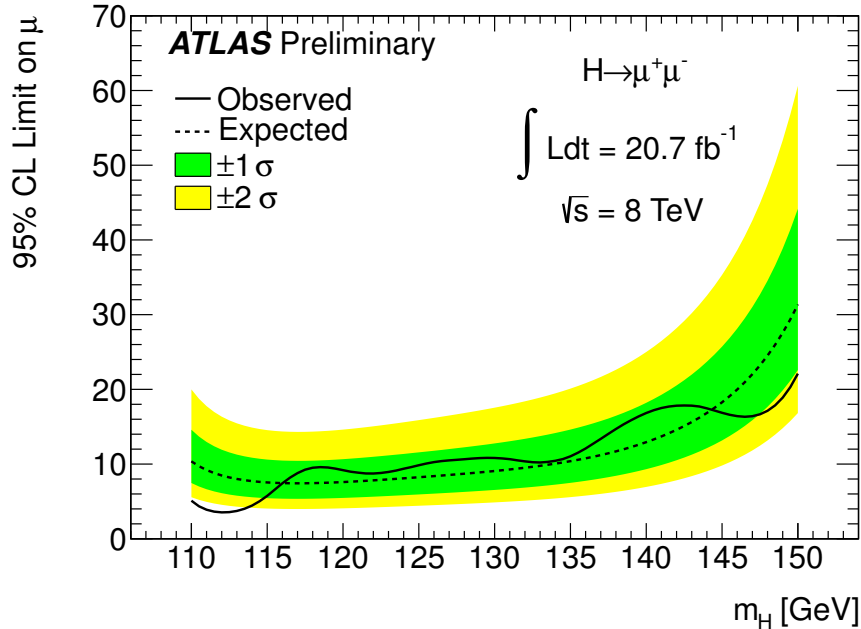


Figure 10.1: Observed (solid line) and expected (dashed line) 95% C.L. exclusion limit on the signal strength $\mu = \sigma/\sigma_{SM}$ as a function of the tested Higgs boson mass, obtained using the 2012 dataset in the standalone analysis. The expected limit is obtained using asymptotic formulae described in detail in [113]. The one and two sigma uncertainty bands on the expectation are shown as green and yellow shaded areas, respectively [92].

m_H [GeV]	Obs.	Exp.	Exp. $+2\sigma$	Exp. $+1\sigma$	Exp. -1σ	Exp. -2σ
110	5.10	10.36	19.99	14.60	7.47	5.56
115	5.74	7.54	14.54	10.60	5.43	4.05
120	9.19	7.59	14.61	10.66	5.47	4.08
125	9.85	8.24	15.88	11.57	5.94	4.42
130	10.82	9.07	17.55	12.77	6.54	4.87
135	11.04	10.39	20.10	14.62	7.49	5.58
140	16.84	12.94	25.00	18.20	9.32	6.94
145	16.86	18.27	35.32	25.72	13.16	9.80
150	22.11	31.35	60.62	44.17	22.59	16.83

Table 10.1: Expected and observed upper limits on the signal strength μ at 95% C.L. for a collection of Higgs boson mass hypotheses, obtained using proton-proton collision data recorded in 2012 at $\sqrt{s} = 8$ TeV [92].

10.2 Combined Search Result

In analogy to the standalone search, the combined analysis selection and categorisation as described in section 6.3.3 is applied. The proton-proton collision datasets collected by the ATLAS detector at centre-of-mass energies $\sqrt{s} = 7$ TeV and 8 TeV in 2011 and 2012 are used to obtain the dimuon invariant mass distributions in the 14 analysis categories, 7 for each dataset. The likelihood function is the product of the likelihoods in each category, taking the different background models for the $p_T^{\mu\mu}$ categories and the VBF category into account (c.f. section 7.2.2). Upper limits at 95% confidence level are set on the signal strength μ for Higgs mass hypotheses in the range between $m_H = 120$ GeV and 150 GeV. This search range is smaller than for the standalone analysis in order to reduce spurious signal systematic uncertainty induced by the combined analysis background models (see section 8.3.2). The graphical illustration of the observed and expected limits including all systematic uncertainties described in section 8 is shown in Figure 10.2. The observed (expected) limit on μ for a SM Higgs boson with a mass of $m_H = 125.5$ GeV is 7.05 (7.15) times the Standard Model expectation. The observed and expected limits for different Higgs boson mass hypotheses as well as the uncertainty on the expectation are collected in Table 10.2.

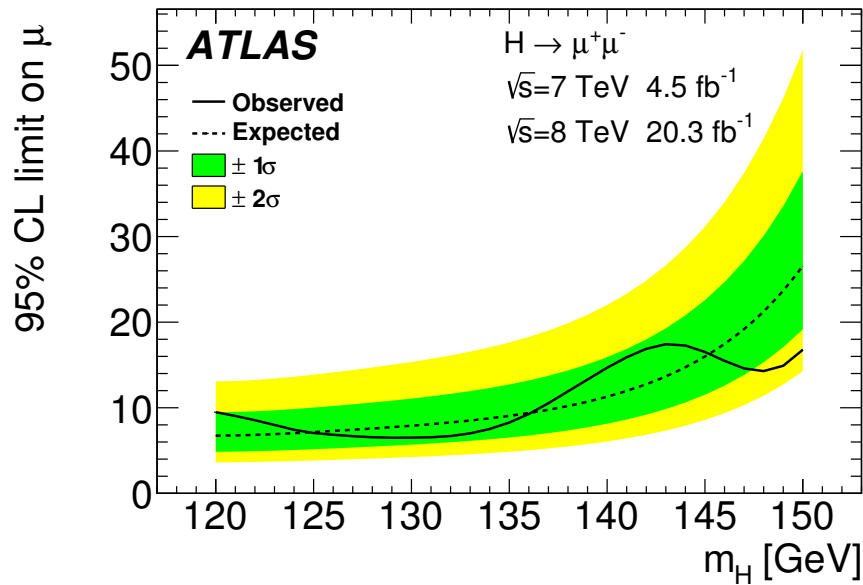


Figure 10.2: Observed (solid line) and expected (dashed line) 95% C.L. exclusion limit on the signal strength $\mu = \sigma/\sigma_{SM}$ as a function of the tested Higgs boson mass, obtained using the 2011 and 2012 datasets in the combined analysis. The expected limit is obtained using asymptotic formulae described in detail in [113]. The one and two sigma uncertainty bands on the expectation are shown as green and yellow shaded areas, respectively [115].

m_H [GeV]	Obs.	Exp.	Exp. $+2\sigma$	Exp. $+1\sigma$	Exp. -1σ	Exp. -2σ
120	9.48	6.74	9.48	13.08	4.86	3.62
125	7.05	7.15	10.02	13.87	5.15	3.84
130	6.51	7.90	11.07	15.35	5.69	4.24
135	8.27	9.05	12.72	17.62	6.52	4.86
140	14.67	11.29	15.91	22.00	8.14	6.06
145	16.52	15.99	22.58	31.16	11.52	8.58
150	16.77	26.57	37.65	51.75	19.15	14.26

Table 10.2: Expected and observed upper limits on the signal strength μ at 95% C.L. for a collection of Higgs boson mass hypotheses, obtained applying the combined analysis to proton-proton collision data recorded in 2011 and 2012 [115].

10.3 Comparison with CMS

The CMS experiment performed a similar measurement searching for the dimuon decay of a Standard Model Higgs boson [116], utilising datasets of proton-proton collisions recorded by the CMS detector in 2011 and 2012 at centre-of-mass energies $\sqrt{s} = 7$ TeV and 8 TeV, which correspond to a total integrated luminosity of 24.7 fb^{-1} . The exclusion limit on μ obtained by CMS as a function of the tested Higgs boson mass is shown in Figure 10.3. For comparison, the ATLAS result is shown side-by-side. It can be observed that the expected limit stated by the CMS collaboration is systematically lower than the ATLAS result. The main reason lies in the dimuon mass resolution of CMS, which is approximately 30% better than in ATLAS [117]. The CMS collaboration exploits the better performance of the CMS muon spectrometer by having additional resolution categories. However, the observed limit on μ obtained by CMS for a SM Higgs boson mass of 125.5 GeV is 7.4 times the Standard Model expectation, quite similar to the result obtained in this thesis, which is also claimed by the ATLAS collaboration using the combined analysis.

10.4 Embedding into other ATLAS Higgs Results

The upper limit on the signal strength $\mu = (\sigma \times BR)/(\sigma_{SM} \times BR_{SM})$ corresponds to an upper limit on the branching ratio under the assumption that $\sigma = \sigma_{SM}$. For a Higgs boson with a mass of 125.5 GeV, the limit on the branching ratio therefore is $BR(H \rightarrow \mu\mu) < 1.3 \times 10^{-3}$ at 95% confidence level. Here, the uncertainties on σ_{SM} are taken into account. Further, the branching ratio depends quadratically on the mass of the decay particle (see sections 2.1.2.2 and 2.2.2), which in turn arises from the Yukawa coupling to the Higgs boson. Thus, the limit on the branching ratio corresponds to an upper limit on the Yukawa coupling of the muon of $\lambda_\mu < 1.60 \times 10^{-3}$. This limit is compared with the current ATLAS results on the couplings of the SM Higgs boson to tau-leptons, b -quarks, W and Z -bosons and top-quarks [12] in Figure 10.4. It can be observed that the result from the presented analysis is consistent with the SM expectation, and that the prediction of the couplings is valid over several orders of magnitude of the particle mass within current experimental uncertainties.

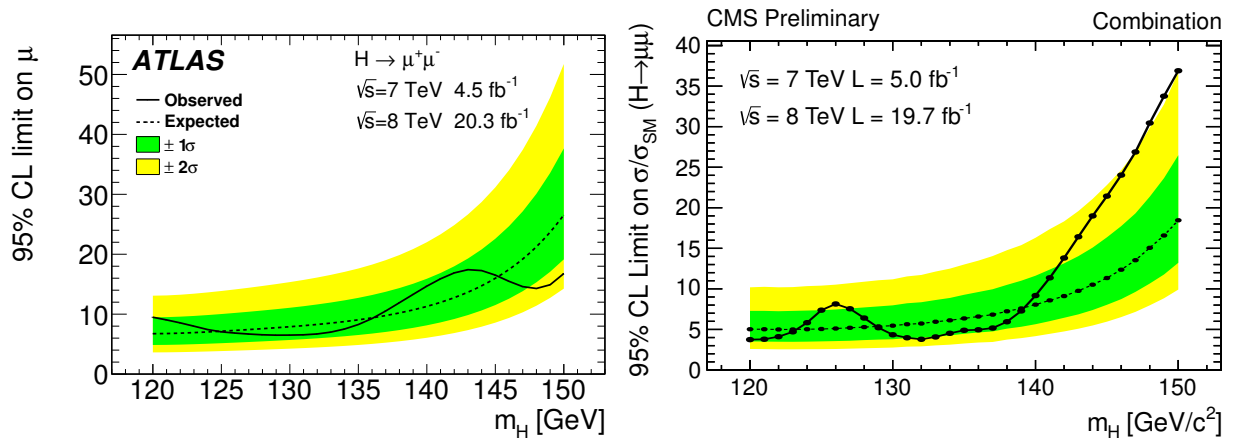


Figure 10.3: Expected and observed limits on μ as a function of the Higgs boson mass hypothesis obtained by ATLAS [115] (left) and CMS [116] (right). The one and two σ uncertainty bands of the expectation are shown as shaded green and yellow areas, respectively.

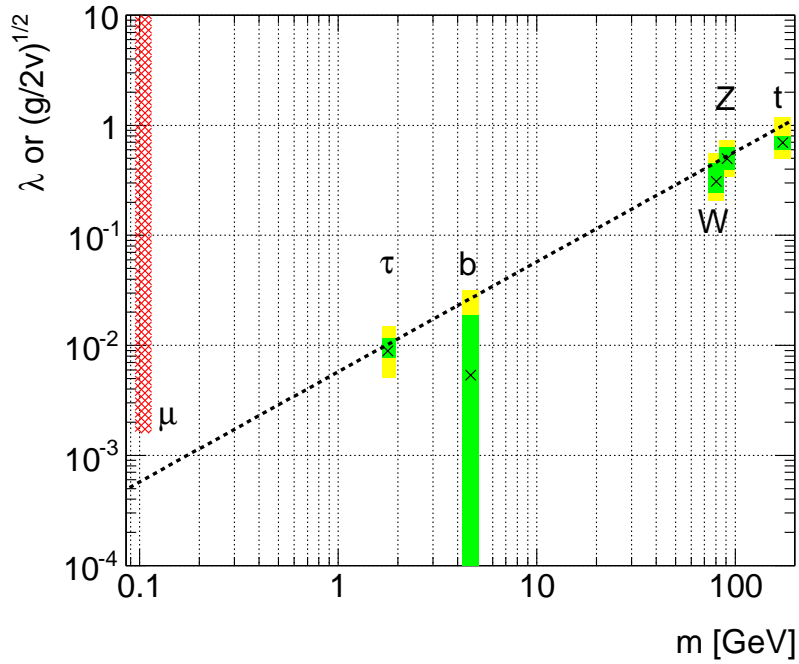


Figure 10.4: Comparison of the obtained upper limit on the muon Yukawa coupling indicated by the red shaded area to the measurement of the couplings of other fundamental particles by ATLAS [12]. The black dashed line indicates the SM prediction, and the black crosses mark the measurements. The green and yellow areas depict the one and two σ uncertainty bands, respectively. The ordinate describes the Yukawa coupling λ for fermions and the square-root of the Higgs boson coupling to the heavy vector bosons W and Z .

11 Summary and Outlook

In this thesis, two searches for a Standard Model Higgs boson in the dimuon decay channel were presented. The proton-proton collision datasets recorded by the ATLAS detector in 2011 and 2012 at centre-of-mass energies of $\sqrt{s} = 7$ TeV and 8 TeV were used to obtain dimuon invariant mass spectra. The standalone analysis hereby drew upon the sole 2012 dataset, splitting events in two resolution categories, whereas the combined analysis resorted on seven analysis categories using the complete run-I dataset. The spectra were then investigated for a signal of a Standard Model Higgs boson with masses ranging from 110 GeV to 150 GeV, using analytical parametrisations of the signal and background shapes. Neither of the analyses had the sensitivity to observe a significant hint for a signal, and upper limits were set on the signal strength as a function of the Higgs boson mass. Thus, a boson with properties similar to the Standard Model Higgs boson, but with a higher signal strength $\mu = \sigma/\sigma_{SM}$ is excluded with 95% confidence level. The excluded signal strengths hereby range from $\mu \geq 6.51$ for $m_H = 130$ GeV to $\mu \geq 16.77$ for $m_H = 150$ GeV for the combined analysis.

Both the standalone and the combined analyses drew profit from very precise estimations of methodical systematic uncertainties, with instruments developed and refined in the course of this thesis. The signal acceptance uncertainty determination of the standalone analysis was the best approach to estimate the impact of Monte Carlo simulation shortcomings on the signal yield, until refined methods using next-to-next-to leading order calculations became available. The usage of smeared generator-level background samples with very high statistical accuracy to determine the spurious signal of the combined analysis' background models constitutes a novel approach to overcome the shortcomings of the spurious signal technique. For the first time, the spurious signal was measured with an accuracy up to $\mu_{SP}/\sigma_{stat}(\mu_{SP}) = 0.01$.

Further, in the light of the discovery of a boson consistent with a Standard Model Higgs boson by other analyses, limits were placed on the branching ratio of $BR(H \rightarrow \mu\mu) \leq 1.3 \times 10^{-3}$ and on the muon Yukawa coupling of $\lambda_\mu \leq 1.6 \times 10^{-3}$ for a Higgs boson mass of 125.5 GeV. These results are consistent with the expectations for a Standard Model Higgs boson.

The comparison of the standalone and the combined analysis showed an improvement of approximately 30% for the observed limit for $m_H = 125.5$ GeV in the combined analysis, while at the same time the dataset size increased by only 22%. This shows the success of the event categorisation and the improvements in the background modeling, while keeping the systematic uncertainties of the analysis low. The observed upper limit is slightly better than the result presented by the CMS collaboration, which nevertheless outperforms ATLAS in the expected limit due to a better detector resolution.

The size of the available dataset is the limiting factor for the sensitivity of this search. With the start of run-II of the LHC in 2015, the collection of collision data will be resumed at a higher centre-of-mass energy of 13 TeV [118]. This increases the production cross-section for the SM Higgs boson by a factor of approximately two. Though the background rate will also increase, a rough estimation indicates that the present combined analysis will reach sensitivity to the Standard Model $H \rightarrow \mu\mu$ process with an integrated luminosity of approximately 300 fb⁻¹. With the current LHC plans, this amount of data will be collected after the phase I upgrade of the LHC in 2018.

This simple extrapolation does not include analysis improvements. Other ATLAS Higgs analyses, e.g. the $H \rightarrow \tau\tau$ search, have been using boosted decision trees as a multivariate classifier to separate signal and background events. The search for the dimuon decay of the Standard Model Higgs boson might adopt multivariate techniques to boost its sensitivity beyond simple statistical improvements. However, the impact of systematic uncertainties has to be re-evaluated in this case. A simpler way to improve the presented analysis is to adopt more analysis categories, analogous to the approach utilised by the CMS collaboration. The signal and background modeling will have to be re-examined and improved, but the overall analysis technique as well as the treatment of the systematic uncertainties can be reused. Whatever a future search for the Higgs boson decay into a muon pair with the ATLAS detector may look like, it is now crucial to prepare for the next data-taking run at the LHC, and the foundations for future searches have been laid out clearly in this thesis.

A Auxiliary Information on Conventions and Units

This section will give additional information on the conventions and units of measure used in this thesis.

Naming Conventions The names of elementary particles implicitly also refer to the respective anti-particles, unless specifically stated otherwise. For example, dimuon stands for a pair consisting of a muon and an antimuon. The term *lepton* usually refers to the charged leptons and does not include the neutrinos, except explicitly said so.

In the theoretical considerations of this thesis, the following conventions and namings are used. The partial derivative with respect to the four spacetime-coordinates is denoted as ∂^μ . The Levi-Civita-Symbol, ϵ^{abc} is defined as:

$$\epsilon^{abc} = \begin{cases} +1 & \text{if } a, b, c \text{ is an even permutation of } 1, 2, 3 \\ -1 & \text{if } a, b, c \text{ is an odd permutation of } 1, 2, 3 \\ 0 & \text{if at least two indices are identical.} \end{cases}$$

Units of Measure Throughout this thesis, natural units are used, setting $\hbar = c = k_B = 1$. Energies, momenta and particle masses are expressed in electronvolts eV, implicitly meaning eV/c for momenta and eV/c² for masses. Cross-sections are measured in barn: $1b = 10^{-24} \text{ cm}^2$, usually with the numeric prefixes *pico* = 10⁻¹² or *femto* = 10⁻¹⁵. The instantaneous luminosity \mathcal{L} is measured in $\text{cm}^{-2}\text{s}^{-1}$. The integrated luminosity \mathcal{L}_{int} or $\int \mathcal{L} dt$ is expressed in inverse barn b^{-1} and its respective SI prefixes, commonly inverse femtobarn fb⁻¹.

B Monte Carlo Simulated Samples

This section summarises the Monte Carlo simulated signal and background samples used in this analysis. The process, dataset ID, generator are given, as well as the sample cross-section σ and generator filter efficiency ϵ_F .

B.1 Samples for the Standalone Analysis

B.1.1 Background Samples

Sample	Data set ID	Generator	Generator cuts	σ [pb]	ϵ_F
Unbinned	147807	Powheg+Pythia8	$m_{\mu\mu} > 60$ GeV	1109.8	1.0
Mass-filtered	129524	Powheg+Pythia8	$120 \leq m_{\mu\mu} < 180$ GeV	9.8460	1.0
Mass-filtered	129525	Powheg+Pythia8	$180 \leq m_{\mu\mu} < 250$ GeV	1.5710	1.0

Table B.1: 8 TeV $Z/\gamma^* \rightarrow \mu\mu$ samples.

Sample	Data set ID	Generator	Generator cuts	σ [pb]	ϵ_F
$q\bar{q} \rightarrow W^+W^- \rightarrow$					
$e\bar{e}e\nu$	126928	Powheg+Pythia8		0.631	1.0
$\mu\bar{\nu}e\nu$	126929	Powheg+Pythia8		0.631	1.0
$\tau\bar{\nu}e\nu$	126930	Powheg+Pythia8		0.631	1.0
$e\nu\mu\nu$	126931	Powheg+Pythia8		0.631	1.0
$\mu\nu\mu\nu$	126932	Powheg+Pythia8		0.631	1.0
$\tau\nu\mu\nu$	126933	Powheg+Pythia8		0.631	1.0
$e\nu\tau\nu$	126934	Powheg+Pythia8		0.631	1.0
$\mu\nu\tau\nu$	126935	Powheg+Pythia8		0.631	1.0
$\tau\nu\tau\nu$	126936	Powheg+Pythia8		0.631	1.0
$gg \rightarrow W^+W^- \rightarrow$					
$e\bar{e}e\nu$	106011	gg2WW		0.018	1.0
$e\nu\mu\nu$	106012	gg2WW		0.018	1.0
$e\nu\tau\nu$	106013	gg2WW		0.018	1.0
$\mu\nu\mu\nu$	106014	gg2WW		0.018	1.0
$\mu\nu e\nu$	106015	gg2WW		0.018	1.0
$\mu\nu\tau\nu$	106016	gg2WW		0.018	1.0
$\tau\nu\tau\nu$	106017	gg2WW		0.018	1.0
$\tau\nu e\nu$	106018	gg2WW		0.018	1.0
$\tau\nu\mu\nu$	106019	gg2WW		0.018	1.0

Table B.2: 8 TeV WW diboson samples.

Sample	Data set ID	Generator	Generator cuts	σ [pb]	ϵ_F
$q\bar{q} \rightarrow W^+Z \rightarrow$					
$e\bar{e}e$	129477	Powheg+Pythia8		1.407	0.29456
$e\nu\mu\mu$	129478	Powheg+Pythia8		0.9382	0.35211
$e\nu\tau\tau$	129479	Powheg+Pythia8		0.1746	0.16682
$\mu\bar{\nu}e$	129480	Powheg+Pythia8		1.399	0.29351
$\mu\nu\mu\mu$	129481	Powheg+Pythia8		0.9537	0.35132
$\mu\nu\tau\tau$	129482	Powheg+Pythia8		0.1746	0.16863
$\tau\bar{\nu}e$	129483	Powheg+Pythia8		1.399	0.14289
$\tau\nu\mu\mu$	129484	Powheg+Pythia8		0.9382	0.18256
$\tau\nu\tau\tau$	129485	Powheg+Pythia8		0.1719	0.058517
$q\bar{q} \rightarrow W^-Z \rightarrow$					
$e\bar{e}e$	129486	Powheg+Pythia8		0.9795	0.29694
$e\nu\mu\mu$	129487	Powheg+Pythia8		0.639	0.35302
$e\nu\tau\tau$	129488	Powheg+Pythia8		0.1125	0.15969
$\mu\bar{\nu}e$	129489	Powheg+Pythia8		0.9359	0.29766
$\mu\nu\mu\mu$	129490	Powheg+Pythia8		0.6488	0.35414
$\mu\nu\tau\tau$	129491	Powheg+Pythia8		0.1125	0.16023
$\tau\bar{\nu}e$	129492	Powheg+Pythia8		0.9359	0.14803
$\tau\nu\mu\mu$	129493	Powheg+Pythia8		0.639	0.18657
$\tau\nu\tau\tau$	129494	Powheg+Pythia8		0.1107	0.056651

Table B.3: 8 TeV WZ diboson samples.

Sample	Data set ID	Generator	Generator cuts	σ [pb]	ϵ_F
$q\bar{q} \rightarrow W^{+/-}\gamma^* \rightarrow$					
$l\nu e$	146890	MadGraph	$m_{ll} < 7 \text{ GeV}$	5.6 *2.01	1.0
$l\nu\mu\mu$	146892	MadGraph	$m_{ll} < 7 \text{ GeV}$	1.3777*2.01	1.0
$l\nu\tau\tau$	146894	MadGraph	$m_{ll} < 7 \text{ GeV}$	0.14717*2.01	1.0
$q\bar{q} \rightarrow W^{+/-}\gamma \rightarrow$					
$l\nu + 0p$	146436	Alpgen	$p_T > 18 \text{ GeV}, \eta < 3.0$	229.88*1.15	0.31372
$l\nu + 1p$	146437	Alpgen	$p_T > 18 \text{ GeV}, \eta < 3.0$	59.518*1.15	0.44871
$l\nu + 2p$	146438	Alpgen	$p_T > 18 \text{ GeV}, \eta < 3.0$	21.39*1.15	0.54461
$l\nu + 3p$	146439	Alpgen	$p_T > 18 \text{ GeV}, \eta < 3.0$	7.1203*1.15	0.62974
$l\nu + 4p$	146434	Alpgen		2.1224*1.15	1.0
$l\nu + 5p$	146435	Alpgen		0.46612*1.15	1.0

Table B.4: 8 TeV W γ diboson samples.

Sample	Data set ID	Generator	Generator cuts	σ [pb]	ϵ_F
$q\bar{q} \rightarrow ZZ \rightarrow$					
$4e$	126937	Powheg+Pythia	$m_{ll} > 4 \text{ GeV}$	0.0735	0.90765
$2e2\mu$	126938	Powheg+Pythia	$m_{ll} > 4 \text{ GeV}$	0.1708	0.82724
$2e2\tau$	126939	Powheg+Pythia	$m_{ll} > 4 \text{ GeV}$	0.1708	0.58278
4μ	126940	Powheg+Pythia	$m_{ll} > 4 \text{ GeV}$	0.0735	0.91241
$2\mu2\tau$	126941	Powheg+Pythia	$m_{ll} > 4 \text{ GeV}$	0.1708	0.90765
4τ	126942	Powheg+Pythia	$m_{ll} > 4 \text{ GeV}$	0.0735	0.10604
$ee\nu\nu$	126949	Powheg+Pythia	$m_{ll} > 4 \text{ GeV}$	0.168	1.0
$\mu\mu\nu\nu$	126950	Powheg+Pythia	$m_{ll} > 4 \text{ GeV}$	0.168	1.0
$\tau\tau\nu\nu$	126951	Powheg+Pythia	$m_{ll} > 4 \text{ GeV}$	0.168	1.0
$gg \rightarrow ZZ \rightarrow$					
$4e$	116601	gg2ZZ		0.00075	1.0
4μ	116601	gg2ZZ		0.00075	1.0
$2e2\mu$	116601	gg2ZZ		0.0015	1.0

Table B.5: 8 TeV ZZ diboson samples.

Sample	Data set ID	Generator	Generator cuts	σ [pb]	ϵ_F
$q\bar{q} \rightarrow W^{+/-} \rightarrow$					
$e\nu + 0p$	107680	Alpgen		8037.1*1.19	1.0
$e\nu + 1p$	107681	Alpgen		1579.2*1.19	1.0
$e\nu + 2p$	107682	Alpgen		477.2*1.19	1.0
$e\nu + 3p$	107683	Alpgen		133.93*1.19	1.0
$e\nu + 4p$	107684	Alpgen		35.622*1.19	1.0
$e\nu + 5p$	107685	Alpgen		10.553*1.19	1.0
$\mu\nu + 0p$	107690	Alpgen		8040*1.19	1.0
$\mu\nu + 1p$	107691	Alpgen		1580.3*1.19	1.0
$\mu\nu + 2p$	107692	Alpgen		477.5*1.19	1.0
$\mu\nu + 3p$	107693	Alpgen		133.94*1.19	1.0
$\mu\nu + 4p$	107694	Alpgen		35.636*1.19	1.0
$\mu\nu + 5p$	107695	Alpgen		10.571*1.19	1.0
$\tau\nu + 0p$	107700	Alpgen		8035.8*1.19	1.0
$\tau\nu + 1p$	107701	Alpgen		1579.8*1.19	1.0
$\tau\nu + 2p$	107702	Alpgen		477.55*1.19	1.0
$\tau\nu + 3p$	107703	Alpgen		133.79*1.19	1.0
$\tau\nu + 4p$	107704	Alpgen		35.583*1.19	1.0
$\tau\nu + 5p$	107705	Alpgen		10.54*1.19	1.0

Table B.6: 8 TeV W+jets samples.

Sample	Data set ID	Generator	Generator cuts	σ [pb]	ϵ_F
$q\bar{q}/gg \rightarrow t\bar{t}$	110001	MC@NLO	dilepton filter	238.06	0.105
Single top (tchan \rightarrow e)	117360	AcerMC		9.48	1.0
Single top (tchan \rightarrow μ)	117361	AcerMC		9.48	1.0
Single top (tchan \rightarrow τ)	117362	AcerMC		9.48	1.0
Single top (schan \rightarrow e)	108343	MC@NLO		0.606	1.0
Single top (schan \rightarrow μ)	108344	MC@NLO		0.606	1.0
Single top (schan \rightarrow τ)	108345	MC@NLO		0.606	1.0
W+t	108346	MC@NLO		22.37	1.0

Table B.7: 8 TeV Single top and $t\bar{t}$ samples.

B.1.2 Signal Samples

Sample	m_H [GeV]	Data set ID	Generator	σ [fb]	ϵ_F
ggF $H \rightarrow \mu\mu$	100	167380	Powheg+Pythia8	8.548	1.0
	105	167381	Powheg+Pythia8	7.671	1.0
	110	167382	Powheg+Pythia8	6.817	1.0
	115	167383	Powheg+Pythia8	5.960	1.0
	120	167384	Powheg+Pythia8	5.090	1.0
	125	167385	Powheg+Pythia8	4.220	1.0
	130	167386	Powheg+Pythia8	3.374	1.0
	135	167387	Powheg+Pythia8	2.585	1.0
	140	167388	Powheg+Pythia8	1.881	1.0
	145	167389	Powheg+Pythia8	1.307	1.0
	150	167390	Powheg+Pythia8	0.837	1.0

Table B.8: 8 TeV ggF signal samples.

Sample	m_H [GeV]	Data set ID	Generator	σ [fb]	ϵ_F
VBF $H \rightarrow \mu\mu$	100	167391	Powheg+Pythia8	0.572	1.0
	105	167392	Powheg+Pythia8	0.539	1.0
	110	167393	Powheg+Pythia8	0.499	1.0
	115	167394	Powheg+Pythia8	0.455	1.0
	120	167395	Powheg+Pythia8	0.402	1.0
	125	167396	Powheg+Pythia8	0.346	1.0
	130	167397	Powheg+Pythia8	0.286	1.0
	135	167398	Powheg+Pythia8	0.226	1.0
	140	167399	Powheg+Pythia8	0.169	1.0
	145	167400	Powheg+Pythia8	0.121	1.0
	150	167401	Powheg+Pythia8	0.079	1.0

Table B.9: 8 TeV VBF signal samples.

Sample	m_H [GeV]	Data set ID	Generator	σ [fb]	ϵ_F
WH, $H \rightarrow \mu\mu$	100	167402	Pythia8	0.417	1.0
	105	167403	Pythia8	0.353	1.0
	110	167404	Pythia8	0.296	1.0
	115	167405	Pythia8	0.244	1.0
	120	167406	Pythia8	0.196	1.0
	125	167407	Pythia8	0.154	1.0
	130	167408	Pythia8	0.117	1.0
	135	167409	Pythia8	0.084	1.0
	140	167410	Pythia8	0.058	1.0
	145	167411	Pythia8	0.038	1.0
	150	167412	Pythia8	0.023	1.0

Table B.10: 8 TeV WH signal samples.

Sample	m_H [GeV]	Data set ID	Generator	σ [fb]	ϵ_F
ZH, $H \rightarrow \mu\mu$	100	167413	Pythia8	0.233	1.0
	105	167414	Pythia8	0.199	1.0
	110	167415	Pythia8	0.169	1.0
	115	167416	Pythia8	0.141	1.0
	120	167417	Pythia8	0.115	1.0
	125	167418	Pythia8	0.091	1.0
	130	167419	Pythia8	0.069	1.0
	135	167420	Pythia8	0.051	1.0
	140	167421	Pythia8	0.035	1.0
	145	167422	Pythia8	0.023	1.0
	150	167423	Pythia8	0.014	1.0

Table B.11: 8 TeV ZH signal samples.

B.2 Samples for the Combined Analysis

In the combined analysis, the same simulated signal and background samples are used for a centre-of-mass energy of 8 TeV. One difference though is the number of events in the inclusive POWHEG $Z \rightarrow \mu\mu$ sample: while there were only 10 million events available for the standalone analysis, more events were requested for the combined analysis, increasing the number of simulated events for this sample to 30 million. The 7 TeV background samples are listed in Tables B.12-B.17. For the dominating $Z \rightarrow \mu\mu$ background process, ALPGEN was utilised for 7 TeV.

B.2.1 7 TeV Background Samples

Sample	Data set ID	Generator	Generator cuts	σ [pb]	ϵ_F
$q\bar{q} \rightarrow W^+W^- \rightarrow$					
$e\nu e\nu$	126610	Powheg+Pythia6		0.520	1.0
$\mu\nu e\nu$	126611	Powheg+Pythia6		0.520	1.0
$\tau\nu e\nu$	126612	Powheg+Pythia6		0.520	1.0
$e\nu\mu\nu$	126613	Powheg+Pythia6		0.520	1.0
$\mu\nu\mu\nu$	126614	Powheg+Pythia6		0.520	1.0
$\tau\nu\mu\nu$	126615	Powheg+Pythia6		0.520	1.0
$e\nu\tau\nu$	126616	Powheg+Pythia6		0.520	1.0
$\mu\nu\tau\nu$	126617	Powheg+Pythia6		0.520	1.0
$\tau\nu\tau\nu$	126618	Powheg+Pythia6		0.520	1.0
$gg \rightarrow W^+W^- \rightarrow$					
$e\nu e\nu$	106011	gg2WW		0.014	1.0
$e\nu\mu\nu$	106012	gg2WW		0.014	1.0
$e\nu\tau\nu$	106013	gg2WW		0.014	1.0
$\mu\nu\mu\nu$	106014	gg2WW		0.014	1.0
$\mu\nu e\nu$	106015	gg2WW		0.014	1.0
$\mu\nu\tau\nu$	106016	gg2WW		0.014	1.0
$\tau\nu\tau\nu$	106017	gg2WW		0.014	1.0
$\tau\nu e\nu$	106018	gg2WW		0.014	1.0
$\tau\nu\mu\nu$	106019	gg2WW		0.014	1.0

Table B.12: 7 TeV WW diboson samples.

Sample	Data set ID	Generator	Generator cuts	σ [pb]	ϵ_F
$q\bar{q} \rightarrow W^+Z \rightarrow$					
$e\bar{e}e$	126874	Powheg+Pythia6		1.2	0.29991
$e\nu\mu\mu$	126875	Powheg+Pythia6		0.8	0.3563
$e\nu\tau\tau$	126876	Powheg+Pythia6		0.15	0.16705
$\mu\bar{\nu}e$	126877	Powheg+Pythia6		1.2	0.29903
$\mu\nu\mu\mu$	126878	Powheg+Pythia6		0.82	0.36004
$\mu\nu\tau\tau$	126879	Powheg+Pythia6		0.15	0.16751
$\tau\bar{\nu}e$	126880	Powheg+Pythia6		1.2	0.14415
$\tau\nu\mu\mu$	126881	Powheg+Pythia6		0.8	0.18418
$\tau\nu\tau\tau$	126882	Powheg+Pythia6		0.15	0.058496
$q\bar{q} \rightarrow W^-Z \rightarrow$					
$e\bar{e}e$	126883	Powheg+Pythia6		0.81	0.2991
$e\nu\mu\mu$	126884	Powheg+Pythia6		0.54	0.35953
$e\nu\tau\tau$	126885	Powheg+Pythia6		0.093	0.15742
$\mu\bar{\nu}e$	126886	Powheg+Pythia6		0.8	0.29916
$\mu\nu\mu\mu$	126887	Powheg+Pythia6		0.56	0.35766
$\mu\nu\tau\tau$	126888	Powheg+Pythia6		0.093	0.15802
$\tau\bar{\nu}e$	126889	Powheg+Pythia6		0.8	0.14852
$\tau\nu\mu\mu$	126890	Powheg+Pythia6		0.54	0.1877
$\tau\nu\tau\tau$	126891	Powheg+Pythia6		0.092	0.056053

Table B.13: 7 TeV WZ diboson samples.

Sample	Data set ID	Generator	Generator cuts	σ [pb]	ϵ_F
$q\bar{q} \rightarrow W^{+/-}\gamma^* \rightarrow$					
$l\nu e$	146890	MadGraph	$m_{ll} < 7 \text{ GeV}$	4.9958*2.01	1.0
$l\nu\mu\mu$	146892	MadGraph	$m_{ll} < 7 \text{ GeV}$	1.2118*2.01	1.0
$l\nu\tau\tau$	146894	MadGraph	$m_{ll} < 7 \text{ GeV}$	0.12679*2.01	1.0
$q\bar{q} \rightarrow W^{+/-}\gamma \rightarrow$					
$l\nu + 0p$	146436	Alpgen	$p_T > 18 \text{ GeV}, \eta < 3.0$	198.76*1.15	0.31372
$l\nu + 1p$	146437	Alpgen	$p_T > 18 \text{ GeV}, \eta < 3.0$	48.9*1.15	0.44871
$l\nu + 2p$	146438	Alpgen	$p_T > 18 \text{ GeV}, \eta < 3.0$	17.18*1.15	0.54461
$l\nu + 3p$	146439	Alpgen	$p_T > 18 \text{ GeV}, \eta < 3.0$	5.30*1.15	0.62974
$l\nu + 4p$	146434	Alpgen		1.49*1.15	1.0
$l\nu + 5p$	146435	Alpgen		0.396*1.15	1.0

Table B.14: 7 TeV W γ diboson samples.

Sample	Data set ID	Generator	Generator cuts	σ [pb]	ϵ_F
$ZZ \rightarrow$					
$4e$	167310	Powheg+Pythia		0.066	0.90475
4μ	167311	Powheg+Pythia		0.066	0.90432
$2e2\mu$	167312	Powheg+Pythia		0.15	0.82359
$2\mu2\tau$	167313	Powheg+Pythia		0.15	0.57451
$2e2\tau$	167314	Powheg+Pythia		0.15	0.57686
4τ	167315	Powheg+Pythia		0.066	0.10248
$ee\nu\nu$	167317	Powheg+Pythia		0.045967	1
$\mu\mu\nu\nu$	167318	Powheg+Pythia		0.045945	1
$\tau\tau\nu\nu$	167319	Powheg+Pythia		0.046	1

Table B.15: 7 TeV ZZ diboson samples.

Sample	Data set ID	Generator	Generator cuts	σ [pb]	ϵ_F
$W^{+/-} \rightarrow$					
$e\nu + 0p$	107680	Alpgen		6930.5*1.19	1.0
$e\nu + 1p$	107681	Alpgen		1305.3*1.19	1.0
$e\nu + 2p$	107682	Alpgen		378.13*1.19	1.0
$e\nu + 3p$	107683	Alpgen		101.86*1.19	1.0
$e\nu + 4p$	107684	Alpgen		25.68 *1.19	1.0
$e\nu + 5p$	107685	Alpgen		6.9941*1.19	1.0
$\mu\nu + 0p$	107690	Alpgen		6932.4*1.19	1.0
$\mu\nu + 1p$	107691	Alpgen		1305.9*1.19	1.0
$\mu\nu + 2p$	107692	Alpgen		378.07*1.19	1.0
$\mu\nu + 3p$	107693	Alpgen		101.85*1.19	1.0
$\mu\nu + 4p$	107694	Alpgen		25.72 *1.19	1.0
$\mu\nu + 5p$	107695	Alpgen		6.9999*1.19	1.0
$\tau\nu + 0p$	107700	Alpgen		6932.2*1.19	1.0
$\tau\nu + 1p$	107701	Alpgen		1304.9*1.19	1.0
$\tau\nu + 2p$	107702	Alpgen		377.93*1.19	1.0
$\tau\nu + 3p$	107703	Alpgen		101.96*1.19	1.0
$\tau\nu + 4p$	107704	Alpgen		25.708*1.19	1.0
$\tau\nu + 5p$	107705	Alpgen		6.9994*1.19	1.0

Table B.16: 7 TeV W+jets samples.

Sample	Data set ID	Generator	Generator cuts	σ [pb]	ϵ_F
$q\bar{q}/gg \rightarrow t\bar{t}$	110001	MC@NLO	dilepton filter	238.06	0.105
Single top (tchan \rightarrow e)	117360	AcerMC		9.48	1.0
Single top (tchan \rightarrow μ)	117361	AcerMC		9.48	1.0
Single top (tchan \rightarrow τ)	117362	AcerMC		9.48	1.0
Single top (schan \rightarrow e)	108343	MC@NLO		0.606	1.0
Single top (schan \rightarrow μ)	108344	MC@NLO		0.606	1.0
Single top (schan \rightarrow τ)	108345	MC@NLO		0.606	1.0
W+t	108346	MC@NLO		22.37	1.0

Table B.17: 7 TeV Single top and $t\bar{t}$ samples.

B.2.2 7 TeV Signal Samples

Sample	m_H [GeV]	Data set ID	Generator	σ [fb]	ϵ_F
ggF $H \rightarrow \mu\mu$	105	169751	Powheg+Pythia6	6.092	1.0
	110	169752	Powheg+Pythia6	5.399	1.0
	115	169753	Powheg+Pythia6	4.705	1.0
	120	169754	Powheg+Pythia6	4.009	1.0
	125	169755	Powheg+Pythia6	3.313	1.0
	130	169756	Powheg+Pythia6	2.642	1.0
	135	169757	Powheg+Pythia6	2.020	1.0
	140	169758	Powheg+Pythia6	1.466	1.0
	145	169759	Powheg+Pythia6	1.016	1.0
	150	169760	Powheg+Pythia6	0.650	1.0

Table B.18: 7 TeV ggF signal samples.

Sample	m_H [GeV]	Data set ID	Generator	σ [fb]	ϵ_F
VBF $H \rightarrow \mu\mu$	105	169762	Powheg+Pythia6	0.420	1.0
	110	169763	Powheg+Pythia6	0.389	1.0
	115	169764	Powheg+Pythia6	0.353	1.0
	120	169765	Powheg+Pythia6	0.312	1.0
	125	169766	Powheg+Pythia6	0.268	1.0
	130	169767	Powheg+Pythia6	0.221	1.0
	135	169768	Powheg+Pythia6	0.174	1.0
	140	169769	Powheg+Pythia6	0.130	1.0
	145	169770	Powheg+Pythia6	0.092	1.0
	150	169771	Powheg+Pythia6	0.061	1.0

Table B.19: 7 TeV VBF signal samples.

Sample	m_H [GeV]	Data set ID	Generator	σ [fb]	ϵ_F
WH, $H \rightarrow \mu\mu$	105	169773	Pythia6	0.292	1.0
	110	169774	Pythia6	0.244	1.0
	115	169775	Pythia6	0.201	1.0
	120	169776	Pythia6	0.161	1.0
	125	169777	Pythia6	0.127	1.0
	130	169778	Pythia6	0.096	1.0
	135	169779	Pythia6	0.069	1.0
	140	169780	Pythia6	0.048	1.0
	145	169781	Pythia6	0.031	1.0
	150	169782	Pythia6	0.019	1.0

Table B.20: 7 TeV WH signal samples.

Sample	m_H [GeV]	Data set ID	Generator	σ [fb]	ϵ_F
ZH, $H \rightarrow \mu\mu$	105	169784	Pythia6	0.163	1.0
	110	169785	Pythia6	0.137	1.0
	115	169786	Pythia6	0.114	1.0
	120	169787	Pythia6	0.093	1.0
	125	169788	Pythia6	0.073	1.0
	130	169789	Pythia6	0.056	1.0
	135	169790	Pythia6	0.041	1.0
	140	169791	Pythia6	0.028	1.0
	145	169792	Pythia6	0.019	1.0
	150	169793	Pythia6	0.011	1.0

Table B.21: 7 TeV ZH signal samples.

C Auxiliary Information on the Muon Resolution Model

This section provides additional information on the resolution model used to smear generator-level muons, as outlined in section 8.3.2.2. The distributions of the resolution model parameters are shown in Figures C.1-C.4. The distribution of the $\chi^2/ndof$ of the fits is shown in Figure C.5. There are

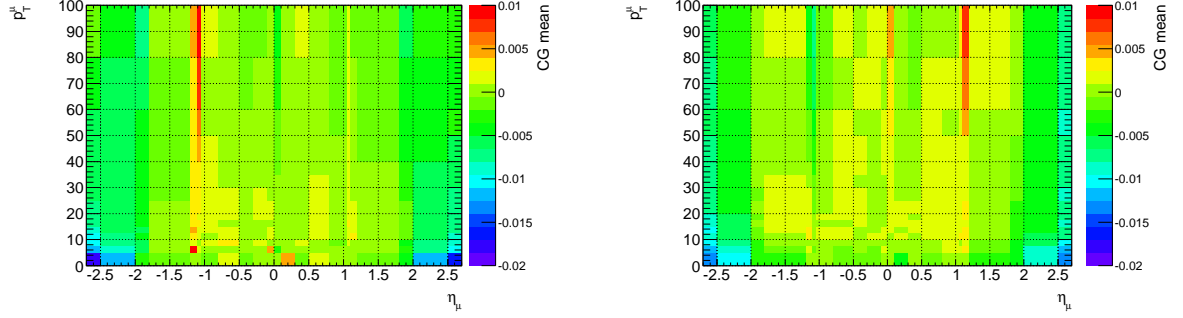


Figure C.1: Parameter distribution of the central Gauss (CG) mean parameter μ_{CG} after fitting to the Δp_T^{rel} distributions, binned in η^{truth} and p_T^{truth} . The left plot shows the distribution for antimuons, and the values obtained for muons are displayed on the right.

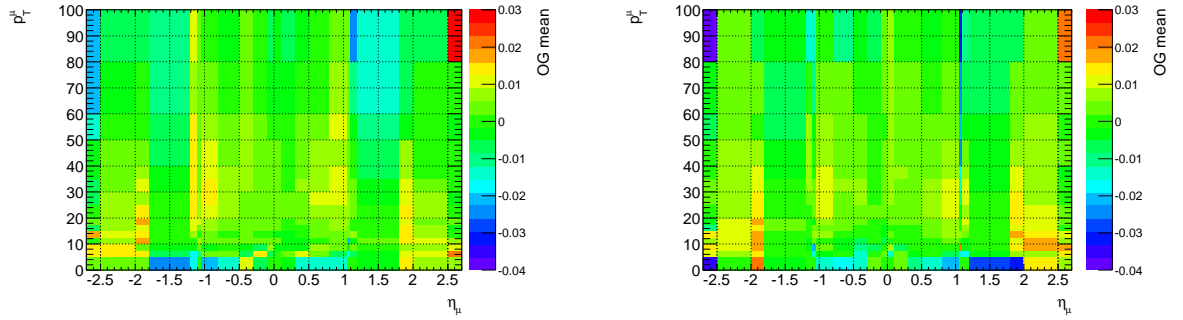


Figure C.2: Parameter distribution of the outer Gauss (OG) mean parameter μ_{OG} after fitting to the Δp_T^{rel} distributions, binned in η^{truth} and p_T^{truth} . The left plot shows the distribution for antimuons, and the values obtained for muons are displayed on the right.

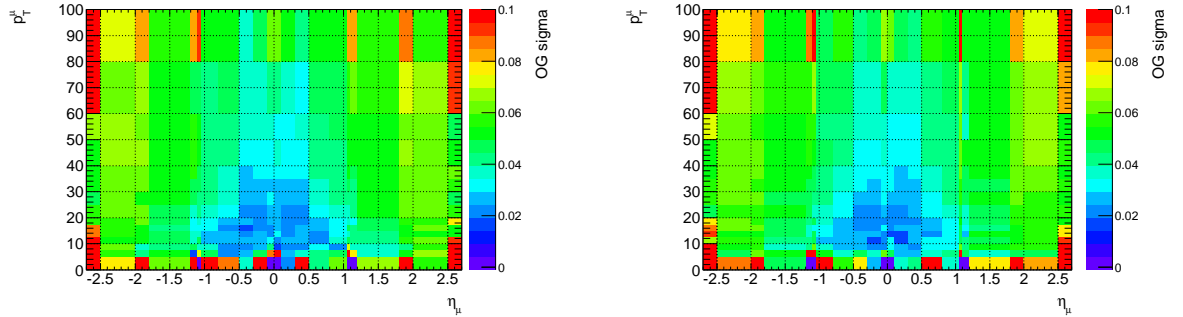


Figure C.3: Parameter distribution of the outer Gauss (OG) width parameter σ_{OG} after fitting to the Δp_T^{rel} distributions, binned in η^{truth} and p_T^{truth} . The left plot shows the distribution for antimuons, and the values obtained for muons are displayed on the right.

obviously regions in the phase space where the fit performs not optimal, as can be seen from the regions

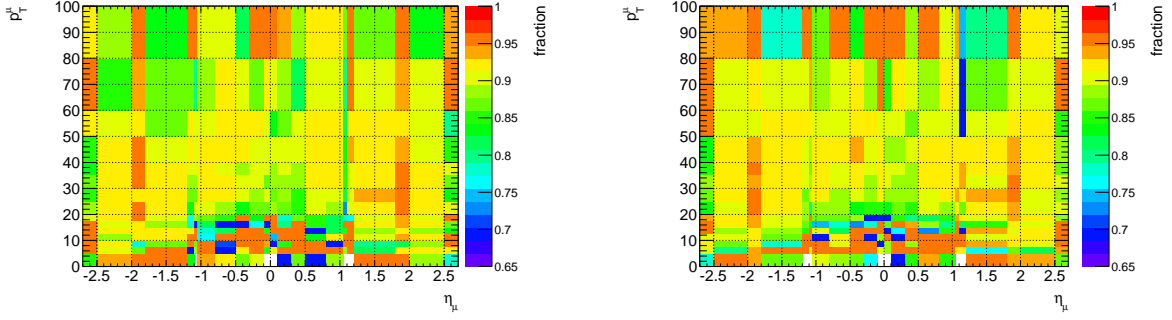


Figure C.4: Parameter distribution of the fraction parameter f between the central and outer Gauss after fitting to the Δp_T^{rel} distributions, binned in η^{truth} and p_T^{truth} . The left plot shows the distribution for positive muons, and the values obtained for negative muons are displayed on the right.

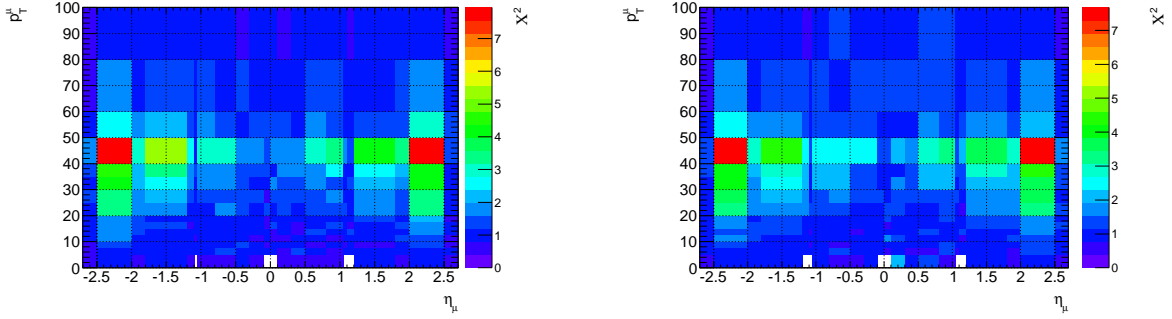


Figure C.5: Distribution of the fit $\chi^2/ndof$, binned in η^{truth} and p_T^{truth} . The left plot shows the distribution for positive muons, and the values obtained for negative muons are displayed on the right.

with high $\chi^2/ndof$. Figures C.6 and C.7 show examples of the Δp_T^{rel} distributions with the fit applied for these regions, compared to regions with good fit performance. The distribution in the high η bin

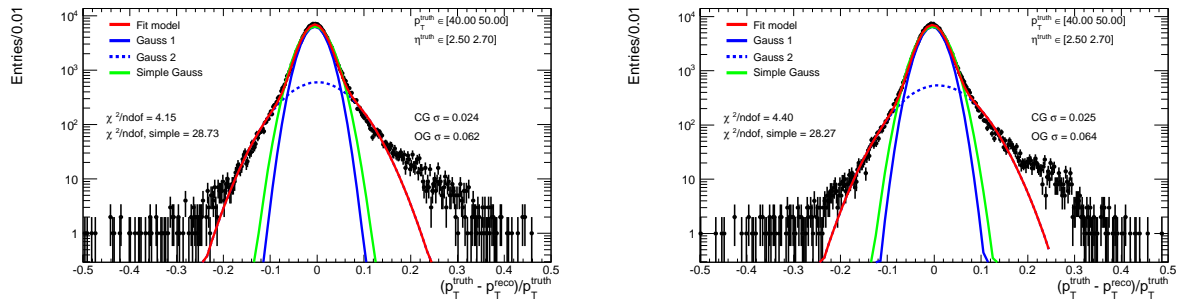


Figure C.6: Distribution of Δp_T^{rel} with a high fit $\chi^2/ndof$. The left plot shows an example for positive muons, and on the right an example with negative muons is displayed.

exhibits significant non-Gaussian tails to both sides which cannot be accurately modeled by the sum of two Gaussian distribution, hence the degraded fit result. However, due to the good overall performance of the simplified resolution model, no attempts to create a refined non-Gaussian model were undertaken.

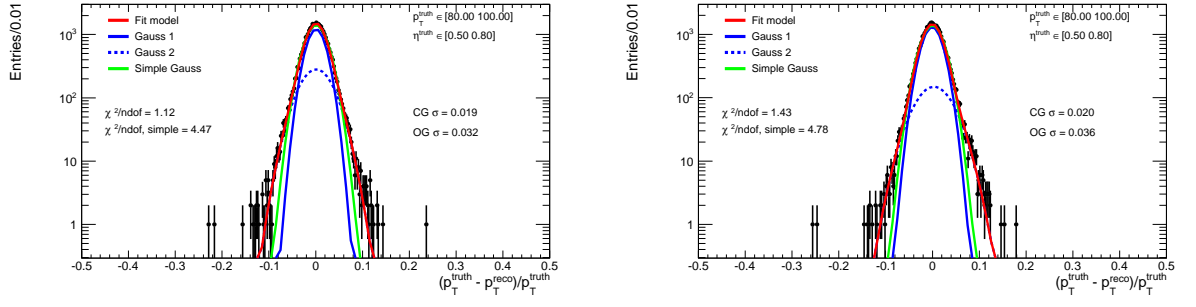


Figure C.7: Distribution of Δp_T^{rel} with a normal fit $\chi^2/ndof$, The left plot shows an example for positive muons, and on the right an example with negative muons is displayed.

Bibliography

ATLAS internal documents are listed for completeness, although not publically available

- [1] G. Zweig, *An SU_3 model for strong interaction symmetry and its breaking; Version I*, Tech. Rep. CERN-TH-401, CERN, Geneva, Jan, 1964.
- [2] J. Schwinger, *A theory of the fundamental interactions*, [Annals of Physics **2** \(1957\) no. 5, 407 – 434.](#)
- [3] S. L. Glashow, *Partial Symmetries of Weak Interactions*, [Nucl. Phys. **22** \(1961\) 579 – 588.](#)
- [4] G. Arnison et al., *Experimental observation of isolated large transverse energy electrons with associated missing energy at $s=540$ GeV*, [Physics Letters B **122** \(1983\) no. 1, 103 – 116.](#)
- [5] G. Arnison et al., *Experimental observation of lepton pairs of invariant mass around 95 GeV/c² at the CERN SPS collider*, [Physics Letters B **126** \(1983\) no. 5, 398 – 410.](#)
- [6] F. Englert and R. Brout, *Broken Symmetry and the Mass of Gauge Vector Mesons*, [Phys. Rev. Lett. **13** \(1964\) 321 – 323.](#)
- [7] P. W. Higgs, *Broken symmetries, massless particles and gauge fields*, [Phys. Lett. **12** \(1964\) 132 – 133.](#)
- [8] P. W. Higgs, *Broken Symmetries and the Masses of Gauge Bosons*, [Phys. Rev. Lett. **13** \(1964\) 508 – 509.](#)
- [9] P. W. Higgs, *Spontaneous Symmetry Breakdown without Massless Bosons*, [Phys. Rev. **145** \(1966\) 1156 – 1163.](#)
- [10] ATLAS Collaboration, *Observation of a new particle in the search for the Standard Model Higgs boson with the ATLAS detector at the LHC*, [Phys. Lett. **B716** \(2012\) no. 1, 1–29.](#)
- [11] CMS Collaboration, *Observation of a new boson at a mass of 125 GeV with the CMS experiment at the LHC*, [Phys. Lett. **B716** \(2012\) no. 1, 30–61, arXiv:1207.7235 \[hep-ex\].](#)
- [12] ATLAS Collaboration, *Updated coupling measurements of the Higgs boson with the ATLAS detector using up to 25 fb⁻¹ of proton-proton collision data*, Tech. Rep. ATLAS-CONF-2014-009, CERN, Geneva, Mar, 2014.
- [13] ATLAS Collaboration, *Evidence for Higgs Boson Decays to the $\tau^+\tau^-$ Final State with the ATLAS Detector*, Tech. Rep. ATLAS-CONF-2013-108, CERN, Geneva, Nov, 2013.
- [14] CMS Collaboration, *Measurement of the properties of a Higgs boson in the four-lepton final state*, [Phys. Rev. D **89** \(May, 2014\) 092007.](#)
- [15] CMS Collaboration, *Measurement of Higgs boson production and properties in the WW decay channel with leptonic final states*, [JHEP **1401** \(2014\) 096, arXiv:1312.1129 \[hep-ex\].](#)
- [16] CMS Collaboration, *Properties of the observed Higgs-like resonance using the diphoton channel*, Tech. Rep. CMS-PAS-HIG-13-016, CERN, Geneva, 2013.
- [17] CMS Collaboration, *Evidence for the 125 GeV Higgs boson decaying to a pair of τ leptons*, [JHEP **1405** \(2014\) 104, arXiv:1401.5041 \[hep-ex\].](#)
- [18] J. Beringer et al. (Particle Data Group), *Review of Particle Physics, 2012-2013*, [Phys. Rev. **D86** \(2012\) 010001.](#)
- [19] S. Weinberg, *A Model of Leptons*, [Phys. Rev. Lett. **19** \(1967\) no. 21, 1264 – 1266.](#)

- [20] A. Salam, *Weak and Electromagnetic Interactions*, *Conf. Proc.* **C680519** (1968) 367–377.
- [21] A. Djouadi, *The Anatomy of electro-weak symmetry breaking. I: The Higgs boson in the standard model*, *Phys.Rept.* **457** (2008) 1–216, [arXiv:hep-ph/0503172](#) [[hep-ph](#)].
- [22] W. Kilian, *Strahlungskorrekturen in Eichtheorien*, Herbstschule Maria Laach **33** (2001) .
- [23] S. Drell and T.-M. Yan, *Massive Lepton Pair Production in Hadron-Hadron Collisions at High-Energies*, *Phys.Rev.Lett.* **25** (1970) 316–320.
- [24] LHC Higgs Cross Section Working Group, *Handbook of LHC Higgs Cross Sections: 1. Inclusive Observables*, [arXiv:1101.0593](#) [[hep-ph](#)].
- [25] E. Braaten and J. P. Leveille, *Higgs-boson decay and the running mass*, *Phys. Rev. D* **22** (Aug, 1980) 715–721.
- [26] M. Gomez-Bock, M. Mondragón, M. Mühlleitner, M. Spira, and P. M. Zerwas, *Concepts of Electroweak Symmetry Breaking and Higgs Physics*, [arXiv:0712.2419](#) [[hep-ph](#)].
- [27] LHC Higgs Cross Section Working Group, *Handbook of LHC Higgs Cross Sections: 2. Differential Distributions*, [arXiv:1201.3084](#) [[hep-ph](#)].
- [28] L. R. Evans and P. Bryant, *LHC Machine*, *JINST* **3** (2008) S08001. 164 p. This report is an abridged version of the LHC Design Report (CERN-2004-003).
- [29] J. Haffner, *The CERN accelerator complex. Complexe des accélérateurs du CERN*, .
- [30] ATLAS Collaboration, *ATLAS Detector images*, 2013. ATLAS Experiment ©2014 CERN.
- [31] ATLAS Collaboration, *Expected Performance of the ATLAS Experiment: Detector, Trigger and Physics*. CERN, Geneva, 2008. [arXiv:0901.0512](#). CERN-OPEN-2008-020.
- [32] ATLAS Collaboration, *ATLAS detector and physics performance: Technical Design Report, Vol. 1*. CERN, Geneva. <http://inspirehep.net/record/511648>.
- [33] ATLAS Collaboration, *Performance of the ATLAS liquid argon endcap calorimeter in the pseudorapidity region in beam tests*, *Nucl. Instr. Meth.* **593** (2008) no. 3, 324 – 342.
- [34] ATLAS Collaboration, *ATLAS muon spectrometer: Technical Design Report*. CERN, Geneva, 1997. <http://inspirehep.net/record/455675>.
- [35] ATLAS Collaboration, *ATLAS magnet system: Technical design report*. CERN, Geneva, 1997. <http://inspirehep.net/record/455674>.
- [36] ATLAS Collaboration, *Performance of the ATLAS Trigger System in 2010*, *Eur. Phys. J. C* **72** (Oct, 2011) 1849. 63 p.
- [37] ATLAS Collaboration, G. Chiodi, E. Gennari, E. Petrolo, F. Pastore, A. Salamon, R. Vari, and S. Veneziano, *The ATLAS barrel level-1 Muon Trigger Sector-Logic/RX off-detector trigger and acquisition board*, . <https://cds.cern.ch/record/1091753>.
- [38] ATLAS Collaboration, *Performance of the ATLAS muon trigger in 2011*, Tech. Rep. ATLAS-CONF-2012-099, CERN, Geneva, Jul, 2012.
- [39] ATLAS Collaboration, *ATLAS first level trigger: Technical design report*, . <http://inspirehep.net/record/479933>.
- [40] V. Cindro et al., *The ATLAS Beam Conditions Monitor*, *JINST* **3** (2008) P02004.

- [41] ATLAS Collaboration, *Improved luminosity determination in pp collisions at $\sqrt{s} = 7$ TeV using the ATLAS detector at the LHC*, [arXiv:1302.4393 \[hep-ex\]](#).
- [42] H. Stenzel, *Luminosity calibration from elastic scattering*, [ATL-LUM-PUB-2007-001](#).
- [43] J. C. Collins, D. E. Soper, and G. F. Sterman, *Factorization of Hard Processes in QCD*, *Adv.Ser.Direct.High Energy Phys.* **5** (1988) 1–91, [arXiv:hep-ph/0409313 \[hep-ph\]](#).
- [44] G. Altarelli and G. Parisi, *Asymptotic Freedom in Parton Language*, *Nucl. Phys.* **B126** (1977) 298.
- [45] P. M. Nadolsky et al., *Implications of CTEQ global analysis for collider observables*, *Phys. Rev.* **D78** (2008) 013004, [arXiv:0802.0007 \[hep-ph\]](#).
- [46] H.-L. Lai et al., *New parton distributions for collider physics*, *Phys. Rev.* **D82** (2010) 074024, [arXiv:1007.2241 \[hep-ph\]](#).
- [47] J. Pumplin et al., *New generation of parton distributions with uncertainties from global QCD analysis*, *JHEP* **07** (2002) 012, [arXiv:hep-ph/0201195](#).
- [48] A. Sherstnev and R. Thorne, *Parton distributions for LO generators*, *EPJC* **55** (2008) 553, [arXiv:0711.2473 \[hep-ph\]](#).
- [49] A. Martin, W. Stirling, R. Thorne, and G. Watt, *Parton distributions for the LHC*, *Eur.Phys.J.* **C63** (2009) 189–285, [arXiv:0901.0002 \[hep-ph\]](#).
- [50] M. L. Mangano, M. Moretti, F. Piccinini, R. Pittau, and A. D. Polosa, *ALPGEN, a generator for hard multiparton processes in hadronic collisions*, *JHEP* **07** (2003) 001, [arXiv:hep-ph/0206293](#).
- [51] J. Alwall, P. Demin, S. de Visscher, R. Frederix, M. Herquet, et al., *MadGraph/MadEvent v4: The New Web Generation*, *JHEP* **0709** (2007) 028, [arXiv:0706.2334 \[hep-ph\]](#).
- [52] S. Catani and M. Seymour, *A General algorithm for calculating jet cross-sections in NLO QCD*, *Nucl.Phys.* **B485** (1997) 291–419, [arXiv:hep-ph/9605323 \[hep-ph\]](#).
- [53] W. Giele, E. Glover, and D. A. Kosower, *Higher-order corrections to jet cross sections in hadron colliders*, *Nuclear Physics B* **403** (1993) no. 3, 633 – 667.
- [54] F. James, *Monte Carlo theory and practice*, *Reports on Progress in Physics* **43** (1980) no. 9, 1145.
- [55] A. Buckley, J. Butterworth, S. Gieseke, D. Grellscheid, S. Hoche, et al., *General-purpose event generators for LHC physics*, *Phys.Rept.* **504** (2011) 145–233, [arXiv:1101.2599 \[hep-ph\]](#).
- [56] M. L. Mangano, M. Moretti, and R. Pittau, *Multijet matrix elements and shower evolution in hadronic collisions: $Wb\bar{b} + n$ jets as a case study*, *Nucl. Phys.* **B632** (2002) 343–362.
- [57] S. Catani, F. Krauss, R. Kuhn, and B. R. Webber, *QCD Matrix Elements + Parton Showers*, *JHEP* **0111** (2001) 063, [arXiv:0109231 \[hep-ph\]](#).
- [58] S. Frixione and B. R. Webber, *Matching NLO QCD computations and parton shower simulations*, *JHEP* **0206** (2002) 029, [arXiv:0204244 \[hep-ph\]](#).
- [59] S. Frixione, P. Nason, and C. Oleari, *Matching NLO QCD computations with Parton Shower simulations: the POWHEG method*, *JHEP* **0711** (2007) 070, [arXiv:0709.2092 \[hep-ph\]](#).
- [60] B. Andersson, G. Gustafson, G. Ingelman, and T. Sj, *Parton fragmentation and string dynamics*, *Physics Reports* **97** (1983) no. 23, 31 – 145.

- [61] T. Sjöstrand, S. Mrenna, and P. Skands, *PYTHIA 6.4 physics and manual*, JHEP **05** (2006) 026, [arXiv:0603175 \[hep-ph\]](#).
- [62] D. Amati and G. Veneziano, *Preconfinement as a property of perturbative QCD*, Physics Letters B **83** (1979) no. 1, 87 – 92.
- [63] G. Corcella et al., *HERWIG 6.5 release note*, [arXiv:0210213 \[hep-ph\]](#).
- [64] T. Gleisberg et al., *Event generation with SHERPA 1.1*, JHEP **02** (2009) 007, [arXiv:0811.4622 \[hep-ph\]](#).
- [65] S. Agostinelli [GEANT4 Collaboration], *GEANT4: A simulation toolkit*, Nucl. Instr. and Meth. A **506** (2003) 250.
- [66] P. Nason, *A New method for combining NLO QCD with shower Monte Carlo algorithms*, JHEP **0411** (2004) 040, [arXiv:hep-ph/0409146 \[hep-ph\]](#).
- [67] *The POWHEG BOX homepage*, <http://powhegbox.mib.infn.it/>.
- [68] S. Frixione, F. Stoeckli, P. Torrielli, B. R. Webber, and C. D. White, *The MCanLO 4.0 Event Generator*, [arXiv:1010.0819 \[hep-ph\]](#).
- [69] T. Sjöstrand, S. Mrenna, and P. Skands, *A Brief Introduction to Pythia 8.1*, [arXiv:0710.3820 \[hep-ph\]](#).
- [70] F. Caravaglios and M. Moretti, *An algorithm to compute Born scattering amplitudes without Feynman graphs*, Phys.Lett. **B358** (1995) 332–338, [arXiv:hep-ph/9507237 \[hep-ph\]](#).
- [71] J. M. Butterworth, J. R. Forshaw, and M. H. Seymour, *Multiparton interactions in photoproduction at HERA*, Z. Phys. **C72** (1996) 637–646, [arXiv:9601371 \[hep-ph\]](#).
- [72] ATLAS Collaboration, *ATLAS detector and physics performance: Technical Design Report, 1*. CERN, Geneva, 1999. <http://inspirehep.net/record/511648>.
- [73] *Preliminary results on the muon reconstruction efficiency, momentum resolution, and momentum scale in ATLAS 2012 pp collision data*, Tech. Rep. ATLAS-CONF-2013-088, CERN, Geneva, Aug, 2013.
- [74] E. Moyse, A. Nisati, A. Oh, and D. Quarrie, *Report of the Muon Reconstruction Selection Panel*, Tech. Rep. ATL-COM-MUON-2011-040, CERN, Geneva, Dec, 2011.
- [75] ATLAS Collaboration, *Muon Performance in Minimum Bias pp Collision Data at $\sqrt{s}=7$ TeV with ATLAS*, Tech. Rep. ATLAS-CONF-2010-036, CERN, Geneva, Jul, 2010.
- [76] ATLAS Collaboration, *Muon Reconstruction Performance*, Tech. Rep. ATLAS-CONF-2010-064, CERN, Geneva, Jul, 2010.
- [77] ATLAS Collaboration Collaboration, *Muon Momentum Resolution in First Pass Reconstruction of pp Collision Data Recorded by ATLAS in 2010*, Tech. Rep. ATLAS-CONF-2011-046, CERN, Geneva, Mar, 2011.
- [78] *ATLAS Muon Combined Performance Wikipage*, <https://twiki.cern.ch/twiki/bin/viewauth/AtlasProtected/MuonPerformance>. Accessed: 2014-02-11.
- [79] M. Woudstra, *Performance of the ATLAS muon trigger in p-p collisions at $\sqrt{s}=8$ TeV*, Tech. Rep. ATL-DAQ-PROC-2013-034, CERN, Geneva, Nov, 2013.

- [80] ATLAS TrigMuonEfficiency, *TrigMuonEfficiency*, <https://twiki.cern.ch/twiki/bin/view/Atlas/TrigMuonEfficiency>.
- [81] ATLAS Collaboration, *Object selection for the $H \rightarrow WW$ search with the ATLAS detector at $\sqrt{s} = 8 \text{ TeV}$, 13 fb^{-1} update*, Tech. Rep. ATL-COM-PHYS-2012-1517, CERN, Geneva, Oct, 2012.
- [82] ATLAS Collaboration Collaboration, *Muon reconstruction efficiency in reprocessed 2010 LHC proton-proton collision data recorded with the ATLAS detector*, Tech. Rep. ATLAS-CONF-2011-063, CERN, Geneva, Apr, 2011.
- [83] *ATLAS Muon Combined Performance Guidelines for Analyses of 2012 Data*, [TWiki Page](#), 2012.
- [84] M. Cacciari, G. P. Salam, and G. Soyez, *The anti- k_t jet clustering algorithm*, *JHEP* **04** (2008) 063, [arXiv:0802.1189 \[hep-ph\]](#).
- [85] *ATLAS JetEtMiss Recommendations for how to clean jets in 2012 data*, <https://twiki.cern.ch/twiki/bin/view/AtlasProtected/HowToCleanJets2012>, 2012.
- [86] ATLAS Collaboration, *Jet energy scale and its systematic uncertainty in proton-proton collisions at $\sqrt{s} = 7 \text{ TeV}$ with ATLAS 2011 data*, [ATLAS-CONF-2013-004](#).
- [87] *ATLAS JetEtMiss Recommendations for 2012 data*, <https://twiki.cern.ch/twiki/bin/viewauth/AtlasProtected/JetEtmissRecommendations2012>, 2012.
- [88] M. zur Nedden, G. Piacquadio, J. Jovicevic, F. Filthaut, T. Scanlon, and F. Parodi, *Calibration of b -tagging using dileptonic top pair events in a combinatorial likelihood approach with the ATLAS experiment*, Tech. Rep. ATLAS-COM-CONF-2014-003, CERN, Geneva, Jan, 2014.
- [89] *ATLAS B-Tag Calibration for the Winter Conferences in 2013*, <https://twiki.cern.ch/twiki/bin/view/AtlasProtected/BTagCalibWinter2013>, 2013.
- [90] *Performance of Missing Transverse Momentum Reconstruction in ATLAS studied in Proton-Proton Collisions recorded in 2012 at 8 TeV*, Tech. Rep. ATLAS-CONF-2013-082, CERN, Geneva, Aug, 2013.
- [91] Data Preparation Group, *Checklist For Physics Analysis*, <https://twiki.cern.ch/twiki/bin/viewauth/Atlas/DataPreparationCheckListForPhysicsAnalysis>.
- [92] ATLAS Collaboration, *Search for a Standard Model Higgs boson in $H \rightarrow \mu\mu$ decays with the ATLAS detector*, Tech. Rep. ATLAS-CONF-2013-010, CERN, Geneva, Mar, 2013.
- [93] ATLAS Collaboration, F. Bernlochner, J. Elmsheuser, F. Hoenig, D. Gillberg, J. Kretschmar, H. Li, W. Mader, R. Ospanov, C. Rudolph, E. Scifo, L. Spiller, and D. Tsybychev, *Search for the Standard Model Higgs boson in di-muon decay mode with 25 fb^{-1} data at $\sqrt{s} = 7$ and 8 TeV using ATLAS detector*, Tech. Rep. ATL-COM-PHYS-2014-161, CERN, Geneva, Feb, 2014.
- [94] ATLAS Collaboration, *Measurements of the properties of the Higgs-like boson in the two photon decay channel with the ATLAS detector using 25 fb^{-1} of proton-proton collision data*, Tech. Rep. ATLAS-CONF-2013-012, CERN, Geneva, Mar, 2013.
- [95] ATLAS Collaboration, *Measurements of the properties of the Higgs-like boson in the $WW^{(*)} \rightarrow \ell\nu\ell\nu$ decay channel with the ATLAS detector using 25 fb^{-1} of proton-proton collision data*, Tech. Rep. ATLAS-CONF-2013-030, CERN, Geneva, Mar, 2013.
- [96] J. Gaiser, *Charmonium Spectroscopy From Radiative Decays of the J/ψ and ψ'* . PhD thesis, Calif. Univ. Stanford, Stanford, CA, 1982. <http://inspirehep.net/record/183554>.

- [97] ATLAS Collaboration, *A measurement of the inclusive W^\pm and Z/γ^* cross sections in the e and μ decay channels in pp collisions at $\sqrt{s} = 7$ TeV with the ATLAS detector*, *Phys. Rev.* **D85** (2011) 072004, [arXiv:1109.5141 \[hep-ex\]](#).
- [98] S. S. Wilks, *The Large-Sample Distribution of the Likelihood Ratio for Testing Composite Hypotheses*, *Annals Math. Statist.* **9** (1938) 60 – 62.
- [99] ATLAS public luminosity results, <https://twiki.cern.ch/twiki/bin/view/AtlasPublic/LuminosityPublicResults>.
- [100] ATLAS Collaboration, *Jet energy measurement with the ATLAS detector in proton-proton collisions at $\sqrt{s} = 7$ TeV*, *Eur.Phys.J.* **C73** (2013) 2304, [arXiv:1112.6426 \[hep-ex\]](#).
- [101] ATLAS Collaboration, R. Daya-Ishmukhametova, J. Elmsheuser, F. Hönig, J. Groth-Jensen, S. Kortner, H. Li, W. Mader, R. Ospanov, C. Rudolph, S. Stern, and D. Tsybychev, *Search for the Standard Model Higgs boson in di-muon decay mode at $\sqrt{s} = 8$ TeV using ATLAS detector*, Tech. Rep. ATLAS-COM-CONF-2012-208, CERN, Geneva, Dec, 2012.
- [102] LHC Higgs Cross Section Working Group, *Handbook of LHC Higgs Cross Sections: 3. Higgs Properties*, [arXiv:1307.1347 \[hep-ph\]](#).
- [103] E. L. Berger and J. M. Campbell, *Higgs boson production in weak boson fusion at next-to-leading order*, *Phys.Rev.* **D70** (2004) 073011, [arXiv:hep-ph/0403194 \[hep-ph\]](#).
- [104] P. Golonka and Z. Was, *PHOTOS Monte Carlo: A Precision tool for QED corrections in Z and W decays*, *Eur. Phys. J.* **C45** (2006) 97–107, [arXiv:0506026 \[hep-ph\]](#).
- [105] B. Waugh, H. Jung, A. Buckley, L. Lonnblad, J. Butterworth, et al., *HZTool and Rivet: Toolkit and Framework for the Comparison of Simulated Final States and Data at Colliders*, [arXiv:hep-ph/0605034 \[hep-ph\]](#).
- [106] J. Collins, *Choosing the renormalization/factorization scale (QCD)*, *Journal of Physics G: Nuclear and Particle Physics* **17** (1991) no. 10, 1547. <http://stacks.iop.org/0954-3899/17/i=10/a=009>.
- [107] M. Guzzi, P. Nadolsky, E. Berger, H.-L. Lai, F. Olness, et al., *CT10 parton distributions and other developments in the global QCD analysis*, [arXiv:1101.0561 \[hep-ph\]](#).
- [108] A. Karneyeu, L. Mijovic, S. Prestel, and P. Skands, *MCPLOTS: a particle physics resource based on volunteer computing*, *The European Physical Journal C* **74** (2014) no. 2, 1–22.
- [109] P. Golonka and Z. Was, *Next to Leading Logarithms and the PHOTOS Monte Carlo*, *Eur.Phys.J.* **C50** (2007) 53–62, [arXiv:hep-ph/0604232 \[hep-ph\]](#).
- [110] Sjöstrand, Torbjorn, *private communication*, November, 2012.
- [111] ATLAS Collaboration, *Observation of an excess of events in the search for the Standard Model Higgs boson in the gamma-gamma channel with the ATLAS detector*, Tech. Rep. ATLAS-CONF-2012-091, CERN, Geneva, Jul, 2012.
- [112] J. Neyman and E. S. Pearson, *On the Problem of the Most Efficient Tests of Statistical Hypotheses*, *Philosophical Transactions of the Royal Society of London* **231** (1933) 289 – 337.
- [113] G. Cowan, K. Cranmer, E. Gross, and O. Vitells, *Asymptotic formulae for likelihood-based tests of new physics*, *European Physical Journal C* **71** (2011) 1554, [arXiv:1007.1727](#).
- [114] A.L. Read, *Presentation of search results: the CL_s technique*, *J. Phys. G: Nucl. Part. Phys.* **28** (2002) 2693.

-
- [115] ATLAS Collaboration, *Search for the Standard Model Higgs boson decay to $\mu^+\mu^-$ with the ATLAS detector*, [arXiv:1406.7663 \[hep-ex\]](#).
- [116] CMS Collaboration, *Search for the standard model Higgs boson in the dimuon decay channel in pp collisions at $\sqrt{s}=7$ and 8 TeV*, tech. rep., CERN, Geneva, 2013.
- [117] CMS Collaboration, *Performance of CMS muon reconstruction in pp collision events at $\sqrt{s}=7$ TeV*, *JINST* **7** (2012) P10002, [arXiv:1206.4071 \[physics.ins-det\]](#).
- [118] C. P. Office, *CERN announces LHC restart schedule*, "Cern Press Office", Jun., 2014.

List of Figures

2.1	Running of the strong coupling	5
2.2	Feynman graphs of DY dimuon production	7
2.3	Higgs boson production processes	8
2.4	SM Higgs boson production cross section versus mass	9
2.5	SM Higgs boson width as a function of mass	9
3.1	The LHC accelerator complex	12
3.2	ATLAS inner detector system	13
3.3	ATLAS pixel detector	14
3.4	ATLAS calorimetry system	15
3.5	ATLAS muon spectrometer	17
3.6	Schematic view of an MDT chamber	17
3.7	CSC chamber electrode geometry	19
3.8	Side view of the ATLAS muon spectrometer	20
3.9	Schematics of the TGC subdetector	20
3.10	ATLAS magnet system	21
3.11	Scheme of the trigger stages	21
3.12	L1 muon trigger items	22
5.1	Muon reconstruction efficiency	34
5.2	Dimuon mass and momentum resolution	34
6.1	Muon trigger efficiency 2011	36
6.2	Muon trigger efficiency 2012	36
6.3	Muon p_T distributions 2012	41
6.4	Muon η distributions 2012	41
6.5	Muon p_T distributions 2011	42
6.6	Muon η distributions 2011	42
6.7	Dimuon p_T distributions	43
6.8	Dimuon invariant mass distributions	43
6.9	Dimuon mass resolution	44
6.10	E_T^{miss} distribution after the baseline selection	47
6.11	$p_T^{\mu\mu}$ categorisation	48
6.12	Categorisation flowchart	49
7.1	Signal invariant mass distributions in the standalone categories	52
7.2	Signal invariant mass distribution in the combined categories	53
7.3	Signal model interpolation in the standalone categories	54
7.4	Signal model interpolation in the combined categories for $\sqrt{s} = 8$ TeV	55
7.5	Simulated background dimuon mass distributions of the standalone analysis	58
7.6	Dimuon mass distribution in the data control region of the standalone analysis	58
7.7	Pull distributions of standalone analysis background model fits to simulated background samples	59
7.8	Pull distribution of standalone analysis background model fits to the data control region	59
7.9	Toy MC studies of the standalone analysis background model	60
7.10	Dimuon mass difference in the low $p_T^{\mu\mu}$ category	61
7.11	Dimuon mass difference in the medium $p_T^{\mu\mu}$ category	62
7.12	Dimuon mass difference in the high $p_T^{\mu\mu}$ category	62
7.13	Background model fit to simulated background in the low $p_T^{\mu\mu}$ category	63
7.14	Background model fit to simulated background in the medium $p_T^{\mu\mu}$ category	63
7.15	Background model fit to simulated background in the high $p_T^{\mu\mu}$ category	64
7.16	Background model fit to simulated background in the VBF category	64
8.1	Generator-level dimuon mass under scale variations	73
8.2	Generator-level dimuon p_T under scale variations	73

8.3	Acceptance systematic uncertainty from PDF variations	74
8.4	Generator level dimuon mass under ISR variation	75
8.5	Generator level dimuon p_T under ISR variation	76
8.6	Generator level dimuon mass under FSR variation	76
8.7	Generator level dimuon p_T under FSR variation	77
8.8	Reweighted Higgs p_T spectra	79
8.9	Schematic description of the spurious signal effect	82
8.10	Resolution model central Gauss σ_{CG} distribution	84
8.11	Reconstruction efficiency distribution	84
8.12	Smeared dimuon mass validation in low $p_T^{\mu\mu}$	85
8.13	Smeared dimuon mass validation in medium $p_T^{\mu\mu}$	85
8.14	Smeared dimuon mass validation in high $p_T^{\mu\mu}$	86
8.15	Spurious signal fit result in the low $p_T^{\mu\mu}$ category	87
8.16	Spurious signal fit result in the medium $p_T^{\mu\mu}$ category	88
8.17	Spurious signal fit result in the high $p_T^{\mu\mu}$ category	89
8.18	Spurious signal fit result in the VBF category	90
9.1	Illustration of the sampling distribution	92
9.2	Illustration of CL_S	93
10.1	95% C.L. exclusion limit on μ for the standalone analysis	95
10.2	95% C.L. exclusion limit on μ for the combined analysis	97
10.3	Comparison of the ATLAS and CMS results	99
10.4	Comparison of Higgs boson couplings	100
C.1	Resolution model central Gauss μ_{CG} distribution	117
C.2	Resolution model outer Gauss μ_{OG} distribution	117
C.3	Resolution model outer Gauss σ_{OG} distribution	117
C.4	Resolution model fraction parameter distribution	118
C.5	Resolution model χ^2 distribution	118
C.6	Δp_T^{rel} distribution with high χ^2 fit	118
C.7	Δp_T^{rel} distribution with low χ^2 fit	119

List of Tables

2.1	Particles of the Standard Model	3
2.2	Interactions and gauge bosons of the SM	4
3.1	MDT layers per station	18
3.2	L1 muon trigger p_T thresholds	23
6.1	Applied muon triggers	35
6.2	Muon isolation criteria	39
6.3	GRLs for 2011 and 2012	40
6.4	Cutflow of the standalone analysis	46
6.5	Cutflow of the combined analysis	50
7.1	Mass resolutions for the combined analysis background model	62
8.1	Standalone analysis experimental systematic uncertainties	66
8.2	Combined analysis experimental systematic uncertainties	67
8.3	Gluon-fusion Higgs boson production cross-section and uncertainties	68
8.4	Vector-boson-fusion Higgs boson production cross-section and uncertainties	68
8.5	Higgs boson production via Higgs-strahlung cross-section and uncertainties	69
8.6	Higgs boson branching ratio uncertainties	70
8.7	Acceptance systematic uncertainty from scale variations	72
8.8	Acceptance systematic uncertainty from PDF variations	74
8.9	Acceptance systematic uncertainties from ISR and FSR variation	75
8.10	Standalone signal acceptance uncertainties	78
8.11	Systematic uncertainties due to Higgs boson p_T reweighting	80
8.12	Systematic uncertainty from MPI in the VBF category	81
8.13	Generator-level dimuon samples	82
8.14	Resolution selection cut flow	83
8.15	Spurious signal events	87
9.1	Statistical treatment of standalone analysis systematic uncertainties	94
9.2	Statistical treatment of combined analysis systematic uncertainties	94
10.1	Expected and observed 95% C.L. upper limits on μ for the standalone analysis	96
10.2	Expected and observed 95% C.L. upper limits on μ for the combined analysis	98
B.1	8 TeV $Z/\gamma^* \rightarrow \mu\mu$ samples.	105
B.2	8 TeV WW diboson samples.	105
B.3	8 TeV WZ diboson samples.	106
B.4	8 TeV $W\gamma$ diboson samples.	106
B.5	8 TeV ZZ diboson samples.	107
B.6	8 TeV W+jets samples.	107
B.7	8 TeV Single top and $t\bar{t}$ samples.	108
B.8	8 TeV ggF signal samples.	109
B.9	8 TeV VBF signal samples.	109
B.10	8 TeV WH signal samples.	110
B.11	8 TeV ZH signal samples.	110
B.12	7 TeV WW diboson samples.	111
B.13	7 TeV WZ diboson samples.	112
B.14	7 TeV $W\gamma$ diboson samples.	112
B.15	7 TeV ZZ diboson samples.	113
B.16	7 TeV W+jets samples.	113
B.17	7 TeV Single top and $t\bar{t}$ samples.	114
B.18	7 TeV ggF signal samples.	115
B.19	7 TeV VBF signal samples.	115
B.20	7 TeV WH signal samples.	116
B.21	7 TeV ZH signal samples.	116

Acknowledgements

It is hard to believe that already more than four years have passed since I first started researching for this thesis. Naturally, the number of people I have met, and also the number of people with an important impact on this work grew almost linearly with time. All those people who gave me so much during that time deserve my deepest gratitude, and I already send my apologies to those I forget to mention.

At first, I would like to thank my supervisor Michael Kobel, without whom none of this work could have been done. I still remember sitting in your “Introduction to Particle Physics” lecture during my undergrad studies, and it is you whom I owe a large part of my enthusiasm for particle physics in the first place. Besides, despite your tight schedule as head of the particle physics department, you were available for discussions and answers whenever I needed them. A big thanks also goes to the students and colleagues of the IKTP whom I had the opportunity to meet and work with. In particular, I want to thank Wolfgang Mader, Thomas Göpfert, Peter Steinbach, Anja Vest and Xavier Prudent, who guided my first steps at the institute and in the analyses. My deep gratitude goes to Marcus Morgenstern and Patrick Czodrowski, who are not only good colleagues, but became some of my best friends. I want to take this opportunity to thank those who supported me during the time I wrote this thesis, helping to improve it with very useful comments and suggestions. Thanks to Wolfgang Mader, Arno Straessner, Patrick Czodrowski, Anne Pfof, Marcus Morgenstern, Dirk Duschinger and Frank Siegert.

I further want to thank the small but effective $H \rightarrow \mu\mu$ analysis group at ATLAS. It is incredible how only a handful of people managed to analyse such an important and difficult channel. Thanks goes to Rustem Ospanov, Jacob Groth Jensen, Johannes Elmsheuser, Friedrich Hönig, Dmitri Tsybychev, Haifeng Li and Sebastian Stern.

Besides the professional support, I also want to take the opportunity to thank all my friends with whom I had the pleasure to spend my spare time when not doing research. Special thanks to the famous “Chemnitzer Jungs”.

I have saved my biggest gratitude for the last part, and the order of mention should by no means be interpreted as a personal ranking. Thank you, mom and dad! Thank you, Ines! I am so happy to have such a loving family, and I cannot gauge the importance of your decade-long support for me and my life choices. And thank you, Franziska! You were always there when I needed your support and confirmation.

Versicherung

Hiermit versichere ich, dass ich die vorliegende Arbeit ohne unzulässige Hilfe Dritter und ohne Benutzung anderer als der angegebenen Hilfsmittel angefertigt habe; die aus fremden Quellen direkt oder indirekt übernommenen Gedanken sind als solche kenntlich gemacht. Die Arbeit wurde bisher weder im Inland noch im Ausland in gleicher oder ähnlicher Form einer anderen Prüfungsbehörde vorgelegt.

Die vorliegende Dissertation wurde angefertigt unter der wissenschaftlichen Betreuung von Prof. Dr. Michael Kobel (Institut für Kern- und Teilchenphysik, TU Dresden), im Zeitraum zwischen Januar 2010 und Juli 2014.

Es haben keine früheren erfolglosen Promotionsverfahren stattgefunden.

Hiermit erkenne ich die Promotionsordnung der Fakultät Mathematik und Naturwissenschaften der Technischen Universität Dresden vom 23.02.2011 an.

Jörg Christian Rudolph, Diplom-Physiker